The Antennae Galaxies

—

a Key to Galactic Evolution

Dissertation

zur Erlangung der Doktorwürde

an der Fakultät für Physik

der Ludwig-Maximilians-Universität

München

vorgelegt von

Dipl.-Phys. Simon Karl

aus Regensburg, Deutschland

München, den 22. September 2011

Ludwig-Maximilians-Universität München

Erster Gutachter: Prof. Dr. Andreas Burkert

Zweiter Gutachter: Prof. Dr. Harald Lesch

Tag der mündlichen Prüfung: 12. Januar 2012

"Gesegnet seist du, machtvolle Materie, unwiderstehliche Evolution, immer neugeborene Wirklichkeit, du, die du in jedem Augenblick unseren Rahmen sprengst, uns zwingst, die Wahrheit immer weiter zu verfolgen. Gesegnet seist du, universelle Masse [...], die du unsere enge Masse überflutend und auslösend uns die Dimensionen Gottes offenbarst [...]."

Pierre Teilhard de Chardin

Zusammenfassung

Die sogenannten "Antennen"-Galaxien (NGC 4038/39) sind die uns am nächsten gelegene Galaxienverschmelzung (*"Merger"*) zweier gasreicher Spiralgalaxien. Ihr Name rührt von den zwei charakteristischen Gezeitenarmen, die aus ihren Hauptgalaxien herausragen. Aufgrund ihrer geringen Entfernung sind die Antennen sehr gut in modernen, hochauflösenden Beobachtungen durchmustert, was eine umfassende Betrachtung ihrer heutigen Morphologie und dynamischen Entwicklungsgeschichte erlaubt. Ziel dieser Arbeit ist es, die vorliegenden hochqualitativen Beobachtungen gegen neue, hochaufgelöste Simulationen zu testen, um unser Verständnis verschiedener physikalischer Prozesse in Mergern, wie etwa die Entstehung junger Sterne und Sternhaufen, zu erweitern. Diese Prozesse waren wahrscheinlich noch erheblich maßgeblicher in der Enstehung und frühen Entwicklung von Galaxien. Zunächst sollen präzise Anfangsbedingungen des Interaktionsorbits und der anfänglichen Galaxienmodelle festgelegt werden. Dazu wird eine ausgedehnte Parameterstudie durchgeführt, um ein gutes Vergleichsmodell mit den Antennen zu erhalten. Als Resultat der so gewonnenen Anfangsbedingungen werden die ersten hochaufgelösten Simulationen, die ein detailliertes theoretisches Pendant zur beobachteten Morphologie und Kinematik der Antennen darstellen, vorgestellt. In diesem Modell werden außerdem die heutige räumliche Verteilung von sternbildenden Gebieten und die totale Sternentstehungsrate sehr gut reproduziert. Beste quantitative Übereinstimmung erhält man unter der Annahme von sehr schwacher Rückkopplung der Sternentstehung an das interstellare Medium. Die Antennen befinden sich in einer außergewöhnlichen Phase ihrer Entwicklung kurz nach dem 2. Perizentrum. Laut unserem Modell werden sie schon in etwa $\sim 50\,\mathrm{Myr}$ miteinander verschmelzen. Desweiteren wird die Sternentstehungsgeschichte *aller* publizierter hydrodynamischer Antennen-Simulationen mit der beobachteten Altersverteilung der Sternhaufen verglichen, die gemäß einem Potenzgesetz $dN/d\tau \propto \tau^{-\gamma}$ mit Index $\gamma = 1$ abfällt. Unter der Annahme proportionaler Raten in der Stern- und der Sternhaufenentstehung ergibt sich, dass die Schwankungen in den simulierten Entstehungsraten alleine nicht ausreichen, um den beobachteten steilen Abfall der Altersverteilung zu erklären. Dies gibt einen deutlichen Hinweis auf eine effiziente und anhaltende Vernichtung von Sternhaufen in den Antennen — ähnlich zu moderater sternbildenden Galaxien. Zuletzt wird untersucht, ob die Antennen sich zukünftig in eine typische elliptische Galaxie entwickeln werden. Der virialisierte Überrest des Mergers gleicht einer oblaten, rotierenden Elliptischen mit einem Oberflächenhelligkeitsprofil gemäß einer Sérsic-Funktion mit Index $n \sim 5$. Für hohe Metallizitäten ($Z \gtrsim Z_\odot$) werden die Antennen in etwa $2.5 - 3\,\mathrm{Gyr}$ einer Population angehören, die heutigen Elliptischen entspricht. In dieser Arbeit wird ein verbessertes numerisches Modell der wechselwirkenden Antennen-Galaxien vorgestellt, welches als Basis zukünftiger Forschung dieses archetypischen Mergers dienen kann. Als nächster Schritt soll die ausgedehnte heiße Gaskomponente der Antennen untersucht werden, die im Röntgenbereich beobachbar ist. Außerdem testen wir unsere Ergebnisse in einem Vergleich verschiedener Simulations-Codes.

Summary

The Antennae galaxies (NGC 4038/39) are the nearest and best-studied major merger of two gas-rich spirals in the local Universe. They are named after the characteristic pair of tidal tails that protrude out of their main galactic disks. Due to their proximity the Antennae are extremely well sampled by modern high-resolution observations over an enormous wavelength range, from radio to X-ray. This allows for a comprehensive multiwavelength approach to the present-day morphology and dynamical history of the system. The goal of this Thesis is to test the available high-quality multiwavelength data against new high-resolution merger simulations as a key to improve our understanding of several merger-induced physical processes, such as starbursts and the formation of young star clusters. These processes are expected to have been even more important in the formation and early evolution of galaxies. First of all, accurate initial conditions for the interaction orbit and the initial galaxy models need to be constrained. To this end, we perform an extended parameter search in order to obtain a suitable match to the Antennae galaxies. Using these new initial conditions, we are able to present the first high-resolution numerical simulations that successfully match the detailed large- and small-scale morphology and kinematics of the Antennae galaxies. Moreover, the spatial distribution of star-forming regions as well as the total star formation rate are reproduced in excellent quantitative agreement, in particular, if we adopt a very weak stellar feedback. We find that the Antennae are currently in a special phase of their evolution, shortly after the second pericenter. They will merge soon within the next ~ 50 Myr. In addition, we compare the star formation histories of all published hydrodynamical Antennae simulations with the observed cluster age distribution. The latter is well approximated by a power-law $dN/d\tau \propto \tau^{-\gamma}$, declining as $\gamma = 1$. Under the assumption that clusters form at rates proportional to the total star formation, it is found that the variations in the simulated formation histories alone cannot account for most of the steep decline in the observed age distribution. This provides strong evidence for efficient, prolonged cluster disruption in the Antennae, similar to more quiescent galaxies. Finally, we address the question of whether the Antennae will evolve into a typical elliptical galaxy. We find that the virialized merger remnant resembles an oblate, fast-rotating early-type with surface brightness profile well fitted by a Sérsic function of index $n \sim 5$. For high metallicities ($Z \gtrsim Z_{\odot}$) the stellar remnant of the Antennae may add to a population of present-day ellipticals after secular evolution of another $\sim 2.5 - 3$ Gyr. Within this Thesis, we present an improved numerical model for the interacting Antennae galaxies that may serve as a test-bed for further investigations of this archetypal merger. As next steps, we plan to investigate the extended hot gas component found in X-ray observations of the Antennae, and test our present results in a code comparison project.

Meinen Eltern.

Contents

List of Figures

List of Tables

Chapter 1

Motivation

In modern hierarchical structure formation theories, such as the currently favored Λ cold dark matter (ΛCDM) model, galaxy mergers are the main drivers of galaxy evolution. Minor mergers are responsible for the thickening of galactic disks (Quinn et al. 1993; Velazquez & White 1999; Bournaud et al. 2007; Moster et al. 2010a), while major mergers, on the other hand, more dramatically affect the formation and evolution of galaxies. By inducing tidal torques they can efficiently transport gas to the centers of the galaxies (Barnes & Hernquist 1996; Naab et al. 2006), trigger star formation (Mihos & Hernquist 1996; Springel 2000; Cox et al. 2008), feed super-massive black holes (Hopkins et al. 2005; Springel et al. 2005; Johansson et al. 2009) and convert spiral galaxies into intermediate-mass ellipticals (Barnes 1992; Naab & Burkert 2003; Rothberg & Joseph 2004; Naab & Ostriker 2009). In the low-redshift universe ($z < 0.3$) about $\sim 5 - 10\%$ of all galaxies are interacting and merging (e.g. Lotz et al. 2008; Bridge et al. 2010; Lotz et al. 2011), and mass assembly via this mechanism was more important at earlier cosmic times when major mergers were more frequent (e.g. Patton et al. 2002; Conselice et al. 2003) and also more gas-rich (e.g. Tacconi et al. 2010).

The Antennae galaxies (NGC 4038/39), at a distance $D \sim 20$ Mpc, are the best-studied nearby major merger of two gas-rich spirals, providing an ideal laboratory to study interaction-driven starbursts. Due to their proximity, their stellar population and interstellar medium (ISM) have been observed in great detail covering an enormous wavelength range from the radio to the X-ray, allowing for a multiwavelength access to the dynamical history and the current physical state of the system (see, e.g. Zhang et al. 2001; Whitmore et al. 2010, and references therein). In the Antennae, the dominant star formation sites are found in extra-nuclear arc-like disk features and a dusty overlap region (Mirabel et al. 1998; Wang et al. 2004b), where also most of the molecular gas is found (Wilson et al. 2000; Gao et al. 2001). In addition, HST imaging has revealed a large number of bright young star clusters ($\gtrsim 1000$) which plausibly have formed in several bursts of star formation induced by the interaction (see Whitmore et al. 2010). These findings indicate that the Antennae are a prime

example out of only very few interacting systems where a similarly powerful, off-center starburst is observed. Furthermore, an extended hot gas halo has been detected, surrounding the main galaxies at a scale of $\sim 20\,\mathrm{kpc}$ (Fabbiano et al. 2001, 2004; Metz et al. 2004). Even further out, near the tip of the southern tidal tail, sites of on-going star-formation are identified along with two high surface density regions, being possible candidates for so-called "tidal dwarf galaxies" (Schweizer 1978; Mirabel et al. 1992).

The detailed information available in the recent observation data immediately raises a number of interesting questions, e.g.:

- What is the origin of extra-nuclear starbursts like the one observed in the Antennae galaxies?
- How do star clusters form and evolve in a highly interacting system like the Antennae?
- What is the physical driver behind the large-scale outflow of hot, X-ray emitting gas in the Antennae?
- How and when do self-gravitating, high-density concentrations of gas and stars form in tidal tails, similar to the tidal dwarf galaxy candidates in the Antennae?
- How will the Antennae look like in the future? Are they going to join the ranks of star-bursting ultra-luminous infrared galaxies (ULIRGs) or light up as energetic active galactic nuclei (AGNs)? Or, will their remnant galaxy evolve into a typical present-day elliptical galaxy?

However, to a big part, these questions have not been fully answered in theoretical studies so far and it is fair to say that our theoretical knowledge about the Antennae galaxies still lags behind the recent increase in the available high-quality observational data.

Within this Thesis, we focus on a number of the questions raised above, carrying out detailed numerical investigations of the Antennae galaxies in a two-step process. First, we improve the interaction orbit adopted in the literature so far. This, in a second step, enables us to study the interesting physical phenomena at play in this highly perturbed, star-bursting system. The Thesis is organized as follows. We will start by giving a short general introduction to observations and theoretical studies of the Antennae galaxies from a historical perspective in Chapter 2. Chapter 3 presents the background to the numerical codes we are using in this Thesis for the simulations and their post-processing, and explains the generation of initial conditions. A description of the process of modeling interacting systems, and an overview on how we obtained our specific match to the Antennae galaxies, is provided in Chapter 4. In Chapter 5, we will describe the results of our best match simulations with respect to the nature of the observed starburst in the overlap region of the Antennae, and, in Chapter 6, we direct

our investigations to the interplay of formation and destruction of young star clusters in the Antennae. Furthermore, we will have a glimpse into the future and investigate the properties of the relaxed merger remnant of the Antennae galaxies in Chapter 7, and, finally, we draw our conclusions and provide a short outlook in Chapter 8.

Chapter 2

The Antennae Galaxies

2.1 From Early Photographs to Space Telescopes - the History of the Antennae

Today the Antennae galaxies (NGC 4038/4039; Arp 244; VV 245; also known as the "Ring-tail galaxies") are probably one of the best-known and most spectacular interacting systems in the nearby Universe, situated at a distance of about 20 Mpc in the constellation Corvus (R.A. = $12^h01^m53.3^s$, Decl. = $-18°52'37''$). They are nicknamed after their prominent appearance with a pair of huge extended arms, protruding out to a total projected distance of $\sim 20'$ from side to side, and two overlapping, but still distinct main galactic disks, reminiscent of two antennae on top of an insect's head.

The first detection of the Antennae galaxies on February 2nd 1785 is ascribed to William Herschel, who speculated that the system could be a double nebula "opening with a branch or two nebulae very faintly joined" (Steinicke 2010). Nevertheless, he classifies them in his category IV for objects of unknown origin, which he calls "planetary nebulae". Later, his son John Herschel separates the system into two distinct objects in his so-called "Slough Catalogue" (Herschel 1833). In Figure 2.2, we show a first, still quite rough drawing of the Antennae galaxies, adapted from a publication by Lord Rosse, where only the more luminous one of the two tidal arms is sketched (Rosse 1861).

First photographs from optical observations were provided in the early 1920s by Perrine (1922) with his 75 cm reflector and Duncan (1923) with the 100-inch Hooker telescope on Mount Wilson. Both note the peculiar form of the object. While Perrine (1922) wonders about the origin of the one-sided arms and a possible relation between the two objects, Duncan (1923) is coining their nickname, describing the arms as "two faint extensions, like antennae" with projected distances of $\sim 6'$ and $\sim 12'$ to the main bodies. In 1940, a first detailed photograph reveals much of the inner "ring-tail"

Figure 2.1: Ground-based optical image of the Antennae galaxies. The system lies at a distance of ~ 20 Mpc in the constellation Corvus. The two galaxies NGC 4038 and NGC 4039 consist of a pair of impressive elongated tails and the two overlapping, but still distinct main galactic disks with a rich and complex substructure (see Figure 2.4 for further details). The northern disk and southern tail belong to NGC 4038, while the southern disk and northern tail belong to NGC 4039. North is pointing upwards, east is on the left. Image courtesy of Robert Gendler.

structure of the galaxies (Shapley & Paraskevopoulos 1940), and the systemic radial velocity is determined to a value of $v_{\rm sys} \sim 1,700\,{\rm km\,s^{-1}}$ using absorption and emission lines (Struve & Linke 1940). Note that this is actually quite close to the range of values measured today (e.g. de Vaucouleurs et al. 1991; Hibbard et al. 2001).

What is the origin of the long tails that seem to stick out of NGC 4038/39? At that time the answer to this question was still unclear. However, starting with first photographs and sketches by Zwicky (1953, 1956, 1959) and later systematic photographic surveys, such as the "Atlas and Catalog of Interacting Galaxies" (Vorontsov-Velyaminov 1959) and the famous "Atlas of Peculiar Galaxies" (Arp 1966), an increasing number of bridge- and tail-like features in other peculiar systems was discovered. Nowadays, interacting and merging systems are thought to make up a total of a few percent among all local galaxies (see Lotz et al. 2008; Bridge et al. 2010). Furthermore, Zwicky already noted correctly (as we think today) that the slender filaments and inter-connecting

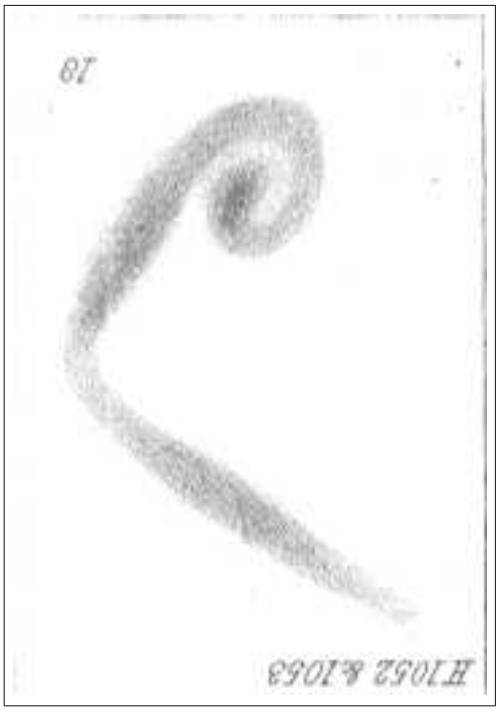

Figure 2.2: Original sketch of the Antennae galaxies taken from a publication by Lord Rosse (Rosse 1861). Only the parts belonging to NGC 4038 are drawn.

bridges observed in many peculiar galaxies must be the result of simple gravitational "tides and counter-tides" caused during close encounters of galaxies (Zwicky 1953). Consequently, these features consist mostly of stars. In Figure 2.3 we show Zwicky's drawing of the Antennae galaxies (Zwicky 1956).

A few years later, very faint radio emission is detected in the Antennae (Minkowski 1957; Mills et al. 1958), which, at that time, is fitting nicely into the growing observational evidence for a possible interaction origin of radio galaxies (see e.g. Baade & Minkowski 1954a,b). Using emission line spectroscopy, further optical studies report the first velocity fields in the Antennae galaxies, noting a large spread in the line-of-sight velocities of about $200\,\mathrm{km\,s^{-1}}$ in the central galaxies (Burbidge & Burbidge 1966; Rubin et al. 1970). The authors emphasize that these velocity fields are not as regular as expected for a single, or two isolated, spiral galaxies, lending further evidence to the collision hypothesis. However, e.g. Burbidge & Burbidge (1966) suggest a possible galactic wind - and not gravitational tides - to be responsible for the "ejection of material" seen in the Antennae galaxies, similar to the large-scale outflow observed in M82 (O'Connell et al. 1995; Westmoquette et al. 2009).

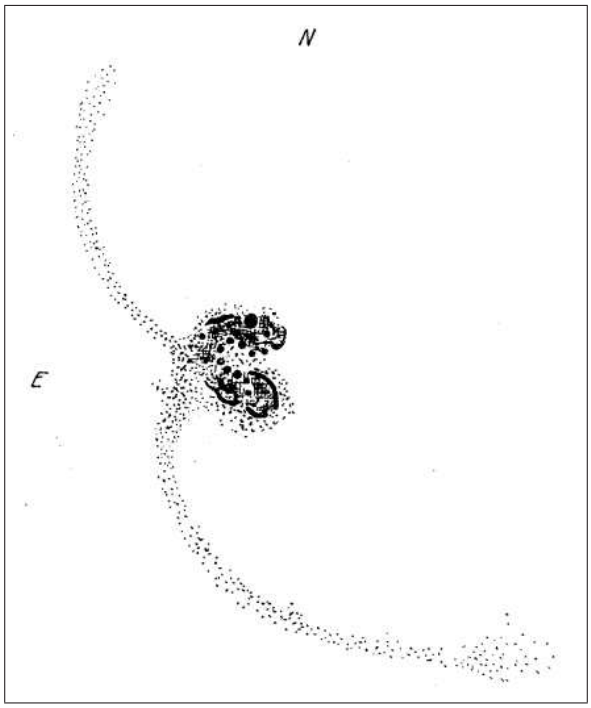

Figure 2.3: Zwicky's sketch of the Antennae galaxies taken from the publication in "Ergebnisse der exakten Naturwissenschaften" (Zwicky 1956).

2.2 All Colors of the Rainbow - the Multi-wavelength View of the Antennae

Owing to their proximity and the improved capabilities of modern ground- and space-based observatories such as the "Very Large Telescope" (VLT), the "Hubble Space Telescope" (HST), or the Chandra and Planck satellites, very detailed high-resolution observations of the Antennae have been obtained, with a large amount of data collected in a very broad range of wavelengths from the X-ray to the radio. With increasing spatial resolution, many studies concentrate on the central regions of the system, showing a wealth of complex substructures in the two disks (see for example Figure 2.4).

Many of the intriguing features of the Antennae galaxies already become evident by examining Figure 2.4 in a little more detail. First of all, we see unambiguous signs for substantial star formation activity in the last $\sim 10\,\mathrm{Myr}$ as traced by the H_α emission, indicated by the rich red color in Figure 2.4. This picture is endorsed at longer wavelengths which are less affected by dust absorption (see the discussion in Section 5.5). In particular, mid-infrared ISO observations show that actually the major part of the recent star formation must have taken place in the "overlap" region, which can be seen partly obscured by heavy dust lanes between the galaxies in Figure 2.4 (Vigroux et al. 1996; Mirabel et al. 1998). These results are confirmed by Spitzer mid-infrared

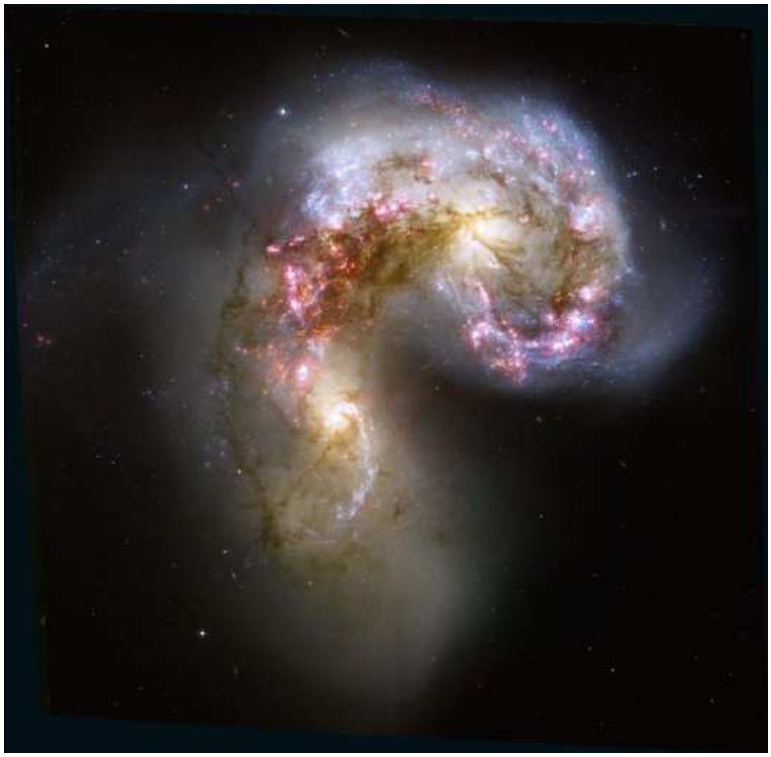

Figure 2.4: Composite color image of the central regions of the Antennae galaxies from the B-band (blue), V-band (green) and a combination of the I-band and an H_α filter in red. Recent star formation is indicated by the rich blue light from massive stars in young clusters, and the abundant H_α emission from HII regions. Large molecular gas reservoirs are traced in absorption by heavy continuous dust lanes especially in the "overlap" region between the two galaxies. The galactic nuclei appear yellowish due to substantial reddening by dust. Image courtesy of Brad Whitmore (Whitmore et al. 2010)

.

observations (Wang et al. 2004b) and recent Herschel-PACS far-infrared (FIR) data (Klaas et al. 2010). By combining different bands in the mid-infrared and FIR, which are less affected by obscuration and contamination from stellar infrared emission, local star formation rates (SFRs) in different regions in the Antennae could be determined (Wang et al. 2004b; Klaas et al. 2010). These observations show that the Antennae galaxies harbor a major off-nuclear starburst in the overlap region and the arc-like shape in the northern galaxy. This makes the Antennae an outstanding system out of only very few others which show a similar level of off-nuclear interaction-induced star formation. Among these are, e.g. Arp 140 (Cullen et al. 2007), II Zw 096 (Inami et al. 2010), NGC 6090 (Dinshaw et al. 1999; Wang et al. 2004a), NGC 6240 (Tacconi et al. 1999; Engel et al. 2010), and NGC 2442 (Pancoast et al. 2010). This behavior contrasts to the general trend observed, e.g. in a sample of 53 pre-merger galaxy pairs (Smith et al. 2007) as well as results from previous numerical simulations (e.g. Barnes & Hernquist 1996). Especially intriguing in this context is the fact that the observed overlap starburst is even outshining the two nuclei with integrated values of $\mathrm{SFR_{overlap}} \sim 5\,\mathrm{M_\odot\,yr^{-1}}$ and $\mathrm{SFR_{nuclei}} = 1.7\,\mathrm{M_\odot\,yr^{-1}}$, respectively, as estimated by the most recent observations (Klaas et al. 2010). A few areas in the overlap region even show specific SFRs ($\hat{=}$ SFRs per unit mass) reaching levels similar to those of heavily star-bursting ULIRGs (Wang et al. 2004b). Earlier numerical models failed to reproduce the relative SFRs observed in the nuclei and the overlap region. They also under-estimate the total SFR in the Antennae which is measured in different observations within a range of $\sim 5 - 20\,\mathrm{M_\odot\,yr^{-1}}$ (e.g. Stanford et al. 1990; Zhang et al. 2001; Knierman et al. 2003; Brandl et al. 2009; Klaas et al. 2010).

Consequently, the overlap region - not the galactic disks or the nuclei - is also where the most abundant gas reservoirs of the Antennae are found. Most of the gas resides in huge molecular complexes with a total mass of $\sim 1.5 \times 10^{10}\,\mathrm{M_\odot}$ (Wilson et al. 2000; Gao et al. 2001). The total mass in molecular gas exceeds the total amount of HI in the galactic disks by a factor of about ~ 10 (Hibbard et al. 2001). This is taken as evidence that, as the merger proceeds, most of the available atomic gas component is converted into molecular form, as a further step along the evolution of merging systems to become molecular gas-rich ULIRGs (see e.g. Joseph & Wright 1985; Sanders & Mirabel 1996; Lutz et al. 1998). Individual molecular clouds could be detected in sensitive CO $J = 1 - 0$ measurements and were found to follow a power-law mass function with exponent of 1.4 ± 0.1 from $5 \times 10^6\,\mathrm{M_\odot}$ up to very large complexes with $\sim 10^9\,\mathrm{M_\odot}$. Zhu et al. (2003) determine a total H_2 mass of $\sim 4 \times 10^9\,\mathrm{M_\odot}$ in the overlap region, where Haas et al. (2000) find a total dust mass of $\sim 10^7\,\mathrm{M_\odot}$.

The rich system of young star clusters in the Antennae has attracted particularly close attention (e.g. Bastian et al. 2006, 2009; Brandl et al. 2005; Fall et al. 2005, 2009; Gilbert & Graham 2007; Kassin et al. 2003; Mengel et al. 2005; Naiman et al. 2009; Zhang & Fall 1999). In particular, HST observations have detected a large number ($\gtrsim$1000) of young star clusters in the Antennae as a result of the on-going merger

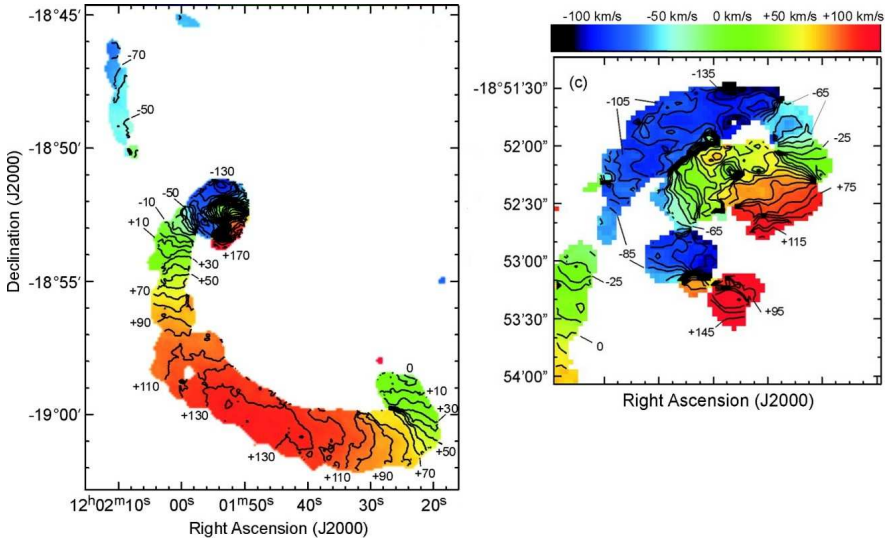

Figure 2.5: Intensity-weighted HI velocity maps of the Antennae galaxies by Hibbard et al. (2001). *Left panel:* large-scale distribution of the HI . *Right panel:* inner regions of the Antennae. Line-of-sight velocities relative to the systemic velocity of $1630\,\mathrm{km\,s^{-1}}$ (green) are color-coded in red for parts receding from, and blue for parts approaching the observer. Iso-velocity contours are drawn at $10\,\mathrm{km\,s^{-1}}$ intervals.

process (Whitmore & Schweizer 1995; Whitmore et al. 1999, 2010). In Figure 2.4, the locations of massive hot young stars formed in the young star clusters can be seen as abundant sprinkles of blue light spreading over the entire system. The brightest star clusters in these observations generally show properties (e.g., masses, sizes, etc) similar to those of "normal" old globular clusters in the Milky Way. But also some exceptionally large "super" star clusters with radii $r \gtrsim 10\,\mathrm{pc}$ are found (Whitmore et al. 1999). Among the clusters, some major, spatially correlated populations were identified (Whitmore et al. 1999; Kassin et al. 2003): while the youngest star clusters seem to form in the overlap region ($\tau < 5\,\mathrm{Myr}$), young star clusters are generally found spread more evenly over the overlap region and a ring-like configuration in the disk of NGC 4038 ($\tau \lesssim 30\,\mathrm{Myr}$). Another, intermediate-age population ($\tau = 500 - 600\,\mathrm{Myr}$) is distributed throughout the disk of NGC 4038, probably induced by the first close encounter of the disks (Whitmore et al. 1999; Zhang et al. 2001). Using the superior statistics of the star cluster system in the Antennae, it is found that their luminosity and mass functions are well described by power-laws with exponents $\alpha \approx \beta \approx -2$ in a mass range of $10^4\,\mathrm{M_\odot} < M < 10^6\,\mathrm{M_\odot}$ (Whitmore et al. 1999; Zhang & Fall 1999; Whitmore et al. 2010), similar to the scale-free luminosity functions of giant molecular clouds and HII -regions from which they have formed. The derived cluster age distribution is also steeply declining as $dN/d\tau \sim \tau^{-1}$ for ages 10^6 yr $\lesssim \tau \lesssim 10^9$ yr. Fall et al. (2005) takes this as an indication that star clusters are efficiently destroyed over a relatively large age range ($\gtrsim 2$ decades), creating an exponentially decaying age distribution. The formation and disruption of star clusters in the Antennae galaxies in

the context of N-body+SPH simulations will be treated in Chapter 6.

While most of the molecular gas is concentrated towards the central regions of the Antennae, about 70% of the total HI gas mass is found to be situated within the extended tidal tails, with about 10 times as much HI mass in the southern than in the northern arm (van der Hulst 1979; Gordon et al. 2001; Hibbard et al. 2001). Since the ionized and molecular gas phases are in general only barely detectable outside the main galaxies due to their low densities, HI is the natural and most valuable tracer for the global large-scale morphology and kinematics in interacting systems. In the Antennae, this can be seen in Figure 2.5 in the deep VLA 21cm line observations by Hibbard et al. (2001). They reveal the basic kinematical features of the system with the two tidal tails moving in opposite directions. While the northern tail approaches the observer, the southern tail is receding, indicated by the mostly blue and red colors, respectively (left panel in Figure 2.5). The southern tail shows a very shallow velocity gradient along the arm, lying almost perpendicular to the observer's line-of-sight in the plane-of-the-sky, with sharp turns at the two edges. The two main galactic disks exhibit a rotation-like pattern with the northern sides approaching and the southern side receding from the observer (right panel in Figure 2.5).

Further out along the tidal tails we also find interesting objects meriting a closer study. In particular, Schweizer (1978) notes a possible dwarf stellar system near the end of the southern tidal tail. It shows signs of recent active star formation, as evidenced by the blue colors and four distinct HII regions in that area. A little further out, at the tip of the southern tail, Mirabel et al. (1992) find another tidal dwarf galaxy candidate consisting "of a chain of nebulae ionized by [...] massive stars, which are embedded in an envelope of HI ". The integrated properties of this tidal dwarf galaxy candidate are broadly consistent with the properties of low-surface brightness dwarf galaxies (Mirabel et al. 1992; Hibbard et al. 2001). However, it is still unclear whether these concentrations are self-gravitating entities in their own right (Hibbard et al. 2001). By comparing the UV colors in the tails to estimates of simple stellar population models, Hibbard et al. (2005) note an age trend along the southern tidal tail. The youngest population at the end of the tail seems to have younger ages than the dynamical age of the arm (estimated from numerical simulations). In this sense, the blue complexes found at the end of the southern tail could possibly hint at a formation mechanism for baryon-rich dwarf galaxies out of the tidal debris of merging galaxies (e.g., Duc & Mirabel 1998; Knierman et al. 2003; Wetzstein et al. 2007).

With its high sensitivity and angular as well as spectral resolution, the Chandra X-ray space observatory provides the unique opportunity to study the spatially resolved thermal and chemical properties of different regions and to detect populations of individual X-ray sources out to the distance of the Antennae. In a first deep Chandra ACIS pointing, Fabbiano et al. (2001) determine a total X-ray luminosity of $L_{\rm X}^{0.1-10\,{\rm keV}} = 2.3 \times 10^{41}\,{\rm erg\,s^{-1}}$ of the Antennae, with about half of the total luminosity

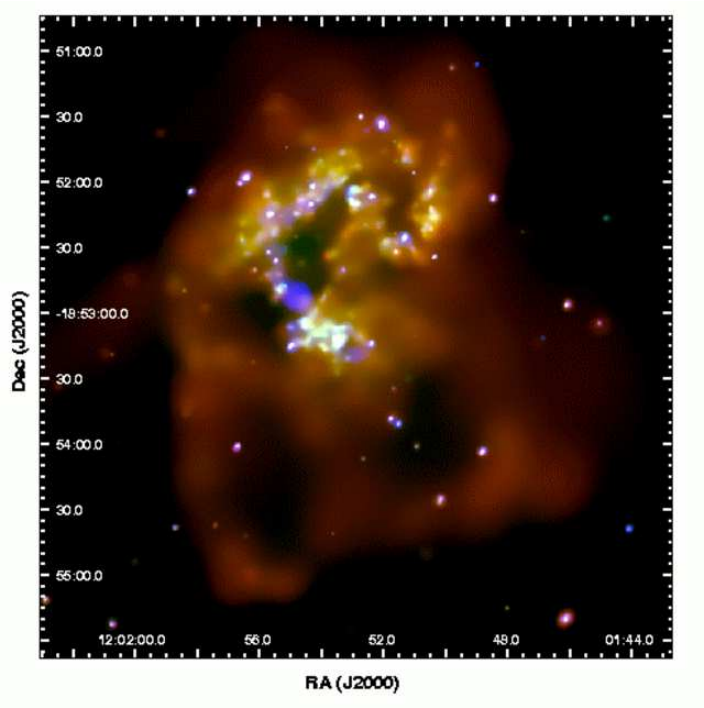

Figure 2.6: Smoothed three-color image of the X-ray emission in the Antennae galaxies using data in the $0.3-0.65\,\mathrm{keV}$ (red), $0.65-1.5\,\mathrm{keV}$ (green), and $1.5-6.0\,\mathrm{keV}$ bands. Three distinct components are nicely distinguishable: a number of compact X-ray sources due to neutron stars and black holes, emission from the main body of the Antennae, and a diffuse hot gaseous halo around the galaxies. Especially intriguing are the two extended loops to the south.

coming from point-like sources, $\sim 1.1\times10^{41}\,\mathrm{erg\,s^{-1}}$. They also discover a hot gaseous outflow on a $\sim 10\,\mathrm{kpc}$ scale to the south of the galactic disks. Assuming that these features started to develop some $\sim 10^7-10^8$ yr ago, this indicates expansion velocities of the order of $100-1000\,\mathrm{km\,s^{-1}}$. Fabbiano et al. (2004) find these features to be large-scale "loops" with an enhanced X-ray surface brightness at the outer rims at a distance of $\sim 10\,\mathrm{kpc}$ from the galactic disks, surrounded by a hot low surface brightness halo extending out to $\sim 18\,\mathrm{kpc}$ (see Figure 2.6). They speculate that the hot gas in the loops could be shocked, super-sonic ISM, swept up in a starburst-driven wind. Zezas & Fabbiano (2002) and more recently, Zezas et al. (2007) derive the X-ray luminosity functions for the populations of discrete X-ray sources in the Antennae. Their cumulative luminosity function is well fitted by a power-law with a slope of $\alpha\sim-0.5\ldots-0.8$, indicating that the X-ray luminosity functions of star-forming galaxies are flatter than those of early-type galaxies. It is worth noting that the X-ray source population in the Antennae includes a surprisingly high number of 14 ultra-luminous X-ray ("ULX") sources ($L_X>10^{39}\,\mathrm{erg\,s^{-1}}$; Zezas et al. 2006). Most of the discrete sources are thought to be young high-mass X-ray binaries ("HMXB"), with a possible beamed component for the most luminous sources (Zezas & Fabbiano 2002; Zezas et al. 2007). By fitting the spectra of a co-added Chandra data set with total exposure time of $\sim$ 411 ks,

Fabbiano et al. (2004) and Baldi et al. (2006a) determine the spatially varied abundances of different metal species (Fe, Ne, Mg, and Si) in the hot ISM. They find a large variety in the chemical composition of different regions in the Antennae, ranging from sub-solar ($\sim 0.2 Z_{i,\odot}$, i = Fe, Ne, Mg, Si) to significantly super-solar values in a number of $\alpha-$elements ($\sim 20 Z_{i,\odot}$, i = Ne, Mg, Si). The total mass in the hot diffuse gas of the extended features, is about $4 \times 10^8\,\mathrm{M}_\odot$ (Fabbiano et al. 2001). Stellar feedback from young star clusters contributes to the heating of the X-ray emitting gas in some regions, but a direct proportionality between the mass in clusters and the hot gas is not observed (Metz et al. 2004). The nuclei of both galaxies show a rather weak X-ray activity with luminosities of $L_{\mathrm{X},4038} \sim 10^{39}\,\mathrm{erg}s^{-1}$ and $L_{\mathrm{X},4039} \sim 8 \times 10^{39}\,\mathrm{erg}s^{-1}$, respectively (Zezas et al. 2002).

Recently, there has been a debate about the exact distance to the Antennae galaxies. Based on photometry of the tip of the red giant branch (RGB), Saviane et al. (2008) proposed a distance of $D = 13.3 \pm 1.0$ Mpc. This distance is quite moderate with respect to the estimate from the Hubble flow recession velocity relative to the Local Group. Using a Hubble constant $H_0 = 71\,\mathrm{km\,s^{-1}\,Mpc^{-1}}$ and a value of $cz_{\mathrm{LocalGroup}} = 1439\,\mathrm{km\,s^{-1}}$ (de Vaucouleurs et al. 1991) one obtains the more commonly adopted distance $D \sim 20$ Mpc (see Whitmore & Schweizer 1995). Schweizer et al. (2008) combined the latter estimate, a re-analysis of the Saviane et al. data (with different conclusions!), and new observations of a type Ia supernova in the southern tail of the Antennae (Drake et al. 2007) to propose a distance estimate of $D = 22 \pm 3$ Mpc. We note here that changing the adopted distance has important consequences for most physical scales. For example, projected distances scale proportional to the assumed distance to the system, while absolute magnitudes scale with the logarithmic distance. However, most studies adopt quite similar distance estimates, and we assume the errors due to different distances to be small or of the same order in most (order of magnitude) calculations with respect to other simulated or observational errors.

There certainly exist even many more observations on the Antennae galaxies than what is compiled in this Chapter. However, naming them all would clearly go beyond the scope of this Thesis. So we have tried to give a rough overview according to personal taste and the contents of the forthcoming chapters. A nice overview relating the different, multi-wavelength observations in the Antennae may be found for instance in Zhang et al. (2001) and further details will also be given in Chapters 5-6.

2.3 Numerical Simulations of the Antennae Galaxies

On the theoretical side, Holmberg (1941) was probably the first who addressed tidal deformation of galaxies in numerical experiments. He studied encounters of two disk galaxies with each disk represented by 37 light bulbs in circular motion about a common

center of mass. Exploiting that both electromagnetic and gravitational forces share the same characteristic $\propto 1/r^2$ scaling, Holmberg measured the intensity and direction of the light as a proxy for the gravitational accelerations on each 'mass point', represented by one of the light bulbs, with a simple photocell. According to the accelerations computed in this way, the particle trajectories could then be followed by gradually moving all light bulbs and repeating the whole exercise. Holmberg was primarily interested in whether galaxies could be trapped in galaxy groups and larger galaxy clusters due to repeated tidal captures of two galaxies on initially hyperbolic orbits. However, he also noted that on slower, parabolic orbits tidal deformations could develop naturally, shortly after a close passage.

In the early 1960s, Pfleiderer & Siedentopf (1961) and Pfleiderer (1963) used the first real computers to investigate how spiral patterns in disk galaxies could be excited by tidal interactions with another closely passing galaxy. To this end, they, again, used a simple setup, where the main galaxy is modeled as a central point-mass surrounded by massless test particles on circular orbits, comprising a non-self-gravitating disk. The intruder galaxy, on the other hand, is represented by a single point-mass without any further substructure. Thus, the gravitational N-body problem is reduced to the motion of N-2 massless test particles in the gravitational field of two galactic point-masses, which themselves move on analytic Keplerian two-body trajectories. With this method, called "restricted 3-body" method, Pfleiderer and Siedentopf were in fact successful in producing tidal tails in their simulations, but did not yet relate their findings to the peculiar features observed in nearby galaxies.

Finally, the idea was picked up again about 10 years later in a series of papers (Toomre & Toomre 1970, 1971; Yabushita 1971; Wright 1972; Clutton-Brock 1972). But it was not before the seminal paper by Toomre & Toomre (1972; TT72) that conclusive evidence was brought forward for a possible interaction origin of the long tails seen in the Antennae and similar systems, e.g. NGC 4676 ('The Mice'). Using the restricted 3-body method, now with two point masses each surrounded by a swarm of test particles, their binary disk galaxy merger simulations suggest that the Antennae have passed the first pericenter and "are about to do it again", i.e. that they are approaching each together again in a second pericenter. Their work can be seen as the major step in establishing that the bridges and tails observed in so many peculiar galaxies are nothing but the tidal relics of close encounters between two spiral galaxies. In this scenario, the bridges are formed from encounters involving a smaller companion galaxy, while long tails are the result of prograde encounters between two (more) equal-mass partners with a very close pericentric passage. TT72 also predict that the merger remnants resulting from the fierce clashes of two equal-mass spiral galaxies would be merging rather quickly, with their final remnants resembling elliptical galaxies. This idea is naturally leading to the so-called "merger hypothesis" for the formation of elliptical galaxies (Toomre 1977). Toomre's reasoning for his hypothesis footed mainly on a compilation of 11 merging systems all showing major tidal tails and very close,

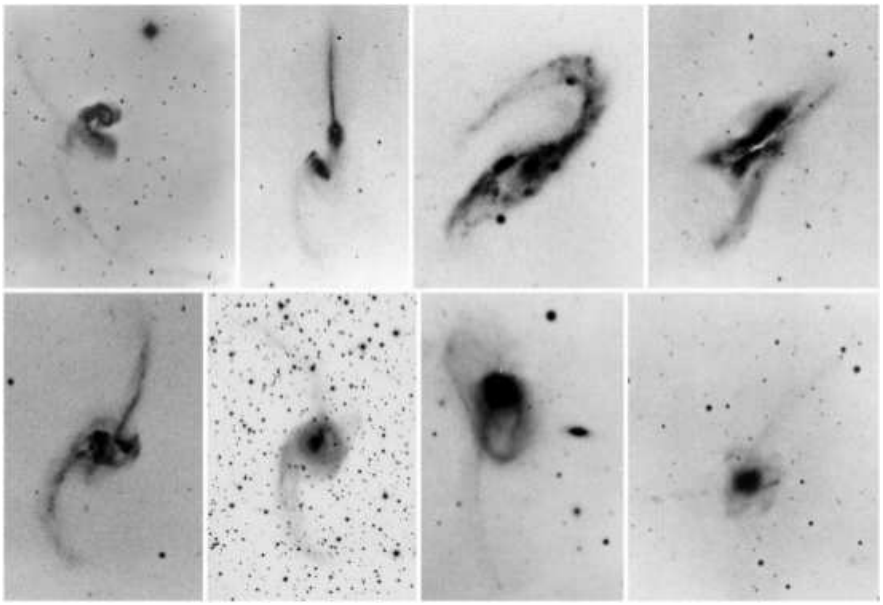

Figure 2.7: A selection of galaxies in the "Toomre sequence" (Toomre 1977) from the Arp atlas (Arp 1966), depicting a putative evolutionary track of merging galaxy pairs. The sequence includes *(from upper left to lower right)*: NGC 4038/4039 ("The Antennae"), NGC 4656 ("The Mice"), NGC 3509, NGC 520, NGC 2623, NGC 3256, NGC 3921, and finally, NGC 7252 ("Atoms for Peace"). Image courtesy of John Hibbard.

or not even separable main bodies, ordered in a sequence according to their putative merging stage (Figure 2.7)[1].

Much of the immediate credibility of TT72's work was due to the fact that they provided models that closely represent the observations of four specific well-known interacting systems. Other than the Antennae galaxies, these include Arp 295, M51 + NGC 5195, and NGC 4676 - the "Atoms of Peace" galaxy. For their Antennae model, TT72 adopt a prograde-prograde encounter geometry, where the galaxies are put on an elliptical orbit ($e = 0.5$) with disk inclinations $i = 60°$ and pericenter arguments $\omega = -30°$ for both disks (see Section 4.1). Choosing equal mass progenitor galaxies, this orbit results in very long symmetric and "crossed" tails quite akin to the Antennae at the time of best-match. The latter was chosen slightly more than $\sim 1/2$ of an orbital period after the first pericenter passage (see Figure 2.8). This first Antennae model was a real success. Nevertheless, there were still some remaining critical issues which were partly due to the simplistic modeling approach, neglecting some important physics such as the self-gravity in the disks and dynamical friction, but also partly due to their specific Antennae model. For instance, their symmetric set-up results in

[1]Note that the Antennae are put in the prominent first place of this sequence, corresponding to the earliest interaction stage despite the proximity of their main bodies. We will come back to this aspect in Chapter 5.

exactly equal tidal tails, while the observed tails are unequal in length and differently curved. In addition, a comparison to the observed velocity maps available at that time (Rubin et al. 1970) shows a mismatch in the velocity fields. Most severe, due to the lack of dynamical friction, the orbital evolution of the models could be followed reliably only for a small part of the full merger timescale (of a few orbital times). The latter issue was addressed in a subsequent model which used an analytical prescription for the orbital decay, adopting a nearly-parabolic orbit with eccentricity $e = 0.9$ (Mahoney et al. 1984).

Another key ingredient for modern theories of galaxy evolution, not yet considered in the first Antennae models, is the role of a dark matter halo. Almost two decades later, Barnes (1988) performed the first self-consistent N-body simulation of the Antennae galaxies including a bulge, a disk, and a live dark matter halo component with a mass ratio of 1:3:16 and a total mass of $M_{\rm tot} = 2.75 \cdot 10^{11}\,{\rm M}_\odot$ for each galaxy. As already envisaged by TT72, the inclusion of self-gravitating massive dark matter halos greatly enhances the orbital decay by efficiently transferring binding energy and angular momentum from orbital to internal motions. Consequently, at the time of best match in TT72's model, the galaxies have already merged.

Dubinski et al. (1996) studied the influence of massive dark matter halos on the development of tidal tails by adopting different halo-to-disk mass ratios. In their simulations, models with halo-to-disk mass ratios of more than 10:1 are found to be very ineffective in reproducing long, extended tidal tails as seen in the Antennae. Since the typical values for spiral galaxies in a hierarchical cold dark matter Universe tend to be much higher than this (see, e.g. McGaugh et al. 2010; Moster et al. 2010b; Guo et al. 2010, for recent publications), they argued for a possible conflict with a bottom-up cosmological scenario. However, Springel & White (1999) note that the ability to produce tidal tails is primarily determined by the relative size of disk and halo rather than by the mass ratio of dark to luminous matter. Following Mo et al. (1998), they propose a quantitative measure for the efficiency of the tidal response, $\mathcal{E} \equiv (v_e/v_c)^2$, relating the escape velocity as an indicator for the depth of the potential v_e to the circular velocity v_c measured at a radius $R = 2\,r_d$, where r_d is the scale length of the disk (see Section 3.3). This is approximately the radius, where about half of the disk mass is enclosed and the maximum circular velocity is reached. For $\mathcal{E} \lesssim 6$ galactic disks are generally found to be susceptible to tidal perturbations (Mo et al. 1998).

Mihos et al. (1993) included for the first time gas-dynamics and star formation in their simulation of the Antennae galaxies, adopting TT72's disk configurations. They used a sticky particle scheme, where discrete clouds evolve by merging and fragmentation. However, they found most of the star formation in their model to be concentrated towards the centers of the galaxies at variance with the observed spatially distributed star formation in the Antennae peaking in the overlap region between the two nuclei (see Section 2.2).

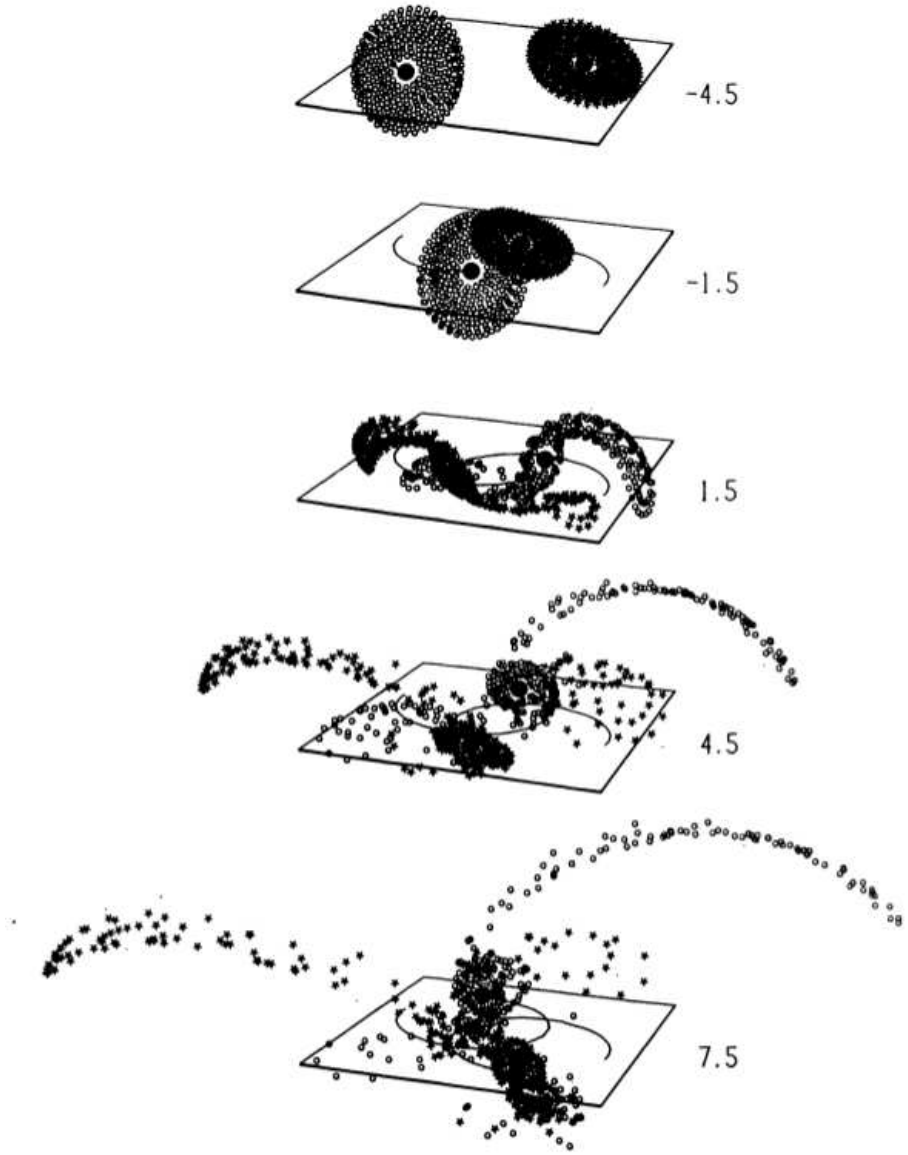

Figure 2.8: Time evolution of the symmetric Antennae model by Toomre & Toomre (1972). The five snapshots illustrate different stages of the encounter, equally spaced in time, before and after the first pericentric passage at $t = 0$. For clarity, the vantage point is not chosen as the viewing direction of the best match, but slightly elevated and from the right. Adaption of Figure 9 from Toomre (1974).

Given the vast and still growing amount of observational data for the Antennae galaxies, a serious modeling effort would be highly desirable to equally improve our theoretical understanding of this archetypal key merging system. However, most of the models presented up to now, are still largely based on the "canonical" orbital parameters given in TT72. Only recently, some new orbits have been proposed. For example, Renaud et al. (2008, 2009) investigate the role of compressive tidal forces as a possible mechanism to enhance interaction-induced starburst, adopting different arguments of pericenter passage. Using this model, Teyssier et al. (2010) show that fragmentation in a cool and turbulent ISM may lead to a burst of spatially extended star formation in galaxy mergers. The most serious modeling effort including a large parameter survey, however, has been performed in the work detailed in this Thesis (see Chapters 4 - 5) and a number of recent publications (e.g. Karl et al. 2008; Kotarba et al. 2010; Karl et al. 2010, 2011). We will discuss how we obtained the presently best-matching model for the Antennae galaxies in more detail in Chapter 4.

Chapter 3

Numerical Techniques

3.1 The Numerical Code

The majority of the numerical simulations presented in this Thesis has been performed using the parallel tree + smoothed particle hydrodynamics (SPH) N-body code GADGET 2 (Springel 2005), and its more recent, updated version GADGET 3. In this Chapter, we will present the most relevant details of these codes which were utilized to study a number of interesting aspects of the galactic dynamics, the physics of the ISM and the interaction-induced star formation in the merging Antennae galaxies (see Chapters 5 - 7).

3.1.1 The N-body Method

In a number of astrophysical systems the spatial extent of one single body is small with respect to the typical distance to other members of the system. This is true, for example, for the galaxies in a galaxy cluster, single stars within in a galaxy or a globular cluster, and the planets in our Solar system. Hence, these systems may be treated, in a first approximation, as simple gravitational N-body systems, where each body, i, of the N mutually interacting point sources evolves under the influence of the gravitational acceleration $\mathbf{a}_i$ from all other system members. This is encoded by Newton's law:

$$\mathbf{a}_i = -\sum_{j \neq i} \frac{\mathrm{G}m_j}{r_{ij}^3}(\mathbf{r}_i - \mathbf{r}_j), \tag{3.1}$$

where $\mathbf{r}_i$ and $\mathbf{r}_j$ are the positions of particles i and j, respectively, which are separated by a distance $r_{ij} = |\mathbf{r}_j - \mathbf{r}_i|$, m_j is the mass of particle j and G the gravitational constant.

The corresponding equations of motion are represented by two sets of $3\,N$ first-order

ordinary differential equations, written as

$$\frac{\mathrm{d}\mathbf{r}_i}{\mathrm{d}t} = \mathbf{v}_i, \tag{3.2}$$

$$\frac{\mathrm{d}\mathbf{v}_i}{\mathrm{d}t} = \mathbf{a}_i, \tag{3.3}$$

where $\mathbf{v}_i$ is the velocity of particle i, respectively, and the acceleration $\mathbf{a}_i$ is given by Equation 3.1.

Since there exists no "shielding" as, e.g., for electromagnetic forces in ionized plasmas, gravitational forces act over a long range, thus, exhibiting a high dynamic range. This has the effect that the resulting equations of motion are highly non-linear, which generally rules out an analytic approach to these kinds of problems. Numerical calculations are in most cases the only viable way to study the formation and evolution of the systems under consideration. To this end, the continuous, first-order differential equations (3.2) and (3.3) are replaced by piece-wise linear differential equations and the variable values of $\mathbf{r}_i$ and $\mathbf{v}_i$ are only evaluated at discrete time intervals.

Once the initial positions and velocities for all particles are set, in GADGET, the particles are advanced in time using the common "leapfrog" integrator in the "kick-drift-kick" (KDK) form (see, e.g. Quinn et al. 1997):

$$\begin{aligned}
\mathbf{v}_i^{n+1/2} &= \mathbf{v}_i^n + \mathbf{a}_i^n \cdot \left(\frac{1}{2}\Delta t_i^n\right), \\
\mathbf{r}_i^{n+1} &= \mathbf{r}_i^n + \mathbf{v}_i^{n+1/2} \cdot \Delta t_i^n, \qquad \text{and} \\
\mathbf{v}_i^{n+1} &= \mathbf{v}_i^{n+1/2} + \mathbf{a}_i^n \cdot \left(\frac{1}{2}\Delta t_i^n\right), \qquad (3.4)
\end{aligned}$$

(3.5)

where Δt_i^n is the particle's time step from n to $n+1$. The calculation of the gravitational accelerations is done at the beginning of each time step. The exact algorithm to do that is the most fundamental and time-consuming part in any modern N-body code and will be treated in Section 3.1.1.2.

Owing to the wide range of timescales present in most astrophysical problems, GADGET assigns to each particle the time step on a (quasi-)individual basis. This is done by using a time step criterion depending on the dynamical state of the particle i, i.e.

$$\Delta t_i = \min\left(\Delta t_{\max}, \left(\frac{2\eta\epsilon_i}{|\mathbf{a}_i|}\right)^{1/2}\right), \tag{3.6}$$

where η is a tolerance parameter, ϵ gives the gravitational softening (see Section 3.1.1.1 below), and $\Delta t_{\max}$ is the user-defined maximum allowed time step (see Springel 2005). In addition, SPH particles are usually limited by an Courant-like time step criterion, which will be discussed in Section 3.1.2. The particles are then systematically grouped into a hierarchy of time steps, with each discrete time bin being a power-of-two subdivision of the global maximum time step $\Delta t_{\max}$ such that the step size of level j in the hierarchy is given by $\Delta t_j = \Delta t_{\max}/2^j$. This allows for a computationally efficient and natural way of sub-cycling smaller time steps. We have used a tolerance parameter of $\eta = 0.02$ throughout this Thesis.

3.1.1.1 Gravitational Softening

In some cases it can be useful to change the form of the Newtonian potential such that it deviates from its pure $\sim 1/r$ form if the distance between two particles r becomes smaller than some predefined parameter ϵ. This usually requires a "softening" of the gravitational potential and forces, where the role of the gravitational softening in N-body codes is generally twofold, depending on the properties of the specific system under consideration. When simulating systems with frequent individual close encounters between the members ("collisional" system), for example a globular star cluster, it has mere practical reasons to introduce a softened potential. Ideally, one would like to use no softening parameter at all, reproducing the exact level of graininess in the gravitational potential of the system. But often a nonzero softening length is adopted in order to avoid divergent forces during close encounters of two particles as this would result in impractically small time steps. On the other hand, in "collisionless" N-body simulations like large-scale dark-matter-only cosmological simulations of structure formation, the number of particles in the studied physical domain dramatically exceeds the number of particles which can be possibly employed in the simulation. Therefore, the particles do not represent real objects, but are simply assumed to be Monte-Carlo representations of the real underlying, smoother mass distribution.

There are two competing effects in introducing gravitational softening in a collisionless N-body simulation. Too large a value normally leads to a bias in the force field such that physical features on length-scales smaller than the softening length ϵ cannot be resolved. On the other hand, too small a value leads to large small-scale fluctuations in the forces owing to the finite-N representation of the underlying, quasi-continuous density distribution of the system. One finds that the best trade-off is not trivial and there is a rich literature on how to obtain an optimal softening parameter by minimizing the average errors in the force estimation (see, e.g. Merritt 1996; Athanassoula et al. 2000; Dehnen 2001). In particular, the exact value for the optimal softening parameter also depends on the specific analytic form of the softening which is chosen for the simulation.

There are two common types of gravitational softening. The so-called "Plummer softening" was originally suggested by Aarseth (1963) in order to overcome the time-

stepping problems of direct (or "collisional") N-body codes (see below). It approximates each gravitating body with a small Plummer sphere[1] of scale radius ϵ. The gravitational force on particle i due to another particle j at a distance $r_{ij} = |\mathbf{r}_i - \mathbf{r}_j|$ is then given by

$$\mathbf{F}_i = -\mathrm{G}m_i m_j \frac{\mathbf{r}_i - \mathbf{r}_j}{(\epsilon^2 + r_{ij}^2)^{3/2}}. \tag{3.7}$$

In spite of being very simple, the Plummer softening has the drawback that it never converges to the exact Newtonian force law at any given separation r_{ij} of the two bodies. This yields significantly larger errors in the force estimations compared to the "spline softening" methods, used for example in GADGET .

In spline-based softening, a single particle is treated as a "smeared-out", finite-sized object in space. Its extended density distribution is represented by a predefined kernel $W(r, h)$, e.g. in the form of Equation (3.12) given below, which depends on the distance r and the softening length h. Integration over the kernel density distribution gives the fraction of the source particle's mass enclosed by a sphere of radius r_{ij},

$$\begin{aligned} \hat{m}_j(r_{ij}) &= 4\pi \int_0^{r_{ij}} \rho(r) r^2 \mathrm{d}r \\ &= 4\pi \int_0^{r_{ij}} W(r, h_{ij}) r^2 \mathrm{d}r, \end{aligned} \tag{3.8}$$

where we have replaced the density ρ by the kernel function $W(r, h)$ in the second equation. Note that the softening length for two particles in GADGET is usually defined as $h_{ij} = 2.8\,(\epsilon_i + \epsilon_j)/2$.

The corresponding modified force equation for particle i due to particle j is then given by

$$\mathbf{F}_i = -\frac{\mathrm{G}\, m_i \hat{m}_j}{r_{ij}^3}(\mathbf{r}_i - \mathbf{r}_j). \tag{3.9}$$

The kernel formulation has the general advantage that it recovers the exact Newtonian form if $r_{ij} > 2 \cdot \epsilon_{ij}$, where $\epsilon_{ij} \equiv (\epsilon_i + \epsilon_j)\,/2$. Furthermore, the force between two particles decreases to zero with decreasing separation, $r_{ij} \to 0$, since the particle's enclosed mass in Equation (3.8) tends to zero.

3.1.1.2 Planting and Growing a Tree Code

The most direct numerical approach to calculate the gravitational accelerations in an astrophysical N-body system would be a straight-forward summation of Equation

[1]The Plummer sphere was originally introduced, and is still used routinely today, as a few-parameter fitting function to the density distribution of globular clusters (see Plummer 1911).

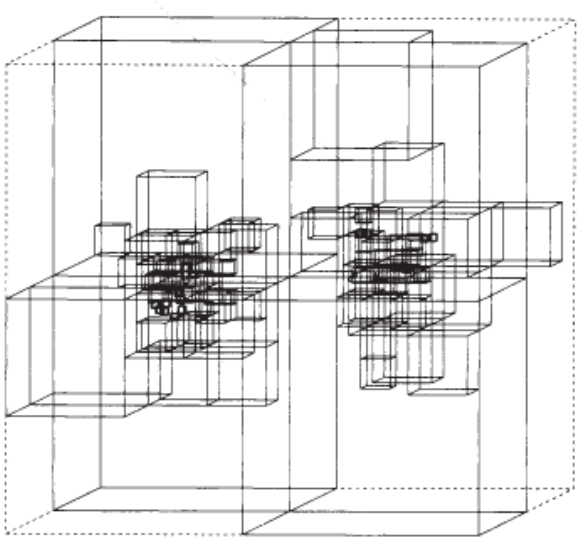

Figure 3.1: Three-dimensional cell structure of an oct-tree. The lines represent the global oct-tree structure of two systems each hosting $N = 64$ particles; taken from Barnes & Hut (1986).

(3.1). This approach is most often called "Direct N-body method" or "Particle-Particle (PP) method" (for a review, refer e.g. to Hockney & Eastwood 1981). However, this approach imposes prohibitively high computational costs with rising particle numbers since the number of numerical operations needed to calculate the accelerations of all N particles increases steeply with $N(N-1) \sim N^2$. Nowadays, the highest-resolution simulations of cosmological structure formation employ typical particle numbers of up to $\gtrsim 10^{11}$ particles (e.g. the "Millennium XXL" simulation, R. Angulo priv. comm.), and up to a few times 10^7 particles if gas physics is included (e.g. the "Eris" simulation by Guedes et al. 2011). These simulations obviously have to be carried out by other code architectures, for example by structuring particles into so-called "hierarchical tree-codes" (see e.g. Appel 1985; Barnes & Hut 1986; Dehnen 2000).

In the hierarchical tree methods, contributions to the forces from nearby particles are calculated via a straight-forward direct summation. At larger distances, however, the gravitational attraction on a single particle due to a group of particles is approximated by a low-order multipole expansion of the group's gravitational potential about its common center of mass. As we will see below, the advantage of a tree code is its faster - albeit approximate - force calculation reducing the computational costs with a much more favorable scaling of only $\sim N \log(N)$. This benefit can be achieved thanks to a novel method of sorting the particles into a hierarchical structure in order to achieve a quick access to single particles or whole particle groups during the force calculation.

There are different approaches of organizing the N particles of a given system in the tree. They are characterized by three main categories. First, this is the type of group-

ing the particles, which itself branches, again, into two categories: the "oct-tree" and the "binary-tree". A comparison between these two schemes may be found in Makino (1990), but we will outline here only the tree algorithm used by GADGET 2 which is based on the so-called "oct-tree" (Barnes & Hut 1986; Barnes 1990). As depicted graphically in Figure 3.1, in this method the tree is constructed by starting from one major cell, which contains all the particles in the system. This "root" cell is then split into eight equal-sized sub-cubes, which themselves are iteratively split into further sub-cubes in the same way. The process continues until each cell contains only one particle, representing a "leaf" of the tree, or no particle at all. The second characteristic is the order of the multipole expansion. While in GADGET 1 the expansion is calculated up to quadrupole order, from GADGET 2 on, only monopole terms are used in the force approximations. Finally, as the third characteristic, when calculating the forces on particle i, an acceptance criterion determines whether the force due to a group of other particles at a certain distance is accepted for the force calculation or whether it has to be broken up further into smaller cells, ultimately reaching single particles in the "leaves" of the tree, if appropriate. Hence, this criterion controls the size of the error introduced into the force calculation by the approximated particle-group interaction, as well as the overall computing time. Hence, for a lower termination of the multipole extension generally a stricter acceptance criterion needs to be chosen to achieve a given accuracy in the force calculations.

The simplest and most intuitive cell-opening criterion is usually defined as

$$R_{\rm crit} \;=\; \frac{l_j}{\theta} + \epsilon, \tag{3.10}$$

where ϵ is the particle's softening length (see Section 3.1.1.1) and l_j the physical size of cell j. The accuracy parameter θ may range between zero and one, and determines the minimum distance $R_{\rm crit}$ at which a cell may be accepted for the force calculation.

However, GADGET employs a slightly more sophisticated cell-opening criterion, after the initial start-up, which is given by

$$\frac{GM_j}{R_{\rm crit}^2}\left(\frac{l_j}{R_{\rm crit}}\right)^2 \;=\; \alpha|\mathbf{a}_i^{\rm old}|. \tag{3.11}$$

Here, M_j is the mass of cell j and $\mathbf{a}_i^{\rm old}$ is the particle's acceleration at the last time step. The advantage of this definition owes to the fact that the cell-opening criterion is not defined geometrically fixed, but may also adapt to the dynamics of the system.

Despite some overheads due to periodic updates and reconstructions of the tree structure, hierarchical tree-codes have led to huge savings in computing time since both tree construction and force evaluation require an order of $\sim \mathcal{O}(N(\log N))$ operations compared to $\sim \mathcal{O}(N^2)$ for the direct summation.

3.1.2 The Smoothed Particle Hydrodynamics Method

The last Section has outlined the calculation of gravitational forces for a system of N gravitationally interacting point masses. In the presence of fluids, however, one also needs to take into account hydrodynamical equations to describe the motions of the fluid. In Gadget, this is done with the so-called "smoothed particle hydrodynamics" (SPH) method. SPH is a conceptually simple, yet powerful method to numerically solve the hydrodynamic equations of a compressible fluid in a Lagrangian formulation. It was first introduced by Lucy (1977) and Gingold & Monaghan (1977). Unlike other numerical methods for hydrodynamics, such as grid-based fluid solvers, SPH is an inherently adaptive method due to its Lagrangian nature. This advantage automatically provides high resolution "where it is needed the most", i.e. in high-density regions, while saving computational effort in regions of nearly empty space. However, this is done at the cost of comprising some resolution in these low-density regions.

In SPH, thermodynamic quantities are represented by discrete interpolation points, each characterized by its position $\mathbf{r}_i$, velocity $\mathbf{v}_i$, and a fixed mass m_i, which may be best thought of as discrete "fluid particles" spread out over some finite-sized region, and moving with the flow. Thermodynamic quantities are then estimated by interpolating over neighboring particles as summarized below.

However, since SPH is not a unique method, we note that there exist many different notations (for detailed reviews we refer the reader to Monaghan 1992 and Price 2005). Here we outline the formulation used in Gadget 2 and Gadget 3 (see Springel 2005), and follow the derivation of the basic equations as detailed in Springel & Hernquist (2002). This particular implementation of the SPH formalism has the advantage that it is strictly entropy-conserving and, in addition, energy-conserving in the case of freely adapting smoothing lengths.

In Gadget, the following spline-based SPH smoothing kernel is used for the interpolation of thermodynamic quantities and the computation of softened gravitational forces (see Section 3.1.1.1)

$$W(r,h) = \frac{8}{\pi h^3} \begin{cases} 1 - 6\left(\frac{r}{h}\right)^2 + 6\left(\frac{r}{h}\right)^3, & 0 \leqslant \frac{r}{h} \leqslant \frac{1}{2}, \\ 2\left(1 - \frac{r}{h}\right)^3, & \frac{1}{2} \leqslant \frac{r}{h} \leqslant 1, \\ 0, & \frac{r}{h} > 1. \end{cases} \tag{3.12}$$

Consequently, the density estimate is obtained as the weighted sum over all N neighboring particles, written as

$$\rho_i \;=\; \sum_{j=1}^{N} m_j \, W(|\mathbf{r}_{ij}|, h_i), \tag{3.13}$$

where $W(r,h)$ is the SPH smoothing kernel as defined in Equation (3.12), and h_i is the adaptive SPH smoothing length of particle i. The smoothing length h_i defines the radius of the region over which the neighboring N particles are sampled, and the number of nearest neighbor particles is kept fixed at a typical value, e.g. 64 ± 5 in our GADGET runs.

The pressure P_i of particle i is set using the equation of state of an ideal gas

$$P_i = A_i \, \rho_i^{\gamma}, \tag{3.14}$$

where $\gamma = 5/3$ is the adiabatic gas index and $A \equiv P/\rho^{\gamma}$ is the "entropic function". Since $A = A(S)$ is a pure function of the entropy S for an ideal gas, it is directly used as the independent thermodynamical variable in GADGET instead of the entropy. The internal energy per unit mass u may then be calculated via

$$u = \frac{A}{\gamma - 1} \rho^{\gamma - 1}. \tag{3.15}$$

For SPH particles, the momentum equation, has to be extended from its form given in Equation (3.3) in order to account for the hydrodynamical accelerations. This is written as

$$\left. \frac{d\mathbf{v}_i}{dt} \right|_{\rm hydro} = - \left(\frac{\nabla_i P_i}{\rho_i} \right) + \left. \frac{d\mathbf{v}_i}{dt} \right|_{\rm visc}. \tag{3.16}$$

The first term in Equation (3.16) is estimated via

$$\left(\frac{\nabla_i P_i}{\rho_i} \right) = \sum_{j=1}^{N} m_j \left[f_i \frac{P_i}{\rho_i^2} \nabla_i W_{ij}(h_i) + f_j \frac{P_j}{\rho_j^2} \nabla_i W_{ij}(h_j) \right], \tag{3.17}$$

where the additional coefficients f_i are defined as

$$f_i = \left(1 + \frac{h_i}{3\rho_i} \frac{\partial \rho_i}{\partial h_i} \right)^{-1}, \tag{3.18}$$

and $W_{ij}(h)$ is a short notation for $W(|\mathbf{r}_{ij}|, h)$.

However, in order to capture the effects of dissipative effects, e.g. in shocks, which drive the conversion of kinetic energy into heat, an additional viscous force has to be introduced in SPH. It takes the form

$$\left. \frac{d\mathbf{v}_i}{dt} \right|_{\rm visc} = - \sum_{j=1}^{N} m_j \Pi_{ij} \nabla_i \bar{W}_{ij}, \tag{3.19}$$

where $\bar{W_{ij}} = \frac{1}{2}(W_{ij}(h_i) + W_{ij}(h_j))$. The artificial viscosity is expressed via

$$\Pi_{ij} = \frac{\alpha}{2} \frac{(c_i + c_j - 3w_{ij})\, w_{ij}}{\rho_{ij}}. \tag{3.20}$$

In the latter equation, c_i and c_j denote the sound speeds of particle i and j, respectively, and $w_{ij} = \mathbf{v}_{ij} \cdot \mathbf{r}_{ij}/|\mathbf{r}_{ij}|$ only if $\mathbf{v}_{ij} \cdot \mathbf{r}_{ij} < 0$, i.e. when the particles have convergent flows. Otherwise w_{ij}, and hence Π_{ij}, are set to zero. The artificial bulk viscosity constant α is typically chosen with values ranging between $\alpha \simeq 0.5 - 1.0$. We adopt a value of $\alpha = 0.75$ throughout the studies presented here.

In the absence of dissipative terms such as shocks or external heat sources, the entropy A_i of a particle remains constant in the flow. Hence, in these cases the only mechanism to generate entropy in SPH is by means of the artificial viscosity. This is done at a rate

$$\frac{dA_i}{dt} = \frac{1}{2} \frac{\gamma - 1}{\rho_i^{\gamma-1}} \sum_{j=1}^{N} m_j\, \Pi_{ij}\, \mathbf{v}_{ij} \cdot \nabla_i \bar{W}_{ij}. \tag{3.21}$$

The signal speed between two particles in the flow is limited by a maximum signal velocity, which is generally estimated as $v_{ij}^{\rm sig} = c_i + c_j - 3w_{ij}$ (Monaghan 1997, cf. also Equation (3.20)). This condition naturally yields a Courant-Friedrichs-Lewy (CFL) criterion, which ensures that information is not propagated further than a fraction $C_{\rm CFL}$ of the particle's smoothing length, h_i, in one time step (Courant et al. 1928). This additional time step criterion for SPH particles then simply reads

$$\Delta t_i|_{hydro} = \frac{C_{\rm CFL}\, h_i}{\max_j(c_i + c_j - 3w_{ij})}, \tag{3.22}$$

where the maximum $\max_j$ is determined with respect to all N neighbors of particle i. A reasonable range for the $C_{\rm CFL}$ parameter is generally chosen between $0.1 \lesssim C_{\rm CFL} < 0.5$. We have used a conservative value of $C_{\rm CFL} = 0.15$ throughout this Thesis. The next time step of an SPH particle is then ultimately determined by the minimum over all limiting time steps defined in Section 3.1.1 and Equation (3.22).

Finally, Gadget uses an additional viscosity limiter to prevent spurious entropy generation and unphysical angular momentum transport in shear flows (Balsara 1995; Steinmetz 1996). To this end, the viscous tensor Π_{ij} is multiplied with the factor $(f_i + f_j)/2$, where the form factor f_i is given as

$$f_i = \frac{|\nabla \times \mathbf{v}|_i}{|\nabla \cdot \mathbf{v}|_i + |\nabla \times \mathbf{v}|_i}. \tag{3.23}$$

In the latter, standard estimates for the divergence and curl have to be used (see, e.g. Monaghan 1992).

3.1.3 Additional Physical Modules

Besides a self-consistent treatment of the gravitational and hydrodynamical forces, GADGET offers implementations for a number of other physical processes, which are relevant to galaxy evolution. Here, we will give a short summary of the particular models we have used in this work. For a more complete overview we refer the reader to the cited literature of any specific model.

Following Katz et al. (1996), radiative cooling and heating is computed for an optically thin plasma out of primordial hydrogen and helium, assuming collisional equilibrium. As a source of heating, a local spatially uniform time-independent photo-ionizing UV background is taken into account, which is assumed to arise from quasi-stellar objects (QSOs) and star-forming galaxies (Haardt & Madau 1996).

Star formation, together with associated supernova feedback is assumed to effectively heat and pressurize the surrounding ISM. It is modeled following the sub-grid multiphase prescription proposed by Springel & Hernquist (2002). In this model, the star-forming ISM is treated as an effective two-phase fluid, where cool dense clouds are embedded in a hot ambient medium assuming pressure equilibrium between the phases. This approach attempts to mimic some of the key aspects of the theoretical picture of a multi-phase ISM (McKee & Ostriker 1977), where hot gas is assumed to develop a run-away cooling instability if it exceeds a certain density threshold, $\rho > \rho_{\rm crit}$. Stars are subsequently formed from cold clouds satisfying the above condition on a characteristic star formation timescale $t_\star$ and instantaneously return mass and supernova energy from massive short-lived stars ($M_\star > 8\,{\rm M}_\odot$) to the surrounding ISM. Adopting a Salpeter initial mass function (IMF; Salpeter 1955), the fraction of massive stars has a value of approximately $\beta = 0.1$, and the energy released to heat the ambient medium per supernova explosion is chosen to take a canonical value of 10^{51} erg. The SFR then simply reads

$$\frac{d\rho_\star}{dt} = \frac{\rho_c}{t_\star} - \beta\frac{\rho_c}{t_\star} = (1-\beta)\,\frac{\rho_c}{t_\star}, \tag{3.24}$$

where ρ_c and $\rho_\star$ are the densities of stars and cold gas, respectively, and the threshold density is determined self-consistently in our simulations by requiring the effective equation of state to be continuous at the onset of star formation. Adopting a characteristic star formation timescale of $t_\star = 2.1\,{\rm Gyr}\cdot(\rho/\rho_\star)^{-1/2}$, the above relation is tuned such as to recover the observed Kennicutt-Schmidt "law" (Kennicutt 1998, see Springel & Hernquist 2003, Figure 2).

The mass and energy transfer between the hot and cold phases establishes a tightly self-regulated star formation prescription, where cloud condensation by cooling and subsequent star formation are efficiently balanced by the heating of the diffuse ISM and the evaporation of cold clouds through the thermal energy injected in supernovae explosions. The basic bookkeeping for the evolution of the densities in the cold and hot

phases, respectively, is given by the respective rate equations (Springel & Hernquist 2002)

$$\frac{d\rho_c}{dt} = -\frac{\rho_c}{t_\star} - A\beta\,\frac{\rho_c}{t_\star} + \frac{1-f}{u_h-u_c}\Lambda_{\rm net}(\rho_h,\rho_c), \quad \text{and} \tag{3.25}$$

$$\frac{d\rho_h}{dt} = \beta\frac{\rho_c}{t_\star} + A\beta\,\frac{\rho_c}{t_\star} - \frac{1-f}{u_h-u_c}\Lambda_{\rm net}(\rho_h,\rho_c), \tag{3.26}$$

where ρ_h is the density of the hot component, and $A \propto A_0\,\rho^{-4/5}$ governs the cloud evaporation. The thermal energy per unit mass of the hot and cold component are given by u_c and u_h and $\Lambda_{\rm net}(\rho_h,\rho_c)$ is the net cooling function in the presence of an external UV background (Katz et al. 1996). The latter terms in Equations (3.25) and (3.26) treat the growth of cold clouds via the thermal instability occurring at densities above the density threshold $\rho_{\rm crit}$, where $f = 0$ is set, and $f = 1$ otherwise. On the other hand, the first terms in Equations (3.25) and (3.26) describe the net mass transfer due to star formation and the instantaneous stellar feedback.

The thermal energy per unit volume $\epsilon_{\rm th} = \rho_c u_c + \rho_h u_h$ of the gas phase then evolves according to

$$\frac{d}{dt}\left(\rho_c u_c + \rho_h u_h\right) = -\Lambda_{\rm net}(\rho_h,\rho_c) + \beta\frac{\rho_c}{t_\star}u_{\rm SN} - (1-\beta)\,\frac{\rho_c}{t_\star}u_c, \tag{3.27}$$

where $u_{\rm SN}$ represents the amount of supernova energy feedback to the surrounding ISM.

As a result of the thermal feedback, the star-forming, dense part of the ISM is assumed to develop a two-phase medium which may be described by an effective equation of state of the form

$$P_{\rm eff} = (\gamma-1)\,\rho\,u_{\rm eff}, \tag{3.28}$$

with $u_{\rm eff} = ((1-x)\,u_h + x\,u_c)$ and x being the mass fraction in cold, star-forming clouds. This effective equation of state is quite "stiff", providing a high, steeply rising pressure support with increasing density. This effectively leads to a self-regulated formulation of the star formation and the associated stellar feedback. However, one is free to control the efficiency of the thermal feedback via a further dimensionless parameter $q_{\rm EQS}$ that interpolates the star formation model between the full "stiff" feedback model ($q_{\rm EQS} = 1.0$) and a "soft" isothermal equation of state with $T = 10^4$ K ($q_{\rm EQS} = 0$, see Springel et al. 2005).

In this Thesis, we generally set the parameters governing the multi-phase SF model such as to ensure a SFR of $\sim 1\,\mathrm{M}_\odot\,\mathrm{yr}^{-1}$ for an isolated Milky-way like galaxy in the simulations (see also Chapters 5 - 7). For that we choose parameters for the star formation timescale $t^0_\star = 8.4\,\mathrm{Gyr}$, the cloud evaporation $A_0 = 4000$, and a supernova "temperature" of $T_\mathrm{SN} = 10^8$ K, respectively. Cold dense gas is assumed to reside in clouds with temperature $T_\mathrm{cold} = 1000$ K. Given this parameter choice and requiring that the equation of state is continuous at the onset of star formation, the critical hydrogen number density is set to $n_\mathrm{crit} = 0.128\,\mathrm{cm}^{-3}$.

3.2 Radiative Transfer Simulations

In Chapter 5, we compare synthetic FIR maps from our Antennae models to recent data by Klaas et al. (2010), obtained with the Herschel-PACS instrument. We describe here the post-processing procedure applied to our simulations to construct the synthetic FIR maps.

FIR emission from the galaxy is dominated by thermal emission from dust that has been heated by stellar radiation. Due to strong spatial fluctuations in both dust density and stellar emission, the dust temperature varies in a very complicated manner. To produce accurate FIR maps of the galaxy it is therefore necessary to run 3D radiative transfer (RT) simulations of the SPH galaxy model.

Maps are produced by post-processing SPH snapshots with the dust RT code (kindly provided by Lunttila et al., in preparation). This code is based on the Monte-Carlo RT code by Juvela (2005), though much of it has been re-written. Before the RT calculations the SPH snapshot is gridded adaptively onto a mesh refinement grid using the SPH smoothing kernel (Section 3.1.2). The use of an adaptive grid enables good spatial resolution in the dense inner parts of the galaxy while keeping the total number of computational cells in the grid low. In the simulations described in this paper the size of the parent grid is 80 kpc while the minimum cell size is 78.125 pc, resulting in an effective resolution of 1024^3. The total number of cells in the mesh refinement grid is approximately 2×10^6.

Interstellar dust is assumed to be uniformly mixed with the gas, and a single dust model is used in the whole galaxy. The dust is assumed to have average properties as found in the Milky Way (Draine 2003)[2], with gas-to-dust ratio of 124 and $R_\mathrm{V} \equiv \frac{A_\mathrm{V}}{E(B-V)} = 3.1$, where A_V is the V-band extinction and $E(B-V)$ defines the "color excess". Stellar emission is modeled by assigning (Bruzual & Charlot 2003) spectral energy distributions (SEDs) to all star particles according to their ages. Because our N-body+SPH simulations do not track metallicity, $Z = 0.02$ is assumed for all

[2]http://www.astro.princeton.edu/?/draine/dust/dustmix.html

stellar particles, i.e. disk, bulge, and newly formed stellar particles. Stellar particles existing at the start of the SPH simulation are assigned ages uniformly distributed between 0 and 4 Gyr for the disk stars and between 3 and 7 Gyr for the bulge. After the dust distribution and radiation sources are set up, the RT simulation is used to calculate the dust equilibrium temperatures. The calculation is run iteratively to account for the dust self-absorption and heating, until the dust temperatures have converged.

As a final step in the RT simulations, 70 μm, 100 μm, and 160 μm maps are produced using the previously computed dust temperatures. The maps are then convolved to the resolution of the Herschel PACS instrument at the corresponding wavelengths to simulate the observations by (Klaas et al. 2010). The full-width-half-maximum (FWHM) of the point-spread function (PSF) is 5″.5, 6″.8, and 11″.8 in the 70 μm, 100 μm, and, 160 μm bands, respectively.

3.3 Disk Galaxy Models

In the previous sections, we introduced the different numerical techniques that we use in the high-resolution major merger simulations of the Antennae throughout this Thesis, along with a number of parameters needed to run the codes. In this Section, we will give an overview of the generation of initial conditions of disk galaxy models.

To set up the galaxies in our simulations, we use self-consistent, equilibrium galaxy models following the method detailed in Springel et al. (2005). These galaxy models are motivated by, and consistent with, current cold dark matter (CDM) cosmologies. We specifically aim to establish progenitor galaxy models which are chosen less 'ad hoc' than most of the previous numerical studies of the Antennae galaxies (see Section 2.3).

The galaxy's total mass and virial radius are given in terms of the "virial velocity", v_{200} by the following relations

$$M_{200} = \frac{v_{200}^3}{10\,G H_0} \quad \text{and} \tag{3.29}$$

$$r_{200} = \frac{v_{200}}{10\,H_0}, \tag{3.30}$$

respectively. Here, the virial velocity denotes the circular velocity at radius r_{200}, defining the radius at which the mean enclosed dark matter density equals 200 times the critical density of the Universe (Mo et al. 1998). The present-day Hubble parameter is set to a value of $H_0 = 71$ km s^{-1} Mpc $^{-1}$ consistent with the observed value of $H_0 = 71.0 \pm 2.5$ km s^{-1} Mpc $^{-1}$ from the year seven Wilkinson Microwave Anisotropy Probe ("WMAP") data release (Komatsu et al. 2011; Jarosik et al. 2011).

Each galaxy consists of a rotationally-supported gaseous and stellar disk component, a non-rotating stellar bulge, and a massive dark matter halo. The cold dark matter halo is modeled using an analytical Hernquist (1990) profile, associated with a corresponding Navarro et al. (1997, "NFW") dark matter profile by requiring that the inner density profiles should be equal for both profiles, enclosing the same mass within the virial radius r_{200}. The NFW profile is motivated from fitting the density profiles of dark-matter-only cosmological simulations. It is defined by only two parameters: its virial radius r_{200} and the concentration parameter $c = r_{200}/r_{\rm s}$, where $r_{\rm s}$ is the scale length of the profile.

Embedded in the dark matter halo is a rotationally supported disk with an exponential surface density profile of scale length $r_{\rm disk}$,

$$\Sigma_{\rm disk}(r) = \frac{M_{\rm disk}}{2\pi r_{\rm disk}^2} \exp(-r/r_{\rm disk}), \tag{3.31}$$

which comprises a constant fraction $m_{\rm disk}$ of the total mass such that the total disk mass is $M_{\rm disk} = m_{\rm disk} M_{200}$. A fraction of the disk mass, $f_{\rm g}$, again, is converted into SPH particles, while the rest of the disk remains in stars[3]. The disk scale length $r_{\rm disk}$ is determined by using the Mo et al. (1998) formalism under the assumption that the fractional disk angular momentum $j_{\rm disk}$ equals the disk mass fraction $m_{\rm disk}$ for a given halo spin parameter λ. This assumption of $J_{\rm disk} = j_{\rm disk} J_{halo}$ ($j_{\rm disk} = m_{\rm disk}$) corresponds to the conservation of the specific angular momentum of the material that forms the disk. The vertical scale height z_0 of the stellar disk is taken to be radially constant and is typically set to $z_0 = 0.2\, r_{\rm disk}$, while the radial velocity dispersion is set equal to the vertical velocity dispersion. The equilibrium structure of the gas disk and the corresponding gas temperature are mainly fixed by the adopted equation of state rather than by the velocity dispersion, where the vertical scale height of the gas disk is computed self-consistently for a given surface density by balancing the galactic potential with the pressure given by the (effective) equation of state of the multi-phase ISM model (Springel & Hernquist 2002). Finally, our galaxy models contain a non-rotating stellar Hernquist (1990) bulge with a total mass fraction $m_{\rm bulge}$, such that $M_{\rm bulge} = m_{\rm bulge}\, M_{200}$. The bulge scale length $r_{\rm bulge}$ is fixed to $0.2\, r_{\rm disk}$ in all simulations.

It is crucial that the galaxy models, while set-up formally in an equilibrium state, actually stay in approximate equilibrium if evolved in isolation, unperturbed by any external forces. To test this, we have evolved the initial conditions of the two progenitor galaxies of our best fitting model (see Chapter 4) in isolation for a total time of 2 Gyr.

[3] Alternatively, the gas mass fraction can also be distributed in a "flat" gaseous disk component with cut-off radius $r_{\rm cut}$. This is motivated by observations of the distribution of the neutral gas component in the Milky Way (e.g., Dame 1993, but see also Kalberla & Dedes 2008). We have performed tests where we adopted flat gas distributions or a combination of flat and exponential gas distributions in our simulations. However, we did not find any improvements in our best match to the Antennae galaxies, and, therefore, discarded these models.

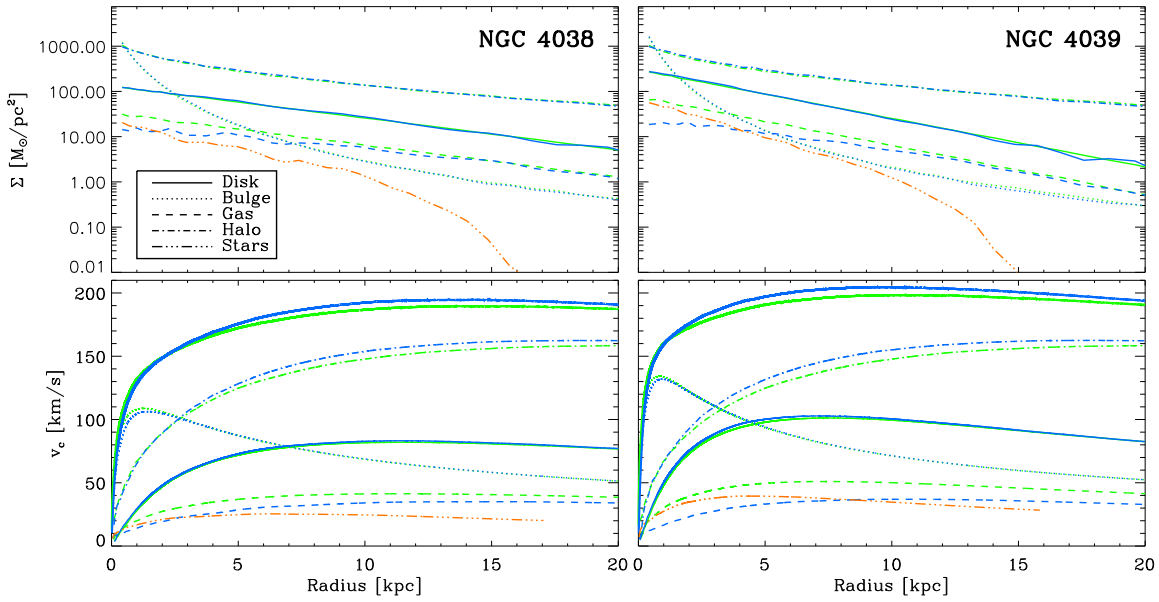

Figure 3.2: Disk profiles for the fiducial galaxy models of NGC 4038 *(left panels)* and NGC 4039 *(right panels)*. Initial (green) and evolved (blue) surface density profiles *(upper panels)* and rotation curves *(lower panels)* are compared for the different galaxy components: dark matter halo, stellar and gaseous disk, and bulge. Additionally, newly formed stars are indicated in yellow, and the total rotation curve is given by the thick upper solid line in the lower panels.

The progenitors for NGC 4038 and NGC 4039 are set up using identical parameters except for the halo spin parameter λ, which directly influences the disk scale length of the galaxies (see Equation 29 f. Mo et al. 1998). Our choice of $\lambda_{4038} = 0.10$ and $\lambda_{4039} = 0.07$ yields disk scale lengths of $r_{\rm disk}^{4038} = 6.28\,{\rm kpc}$ and $r_{\rm disk}^{4039} = 4.12\,{\rm kpc}$, respectively (see also Tables 4.2 and 5.1 in Chapter 4). In Figure 3.2 we compare the radial surface density profiles (upper panels) and rotation curves (lower panels) of both galaxies in their initial state (green) and after evolution for two Gyr (blue) for the different galactic components: the dark matter halo, the bulge and disk stars, and the gas disk. We have also included star formation in the simulations in order to keep the same (initial) pressure support to the gas disks that were assumed while generating the initial conditions (see above). For a better distinction, the radial profiles of the newly formed stars are colored in yellow. New stellar particles are formed mainly in the galactic centers, where the gas densities are highest. The surface densities of all dissipation-less, non-radiating galactic components remain very nearly constant within the inner 20 kpc throughout the entire 2 Gyr of evolution. The surface densities of the initial and final gas disks, however, differ due to the combined effect of a viscous angular momentum transport, driving gas outwards to larger radii, and the formation of new stars in the centers. Still, the combined surface densities of the final gas disks and the newly formed stars add up to recover the initial gas density profile to within $\lesssim 30$ per cent at all radii and for both disks. A little further out, between radii of $20-40\,{\rm kpc}$ (not shown here) spiral

patterns make the surface density profile of the evolved stellar disk oscillate slightly around the initial profile, by less than a factor of 2. Also the rotation curves of both disks stay reasonably constant with deviations $\lesssim 5\,\mathrm{km\,s^{-1}}$, except for a slight increase ($< 10\,\mathrm{km\,s^{-1}}$) in the dark halo, indicating a redistribution of dark matter mass within the inner $\sim 25\,\mathrm{kpc}$. The latter is also mainly reflected in the total rotation curves, given by the thick upper solid lines in the lower panels of Figure 3.2. The gas velocity profile has, again, flattened according to the change in the gas density profiles discussed above.

Additional information about the specific parameter choice defining the structure of our adopted model galaxies are also given at the appropriate places in Chapters 4 - 7.

Chapter 4

Towards a new Model for the Antennae Galaxies

There are basically two complementary approaches in finding a theoretical model for a specific observed system like the interacting Antennae galaxies. One could be called the 'agnostic' method, where a large number of theoretical models is generated, automatically at best, and compared to a subset of the system's properties which are required to be met in order to obtain a "good match". An example of this approach would be the application of automated searches such as the "genetic algorithm" described in Section 4.2.2. The other method is to extract a priori all information that is needed for the parameter choices of the adopted physical and numerical models from the available observational data and run the best possible "replica of nature" on the computer. In practice, however, this is not easily possible due to e.g. missing observational data or short-comings in the physical models themselves, such that we have to resort to a compromise of the two approaches. Thus, in this Thesis, we followed a modeling approach that largely uses parameter choices motivated by observations, combined with a large parameter survey of self-consistent numerical simulations in order to constrain unknown model parameters.

In this Chapter, we describe our modeling approach to find a suitable numerical representation of the Antennae galaxies. First, we give an overview of the basic modeling procedure and discuss some modeling techniques which may have the potential to facilitate similar modeling efforts in the future in Sections 4.1 and 4.2, respectively. In Section 4.3, we will then concentrate specifically on how we obtained our fiducial best-matching model of the Antennae, including a detailed summary of our parameter choices.

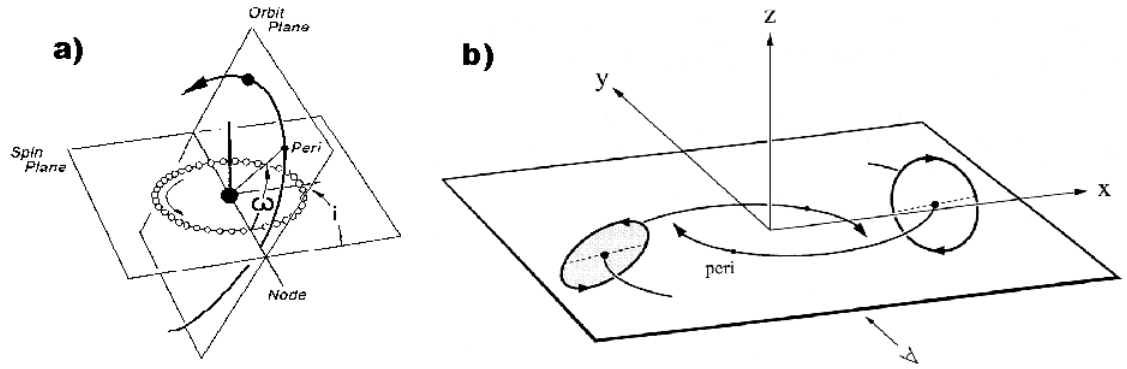

Figure 4.1: Orbital geometry of the idealized binary merger. *Left panel:* disk orientations, *right panel:* initial Keplerian two-body orbit. Adaption of Figure 6a from Toomre & Toomre (1972) and Figure 1 from Barnes (1988).

4.1 Merger Orientation, Orbit & Analysis

The first step in modeling specific pairs of interacting galaxies clearly lies in specifying suitable galaxy models for the two progenitor galaxies. This includes setting a number of ~ 10 parameters per disk galaxy model (see Section 3.3 and Table 4.2). The actual matching procedure, however, requires a number of further steps, each of which consists of guessing the most appropriate choice for a set of parameters and comparing the final outcome to the available observational data. This process is iterated with new (improved) initial conditions, until a satisfactory match to the real system is obtained. One cycle in the matching process consists of the following three main steps:

1. setting up an analytical initial two-body orbit of the two galaxies (see right panel of Figure 4.1),

2. specifying the orientation of the disks, i.e. the spin vector of the disks with respect to each other and to the orbital plane (see left panel of Figure 4.1),

3. and, after running a simulation, comparison of the simulation results to a set of observed quantities, i.e. "observing" the simulated data.

In this Section we want to address shortly the parameter space involved in each of the three steps. We will discuss some of the short-comings and possible improvements of our approach in Section 4.2.

First, we set up the initial conditions for the binary interaction orbit of the two galaxies. In our case, the galaxies are put on initially nearly Keplerian two-body or-

bits, which are defined by a total of *three* parameters: the ellipticity e, the mass ratio of the two galaxies $\mu \equiv M_1/M_2$, and the distance at closest approach between the two galaxies, $r_{\rm p}$[1]. Typically we choose a mass ratio $\mu = 1$, motivated by the relative luminosities of NGC 4038 and NGC 4039 (see Section 4.3.1), and a pericentric distance of the order of the combined disk scale lengths of the two progenitor galaxies, $r_{\rm p} = r_{\rm disk,1} + r_{\rm disk,2}$. Note, however, that we put the galaxies only on "nearly-parabolic" orbits in the sense that we use only a fraction of the total dynamical mass (in our case typically $\sim 1/2$) when calculating the initial velocities. This accounts for the fact that the galactic halos are sampled over such a large initial space that they already overlap at the beginning of the simulation. As a result, our initial two-body orbits are bound, with orbital eccentricities of $e \lesssim 1$. This is in very good agreement with statistics from cosmological N-body simulations (Khochfar & Burkert 2006).

In a further step we choose the initial "spin" vector, specified by a pair of angles per disk, which rotate the galaxies with respect to the angular momentum vector of the orbit and the vector connecting the two galaxies at their closest approach (see left panel in Figure 4.1). These angles are called the disk "inclination" $i_{\rm i}$ and "argument of pericenter" $\omega_{\rm i}$ ($i = 1, 2$) and constitute another *four* parameters needed to be chosen *before* running the simulation.

After the simulation run has been completed we compare the simulation results to the interacting system. To this end, at a given assumed time of best match $t_{\rm BM}$, we choose a grid of different viewing directions onto the system, defined by a set of three angles (θ,ψ,ϕ) that specify a series of subsequent rotations around the x-, y-, and z-axis. In addition, we apply length ($\mathcal{L}$) and velocity ($\mathcal{V}$) scale factors and choose a common center $[X_C, Y_C]$ in the plane-of-the-sky and a systemic line-of-sight velocity $v_{\rm sys}$ in order to map the simulated positions and velocities to the observed system. With these additional *nine* parameters, a total of at least *sixteen* parameters is needed to describe a successful match to a system of two interacting disk galaxies.

4.2 Discussion of Modeling Techniques

The huge parameter space involved in the modeling process unfortunately sets strict constraints on the range of parameters that can be investigated in a reasonable amount of time (such as a PhD project) and illustrates the complexity of the subject. Although intuition and experience of the simulator may narrow down the parameter sub-space that needs to be probed, it is not surprising that detailed parameter studies are scarce

[1]Strictly speaking, the initial separation, $r_{\rm sep}$, has to be chosen as well. But, if chosen sufficiently large such that tidal forces between the galaxies are only of minor importance at the beginning of the simulation, the exact outcome of the simulations should be insensitive to the exact initial value. This is why we do not consider it as a free parameter. In our runs, we generally adopt a distance of one virial radius $r_{\rm sep} = r_{200}$ for the initial separation.

or only cover very small domains of the available parameter space. This is one of the major reasons, apart from uncertainties in the physical models themselves, why the theoretical knowledge often lags greatly behind the information available from modern high-resolution multi-wavelength observations (see Sections 2.2 and 2.3).

Although more time-consuming than simplified numerical techniques such as, e.g. restricted three-body codes (see Section 2.1), we decided to use fully self-consistent N-body + hydrodynamical simulations for our match of the Antennae to reliably model the morphology and kinematics of the gas component. Furthermore, since we want to investigate the overlap starburst, we also include star formation (Section 3.1.3) from the very start of the survey, allowing for additional constraints on the robustness of our models (see Chapter 5 for the results) This approach gives the most accurate and reliable results with respect to the orbital decay and disk self-gravity during the encounter, facilitating a detailed comparison with observations of the HI velocity fields and star formation in the Antennae. Starting with models based on the orbital parameters derived by Toomre & Toomre (1972), galaxy models by Barnes (1988), and further guidance from numerical investigations on the development of tidal tails in dark matter halos (Dubinski et al. 1999; Springel & White 1999), we continued running the simulations, analyzing them using especially developed interactive software, and guessing improved initial conditions in an iterative circle (see, e.g. Karl et al. 2008), until we obtained a satisfactory match to the observations (see Karl et al. 2010; Section 4.3).

4.2.1 Finding the Right Orientation with the "Identikit" Method

A recent improvement having the potential of alleviating some of the time burden in our approach, has been proposed by the "Identikit" method (Barnes & Hibbard 2009; Barnes 2011). These algorithms are designed to rapidly explore the parameter space of the possible disk orientations in binary spiral-spiral encounters by combining self-consistent and test-particle techniques. In "Identikit 1" (Barnes & Hibbard 2009), an idealized test galaxy is represented by a distribution of massive particles that are put into a Hernquist (1990) bulge, an exponential disk, and a tapered NFW dark matter halo profile. In addition, all profiles are converted into a spherical (!) cumulative mass profile $M(\mathbf{r}) = M_{\rm bulge}(\mathbf{r}) + M_{\rm disk}(\mathbf{r}) + M_{\rm halo}(\mathbf{r})$. The corresponding spherically symmetric distribution function is calculated using "Eddington's Formula" (Eddington 1916; see also Binney & Tremaine 2008, Chapter 4, p. 237) given by

$$f(E) \;=\; \frac{1}{\sqrt{8}\pi^2}\frac{d}{dE}\int_0^E \frac{d\rho}{d\Phi}\frac{d\Phi}{\sqrt{E-\Phi}}, \tag{4.1}$$

with E and Φ being the total energy and the galactic potential, respectively. This allows to follow the time-dependent potential and orbital decay of the merging galaxies in a self-consistent way. Embedded in this spherical mass profile is a spherical configuration of massless test-particles on initially circular orbits which are randomly

distributed over all directions by drawing their normalized angular momentum vectors $\hat{\mathbf{s}}_\mathrm{i}$ uniformly from the unit sphere. Test particles within a range of initial normalized spin vectors are thought to represent a disk with a unique normalized spin vector $\hat{\mathbf{s}}_\mathrm{disk}$ if they fulfill the relation $1 - \hat{\mathbf{s}}_\mathrm{disk} \cdot \hat{\mathbf{s}}_\mathrm{i} \leq \sigma$, where σ is a user-defined tolerance parameter. During the encounter, the test-particles feel the tidal forces of the intruder galaxy and may serve as simple, purely ballistic, kinematic tracers of the encounter. The main advantage of the Identikit method is its possibility to probe at once basically *all* possible disk configurations after running only one self-consistent simulation. Hence, having adopted appropriate galaxy models for the two progenitor galaxies, this leaves the experimenter with only *three* parameters, which have to be chosen before running the simulation: the eccentricity e, the mass ratio μ, and the pericentric distance r_p. In principle, this should greatly reduce the number of simulations needed to obtain a decent match. A schematic drawing of the Identikit approach can be seen in Figure 4.2.1. The parameter space of the initial disk configurations, indicated by the polar coordinate, can be explored "a posteriori", after running just one single simulation. In addition, a graphical analysis program is provided, which allows to interactively vary the disk orientation, the viewing angle, the scale factors and position-velocity centroids, along with the time of best match. However, while Identikit may be a quick way to narrow down the parameter range, it should be followed up by self-consistent simulations due to some main limitations of this method. First, due to the lack of self-gravity, features like swing-amplified spirals and bars cannot be reproduced by the test particles. Moreover, while the orbital decay is followed to a certain degree by the massive spherical halos, its dependence on the actual disk orientation is neglected, which can have an effect on the time of best match (measured as the time since last pericenter) of the order of $\sim 10\%$ (e.g. White 1979). Finally, as stated above, the model disks in Identikit are purely collision-less, while the observations usually use different gas phases (e.g. HI , CO, etc) to trace the kinematics of interacting systems, where dissipative effects may change the physical state of the gas. This may lead to slight mismatches due to, e.g. offsets between stellar and gaseous tidal arms (Mihos 2001) or a smaller range in the gas rotation velocities of the real galaxies due to the dissipative nature of the gas.

Currently, there are modeling efforts underway trying to reproduce the fiducial parameters we have found in our Antennae simulations (see, e.g. Table 4.2), using the Identikit method (Lisa Chien, private communication).

4.2.2 Automated Searches - Finding a Measure for the "Goodness-of-Fit"

Apart from low computational costs, another desirable property not accounted for in our present modeling approach would be to have a subjective quantitative measure for the "goodness-of-fit" between the model and the observed data, and for the uniqueness of the best model. An approach, which addresses these problems, is realized by

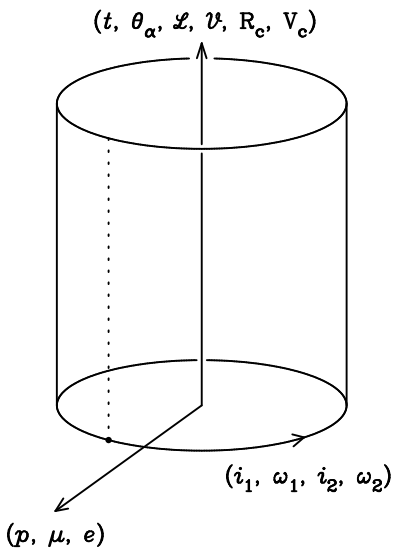

Figure 4.2: Schematic representation of the three parameter groups involved in the modeling of galaxy interactions. In a conventional simulation, the interaction orbit (*radial coordinate*) and the disk orientations (*polar coordinate*) have to be chosen before running the simulation. The parameter space explored in this way is indicated by the dotted line. Using the Identikit method, on the other hand, a single simulation covers the whole polar surface ("mantle") of the cylinder, leaving only the orbital parameters to be chosen before the simulation (image by Barnes 2011).

the "genetic algorithm" technique (Holland 1975). This method adopts an evolutionary search strategy combined with an objective "goodness-of-fit" criterion such that the best-fitting parameters ("genes") out of a given number of models ("population") are mixed and passed on to the next generation of models. To avoid local maxima, spontaneous "mutations" or deliberate breeding with less-fit population members can be included. By this, large parameter searches can be carried out automatically that converge towards the best matching model. However, in the case of binary galaxy interactions, these algorithms often rely on simple restricted N-body codes, showing the known model limitations already discussed (Wahde 1998; Theis 1999; Theis & Kohle 2001). In particular, for a major merger such as the Antennae galaxies, it is difficult to reliably follow the orbital decay over the full merger timescale (Petsch & Theis 2011). Another, equally severe difficulty lies in finding robust criteria for the "goodness-of-fit". Therefore, we decided to rely on subjective comparison of the simulated properties to the observations, exploiting the - actually quite advanced - pattern recognition ability of the human brain (Neisser & Weene 1960; Fischler & Firschein 1987).

Another approach, aiming in the same direction, has recently been provided by the "Identikit 2" method (Barnes 2011), based on the following idea. Assuming that the tidal features of interacting galaxies mainly develop ballistically, their dynamical evolution can be considered to be governed (at least approximately) by the collisionless

Boltzmann equation. This implies that the dynamics are fully reversible at any given instant of time, with the initial geometry of the encounter still imprinted in the actual dynamical state of the tidal tails. This is used in "Identikit 2" to infer the initial spins of the progenitor disks directly from the observational data by requiring that various regions along a tidal tail have to stem from the same disk with *one* unique spin vector. While searching for the best-matching disk spin parameters, a numerical measure for the "goodness-of-fit" is intrinsically provided by the algorithm, allowing, in principle, for an automated search of the parameter space. We refer the reader to Barnes (2011) for further details and first tests of this new method.

4.3 Converging to the Best-matching Model

Within the framework of this Thesis, we want to add to the theoretical knowledge about the Antennae galaxies, and on merging galaxies in general. For that it is crucial that we recover a theoretical model which, on the one hand, is consistent with predictions from current CDM cosmologies, and, on the other hand, is largely constrained by the tremendous amount of high-quality data on the Antennae at our disposal. However, in practice, the observations alone do not suffice to uniquely describe the physical model. Hence, one needs to complement the parameters motivated by the observations with two additional sets of parameters. First, in order to narrow down the parameter space, we choose a number of (mostly numerical) parameters that are known to give reliable results from the literature, and, second, there is a set of all remaining unknown parameters one needs to survey. These are the three basic parameter groups we will discuss in turn in this Section.

Before commencing our studies, we defined three properties of the Antennae galaxies that we wanted to match as closely as possible in order to call our model the "best match". These were the global morphology and kinematics of the system, provided by the excellent HI data by Hibbard et al. (2001), along with a well-defined high surface density overlap region between the two galactic nuclei, featuring the puzzling extraordinary burst of off-center star formation (e.g. Klaas et al. 2010). In the following, we describe in detail how we converged towards the final fiducial model for the Antennae galaxies, as defined by the criteria given above. However, we will restrict ourselves to discussing the best-match parameters, and present, for later reference, all properties derived from the observations of the Antennae in Table 4.1 and compare them to the values adopted in our fiducial model. In addition, we give a summary of the most relevant model parameters and their probed range in Table 4.2. Finally, we defer the discussion on our constraint of the star formation algorithm to Chapter 5.

4.3.1 Constrained Parameters

In this Section, we discuss the set of model parameters which have constraints from observational estimates and theoretical predictions from the literature. However, in addition to the observational input, we varied most of the parameters obtained in this way within reasonable bounds to check the robustness of the models to these parameters. Ultimately, we chose the best-fit parameters according to the most promising results obtained in the simulations, which, however are generally close to the observational estimates (see below).

A first observational constraint on the simulations is given by the total observed mass in baryons in the galaxies. The total gas mass in the Antennae is measured as $M_{\rm gas} \sim M_{\rm HI} + M_{\rm H_2} \sim 2 \times 10^{10}\,{\rm M}_\odot$ (Gordon et al. 2001; Gao et al. 2001). We adopt a total initial gas mass of $M_{\rm gas} \sim 1.66 \times 10^{10}\,{\rm M}_\odot$ for our fiducial model, which corresponds to a disk gas fraction of $f_{\rm g} = M_{\rm gas}/M_{\rm disk} = 20\%$ in each disk. This is consistent with typical gas fractions relative to the stellar masses in local spirals ranging between $10\% - 30\%$ for Sa - Sc galaxies (McGaugh & de Blok 1997). Furthermore, we estimate the stellar content from the total B-band luminosity $L_{\rm B} = 2.9 \times 10^{10}{\rm L}_\odot$ (de Vaucouleurs et al. 1991) in the Antennae, assuming a range of (constant) mass-to-light ratios $\Upsilon_{\rm B} \in [0.5, 3]$ (Bell & de Jong 2001). The resulting estimated stellar masses then lie between $M_{\rm stellar} = 1.5 \times 10^{10}\,{\rm M}_\odot$ and $M_{\rm stellar} = 8.7 \times 10^{10}\,{\rm M}_\odot$, which is a little below our adopted value of $M_{\rm stellar} \sim 9.4 \times 10^{10}\,{\rm M}_\odot$. In addition, a recent "halo occupation model" (HOD; e.g. Figure 5 in Moster et al. 2010b), would tend to predict a lower total stellar mass in the Antennae than what we adopted, with $M_{\rm stellar} \sim 3.6 \times 10^{10}\,{\rm M}_\odot$, given our adopted total halo mass. However, owing to the large scatter in the HOD, our adopted value is marginally consistent with, while at the upper end of their predictions (see dotted points in Figure 6, Moster et al. 2010b).

We can put another, independent constraint on the total baryonic mass via the "Baryonic Tully-Fisher" (BTF) relation, using the nearly-constant rotational velocities observed in local spirals as a simple proxy for the total baryonic mass (McGaugh 2005),

$$M_{\rm bary} = 50\, V_{\rm rot}^4\,{\rm M}_\odot. \tag{4.2}$$

Using, e.g. the maximum rotational velocities of our fiducial disk galaxy models, $v_{\rm rot,4038}^{\rm max} = 189\,{\rm km\,s^{-1}}$ and $v_{\rm rot,4039}^{\rm max} = 198\,{\rm km\,s^{-1}}$ (see also Table 5.1), respectively, we obtain an upper limit for the total baryonic mass of $M_{\rm bary} = 1.4 \times 10^{11}\,{\rm M}_\odot$, which is quite close to our fiducial value of $M_{\rm bary} \sim 1.1 \times 10^{11}\,{\rm M}_\odot$. Hence we conclude that the stellar masses of our progenitor galaxies are at the upper end (or not dramatically above) what would be expected from observations and theoretical predictions.

We model our fiducial progenitor galaxies as typical early-type spirals of Sa/Sb−type with a stellar bulge-to-disk ratio $B/D \sim 0.4$ (Kent 1985; Binney & Merrifield 1998). This corresponds fairly well to suggestions by de Vaucouleurs et al. (1991) who

Table 4.1: Observational and derived properties of NGC 4038/39.

Property	**Value** (NGC 4038 / 4039)	**Best-fit Value**	**Notes/References**
Position (J2000)	R.A. $= 12^h01^m53.3^s$	$12^h01^m53.8^s$	de Vaucouleurs et al. 1991
	Decl. $= -18°52'37''$	$-18°52'50''$	
Distance D	22 ± 3 Mpc	30.8 Mpc	Schweizer et al. 2008
	13.3 ± 1.0 Mpc		Saviane et al. 2008
System Velocity	$1642 \pm 10\,\mathrm{km\,s^{-1}}$	$1630\,\mathrm{km\,s^{-1}}$	Firth et al. 2006
Galaxy Type	SB(s)m(pec) / SA(s)m(pec)	Sa/b (B/D = 0.4)	de Vaucouleurs et al. 1991
L_B	$2.9 \times 10^{10}\mathrm{L}_\odot$	—	de Vaucouleurs et al. 1991; Hibbard et al. 2001
L_IR	$7 \times 10^{10}\,\mathrm{L}_\odot$	—	Sanders et al. 2003
$L_\mathrm{X}^{0.1-10\,\mathrm{keV}}$	$2.3 \times 10^{41}\,\mathrm{erg\,s^{-1}}$	—	Fabbiano et al. 2001
M_HI	$\sim 5 \times 10^9\,\mathrm{M}_\odot$	—	Gordon et al. 2001; Hibbard et al. 2001
M_{H_2}	$1.5 \times 10^{10}\,\mathrm{M}_\odot$	—	Gao et al. 2001
M_dust	$3 \times 10^8\,\mathrm{M}_\odot$	—	Klaas et al. 2010
$M_\mathrm{X-ray}$	$4 \times 10^8\,\mathrm{M}_\odot$	—	Metz et al. 2004
SFR	$22.2\,\mathrm{M}_\odot\,\mathrm{yr}^{-1}$	$14.3\,\mathrm{M}_\odot\,\mathrm{yr}^{-1}$	Klaas et al. 2010
Derived Quantities			
Total Gas Mass	$\sim 2 \times 10^{10}\,\mathrm{M}_\odot$	$1.66 \times 10^{10}\,\mathrm{M}_\odot$	—
Total Stellar Mass	$1.5 - 8.7 \times 10^{10}\,\mathrm{M}_\odot$	$9.38 \times 10^{10}\,\mathrm{M}_\odot$	using $L_\mathrm{B} = 2.9 \times 10^{10}\mathrm{L}_\odot$ and $\Upsilon_\mathrm{B} = 0.5 - 3$ (Bell & de Jong 2001)
	$3.6 \times 10^{10}\,\mathrm{M}_\odot$		(Moster et al. 2010b, Figure 6)
Total Baryonic Mass	$1.4 \times 10^{11}\,\mathrm{M}_\odot$	$1.1 \times 10^{11}\,\mathrm{M}_\odot$	using the baryonic Tully-Fisher relation (McGaugh 2005)

lists NGC 4038 and NGC 4039 as SB(s)m(pec)- and SA(s)m(pec)-types. Based on this, Kassin et al. (2003) suggest that "NGC 4038 was probably a gas-rich Sb/Sc galaxy before the encounter, while NGC 4039 was probably a relatively gas-poor Sa".

The above choices result in a baryonic mass fraction of $f_{\rm bary} \equiv M_{\rm bary}/M_{\rm tot} = 0.10$ in the fiducial model. While still rather high, this falls well below the value of the cosmic baryonic fraction, $f^0_{\rm bary} \equiv \Omega_{\rm bary}/\Omega_{\rm matter} = 0.167$ (Komatsu et al. 2011), which poses a significant improvement over previous Antennae models that have typically adopted baryonic mass fractions exceeding the cosmic limit. For example, Barnes (1988) and Renaud et al. (2008) adopt $f_{\rm bary} = 0.2$ and $f_{\rm bary} \sim 0.29$ in their simulations in the pursuit to produce long tidal tails.

As we can see, there is a large number of model parameters on which we can put constrains from observations and theoretical predictions. These include the total stellar mass ($M_{\rm stellar}$), the total gas mass ($M_{\rm gas}$), the total disk and bulge mass fractions ($m_{\rm disk}$ and $m_{\rm bulge}$), and the disk gas mass fraction $f_{\rm g}$. Furthermore, we may put tentative upper limits on the total system mass using the BTF relation in Equation (4.2), where we take the virial velocities of the galaxies as a proxy for their total mass (see Equation (3.29)). The resulting baryonic fraction is marginally consistent with theoretical predictions (see Moster et al. 2010b). Finally, using the total corrected B-band magnitudes of NGC 4038 and NGC 4039 listed in de Vaucouleurs et al. (1991) as $B^0_{\rm T,4038}$ and $B^0_{\rm T,4039}$, respectively, we obtain a mass ratio of $M_{4038}/M_{4039} \sim 1.10$, if we assume a constant mass-to-light ratio in both galaxies. This gives re-assuring evidence that the Antennae are indeed a nearly 1:1 merger as expected for a system with large symmetric tails (Toomre & Toomre 1972). Following this we adopt a mass ratio of 1:1 in our modeling.

4.3.2 Fixed Parameters

A second group of parameters is deliberately kept unchanged in the simulations in order to narrow down the dimensionality in the probed parameter space. These parameters are mostly GADGET inputs, controlling the exact behavior of the code and the implemented additional physical modules. These have proven to give good results in previous numerical studies throughout the literature. Examples include, among others, the time step tolerance parameter η, the CFL parameter, or the tree opening criteria. These factors were already discussed in Chapter 3 so we don't comment further on them here. Another, smaller group that we have kept fixed throughout our studies are a number of parameters governing the internal structures of the galaxy models. These are listed in Table 4.2 and denoted with the label "fixed".

Table 4.2: Parameters used in the search for the best-fit to the Antennae galaxies.

Parameter Name	Variable Name	Probed Range	Best-fit Value (NGC 4038 / 4039)
Internal Parameters			
Total Mass	$M_{\rm tot}$	$(1.4-13)\times10^{11}\,{\rm M}_\odot$	$5.5\times10^{11}\,{\rm M}_\odot$
Concentration	c	$5-30$	15
Halo spin parameter	λ	$0.03-0.13$	0.10 / 0.07
Disk mass fraction	$m_{\rm disk}$	$0.02-0.17$	0.075
Bulge mass fraction	$m_{\rm bulge}$	$0.006-0.06$	0.025
Disk spin fraction	$j_{\rm disk}$	fixed	$m_{\rm disk}$
Disk gas fraction	$f_{\rm g}$	$0.1-0.4$	0.2
Vertical disk scale height	z_0	fixed	$0.2\cdot r_{\rm disk}$
Bulge scale length	$r_{\rm bulge}$	fixed	$0.2\cdot r_{\rm disk}$
Flat HI disk mass fraction	$f_{\rm g}^{\rm flat}$	$0-1$	0
HI disk cut-off radius	$r_{\rm cut}$	fixed	$6\cdot r_{\rm disk}$
Disk radial dispersion	$\sigma_{\rm r}$	$(1-2)\cdot\sigma_{\rm z}$	$\sigma_{\rm z}$
Factor for softened EOS	$q_{\rm EQS}$	$0.01-1$	0.01
Initial two-body orbit			
Mass ratio	μ	$0.9-1$	1
Initial separation	$r_{\rm sep}$	$1-2\times r_{200}$	$r_{200}=168\,{\rm kpc}$
Pericentric distance	$r_{\rm p}$	$\sim$ few$\times$ $0.5\,(r_{\rm d,1}+r_{\rm d,2})$	$r_{\rm disk,4038}+r_{\rm disk,4039}$ $=10.4\,{\rm kpc}$
Ellipticity	e	$0.9-1$	0.94
Disk orientation			
Inclination	i	free	60°
Argument of pericenter	ω	free	30° / 60°
Merger analysis			
Time of best match	$t_{\rm BM}$	free (after 1st periapse)	1.247 Gyr
Viewing angles	(θ,ψ,ϕ)	free	$(93, 69, 253.5)$
Plane-of-the-sky origin	$[X_C, Y_C]$	free	R.A. $=12^h01^m53.8^s$ Decl. $=-18^\circ52'50''$
Systemic velocity	$v_{\rm sys}$	free	$1630\,{\rm km\,s^{-1}}$
Length scale factor	$\mathcal{L}$	free	1.4
Velocity scale factor	$\mathcal{V}$	free	1

4.3.3 The Parameter Survey

Leaving aside all parameters that are either observationally constrained or kept fixed beforehand, we carried out a detailed parameter survey for the remaining fifteen parameters.

Concerning the internal structural properties, there are only three parameters left to determine. The halo concentration c and spin parameter λ (Section 3.3), as well as the parameter for the softened equation of state $q_{\rm EQS}$ (Section 3.1.3). While fixing the latter is deferred to Chapter 5, the values of c and λ are chosen such as to be consistent with the statistics found in ΛCDM cosmological simulations (e.g. Bullock et al. 2001b,a; Duffy et al. 2008; Muñoz-Cuartas et al. 2011). On the other hand, trying to reproduce the large relative sizes of the arms with respect to the main galaxies of the Antennae we are necessarily biased towards galaxy models with the potential to produce long tidal tails. The latter is primarily determined by the relative size of disk and halo (Springel & White 1999; Section 2.3) which implies that we tend to choose galaxy models with rather large spin parameters (see Table 4.2). We started with models discussed in the literature (see, e.g., Barnes 1988; Mihos et al. 1993), guessing new improved initial conditions after each run. Our final model was originally motivated by Model F in Springel & White (1999), which shows the largest tidal response in their models with c = 15. In order to meet the specific conditions in the Antennae, however, we lower the total mass, include a bulge, and account for the observed asymmetric tails by adopting different halo spins in the two galaxies, $\lambda^{4038} = 0.10$ and $\lambda^{4039} = 0.07$.

With this, all parameters governing the internal galaxy structure are fixed. Now we focus on the large-scale structure and kinematics of the tidal tails. Since these evolve basically ballistically after the first close encounter they still have imprinted the memory of their initial orientations. Thus, one of the most important parameters to be chosen before running the simulations are the orientations of the disks, specified by the inclination i and the pericentric argument ω, as well as the pericenter distance $r_{\rm p}$. Choosing the right combination for these parameters is crucial to obtain a promising model. This is highlighted in Figures 4.3 and 4.4 where we show a small parameter survey in i and ω centered around our best-matching parameters (middle panels) in the plane-of-the sky projection of the simulation data[2]. These figures illustrate the narrow parameter range in the disk orientations that may lead to a promising match. For instance, the match of the morphology in the plane-of-the-sky may alter substantially due to slight changes in the disk orientations of the order of only ±20°. In particular, while it seems that the inclinations for both NGC 4038 and NGC 4039 are very well constrained, the situation for the pericenter arguments seems to be slightly more ambiguous. For example, from Figure 4.4 it appears that a slightly lowered ω_{4038} (by

[2]Note that here and in the further analysis we will often refer to the rotated 3D "position-velocity" (PV) subspace of the simulation data, consisting of the plane-of-the-sky with coordinates x′, y′ and the line-of-sight velocity $v_{\rm los}$, when comparing to observations.

$\sim 10°$) yields an equally good fit, especially resulting in a good match of the marked "kink" at the tip of the southern galaxy, where the tail turns back towards the observer. On the other hand, we decided to adopt ω_{4038}, which shows, in addition to a well-defined "kink", the characteristic bifurcated HI structure in the southern tail as observed by Hibbard et al. (2001). Note that the corresponding changes to the other projections of the PV cube (not shown here),including the line-of-sight velocity, e.g. $x' - v_{\rm los}$ and $v_{\rm los} - y'$, are equally severe. This demonstrates the difficulty of simultaneously matching the kinematics in addition to a good morphological "look-alike" of the system.

Another parameter of prime importance to find a good match is the pericenter distance $r_{\rm p}$. For a given ellipticity e and total mass $M_1 + M_2$, it defines the total angular momentum of the Keplerian two-body orbit. In a test suite, where they try to reproduce a simulated mock catalog of galaxy mergers, Barnes & Hibbard (2009) find a degeneracy when fitting simultaneously for the pericenter distance $r_{\rm p}$, the time of best match $t_{\rm BM}$, and the scale factor $\mathcal{L}$. The reason for this is quite simple. First, wider passages merge more slowly, such that an over-(under-)estimate for the time of best match $t_{\rm BM}$ can be counteracted by adopting larger(smaller) pericenter distances $r_{\rm p}$. Similarly, since at later times in the interaction the tips of the tidal tails are unbound and move at asymptotically constant velocity (Toomre & Toomre 1972) the tail sizes grow approximately proportional to the time elapsed since they were launched (Schweizer 1978), i.e. since their last pericenter passage. Hence, a wrong time estimate results in a proportional error in the tail sizes. The latter, however, may be re-scaled to the correct physical size using the appropriate scale factor $\mathcal{L}$.

A similar situation holds in the Antennae, however, after the second pericenter, as we will see below. Owing to the characteristic morphology of their inner regions, the time of best match and pericenter distance can be constrained within a narrow range in this special case. To demonstrate this we show the stellar surface densities for our best-match model at three instants of time in Figure 4.5, the time of best match $t = t_{\rm BM}$ (middle column), $t = t_{\rm BM} - 30\,{\rm Myr}$ (left column), and $t = t_{\rm BM} + 30\,{\rm Myr}$ (right column). The large-scale morphology (lower panels) is very similar for all three times with only very subtle differences in the length of the tidal tails and decreasing central surface densities. This means that the time of best match would not be well-constrained by the large-scale morphology alone, since, in principle, we could account for a different size with a modified length scale as discussed above. However, in our simulation a region similar to the overlap in the Antennae forms only during a very short period of time ($\Delta t \sim 40\,{\rm Myr}$) between the second close encounter and the final merger (upper panels of Figure 4.5), providing a "good" match to the real system for only $\sim 20\,{\rm Myr}$. Shortly after the second encounter (upper left panel), the overlap region develops in a way similar to the "tidal bridges" generally associated with the first close encounter in low-inclination unequal-mass encounters (Toomre & Toomre 1972), incited by mutual tidal forces, and that of "splash" bridges, forming from the colliding gas of interpene-

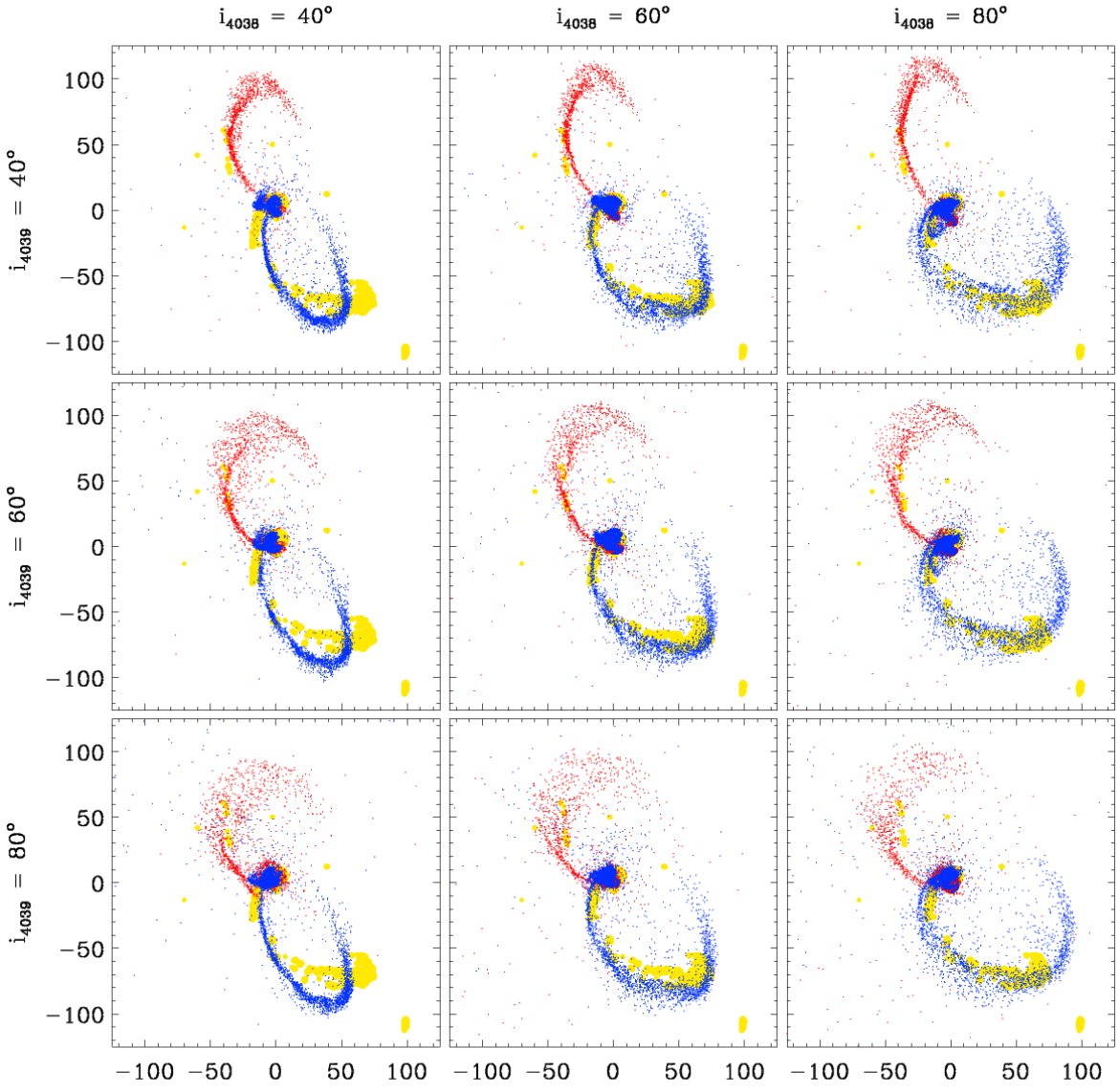

Figure 4.3: Inclination parameter survey spanning $i_{\rm j} = i_{\rm BM,j} \pm 20°$ (j = 4038, 4039, $i_{\rm BM,4038} = i_{\rm BM,4039} = 60°$).

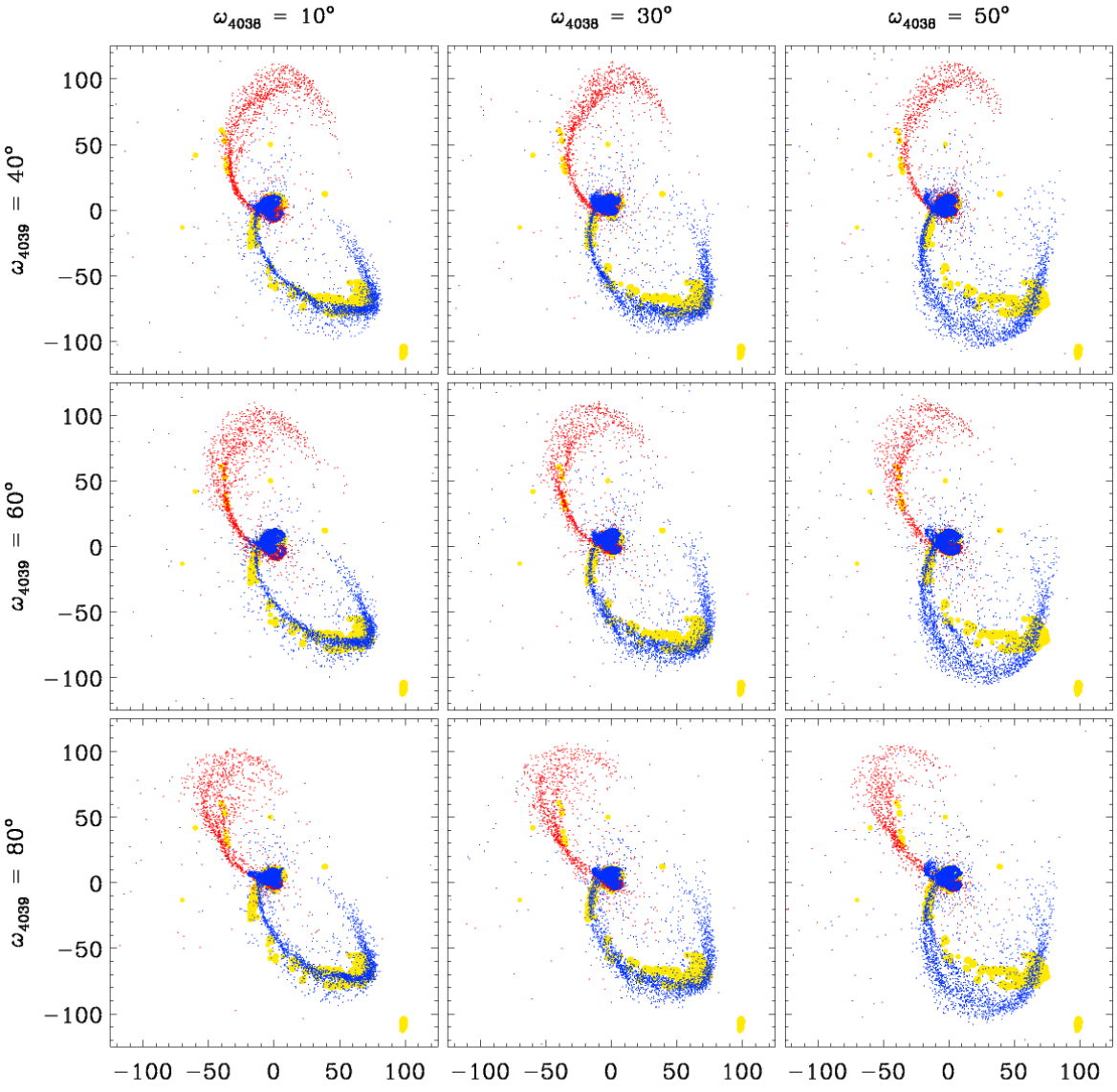

Figure 4.4: Pericenter argument parameter survey spanning $\omega_{\rm j} = \omega_{\rm BM,j} \pm 20^\circ$ (j = 4038, 4039, $\omega_{\rm BM,4038} = 30^\circ$, $\omega_{\rm BM,4039} = 60^\circ$).

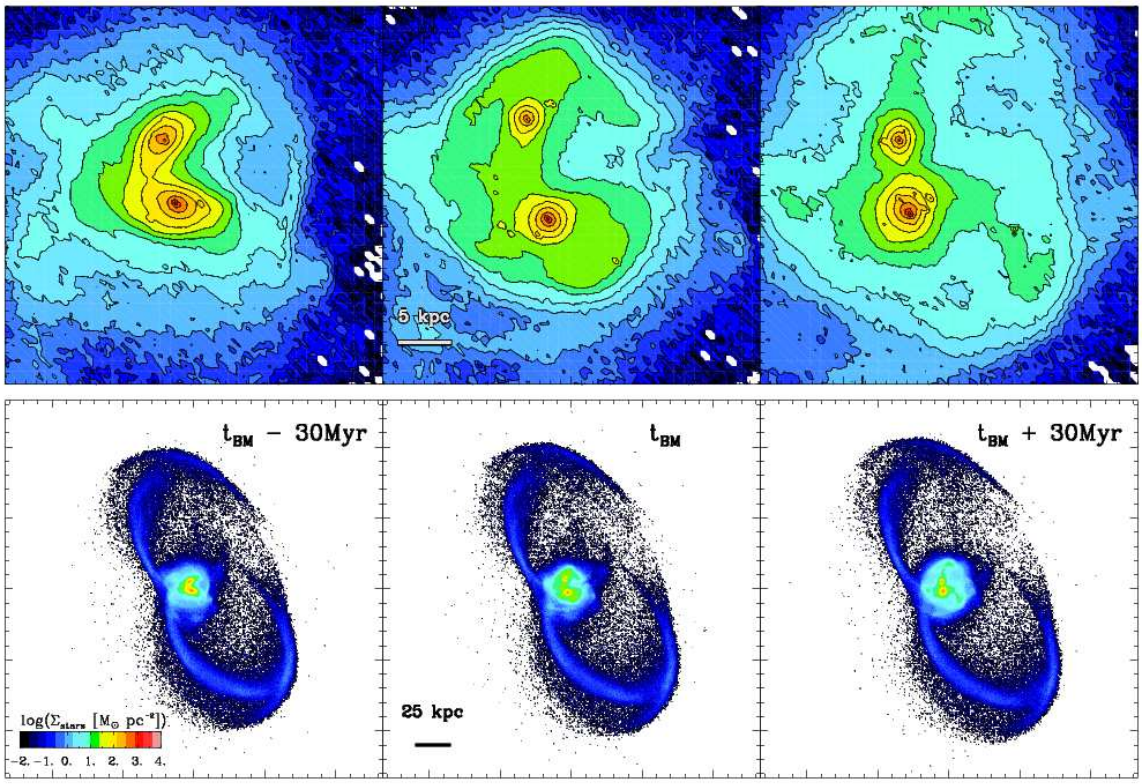

Figure 4.5: Evolution of stellar surface densities in the fiducial model at three instants of time after the second close encounter, the time of best match $t = t_{\rm BM}$ *(middle panels)*, and $t_{\rm BM} - 30\,{\rm Myr}$ *(left panels)* and $t_{\rm BM} + 30\,{\rm Myr}$ *(right panels)*. The time span to recover a high-surface density region similar to the overlap region in the Antennae is very short, $\Delta t \sim 20\,{\rm Myr}$.

trating disks (Struck 1997). However, at that time, the nuclei are still quite close and have not yet fully developed the characteristic "cleft" between the two main galaxies as observed in the Antennae (see Figures 2.1 and 2.4). At $t_{\rm BM} + 30\,{\rm Myr}$ (upper right panel) the galaxies have turned around and are about to fall back again for the final merger. The overlap surface brightness has already faded again. As a consequence, we find that the pericenter distance is also set within small bounds with the additional constraints that, first, the two disks separate wide enough after the second encounter to produce the familiar "cleft" between the galaxies, and, second, a too large pericenter distance leads to long merger timescales resulting in distorted tail morphologies and tail sizes inconsistent with distance estimates for the Antennae for our chosen galaxy models. These findings give the first indications that we observe the Antennae in a very special instant of their evolution! We will further lay out this finding in Chapter 5.

The remaining parameters are all chosen during the analysis of the simulation after each run. For this purpose we have developed a little interactive program that allows to simultaneously manipulate the viewing angles (θ, ψ, ϕ), the co-ordinate origins in the

plane of the sky $[X_C, Y_C]$, the systemic velocity $v_{\rm sys}$, and the scale factors $\mathcal{L}$ and $\mathcal{V}$ for all snapshots. With this tool at hand, determining these parameters is computationally inexpensive, while it still poses the most time-consuming task for the experimenter and the quality of the outcome depends mostly on his/her experience and patience.

The exact choice of the analysis parameters sensitively determines the final appearance of the simulation data in the PV subspace. A close-up of our particular choice is shown in the upper middle panels of Figure 4.6. We find that the vantage point, while chosen freely, lies actually close to the orbital plane, almost "edge-on" along the negative x-axis (see right panels). This is similar to the results noted in earlier studies (Toomre & Toomre 1972; Barnes 1988). The stellar surface density is highest inside the inner ∼few kpc of the two galactic nuclei, in contrast to the gas phase which also shows an enhanced surface density region peaking in the overlap region between the two nuclei (see 5.3 in Chapter 5). Independent of the viewing direction, this is not due to a chance projection of the two disks along the line-of-sight, but due to a real physical proximity of the two nuclei as evidenced by the projection inside the orbital

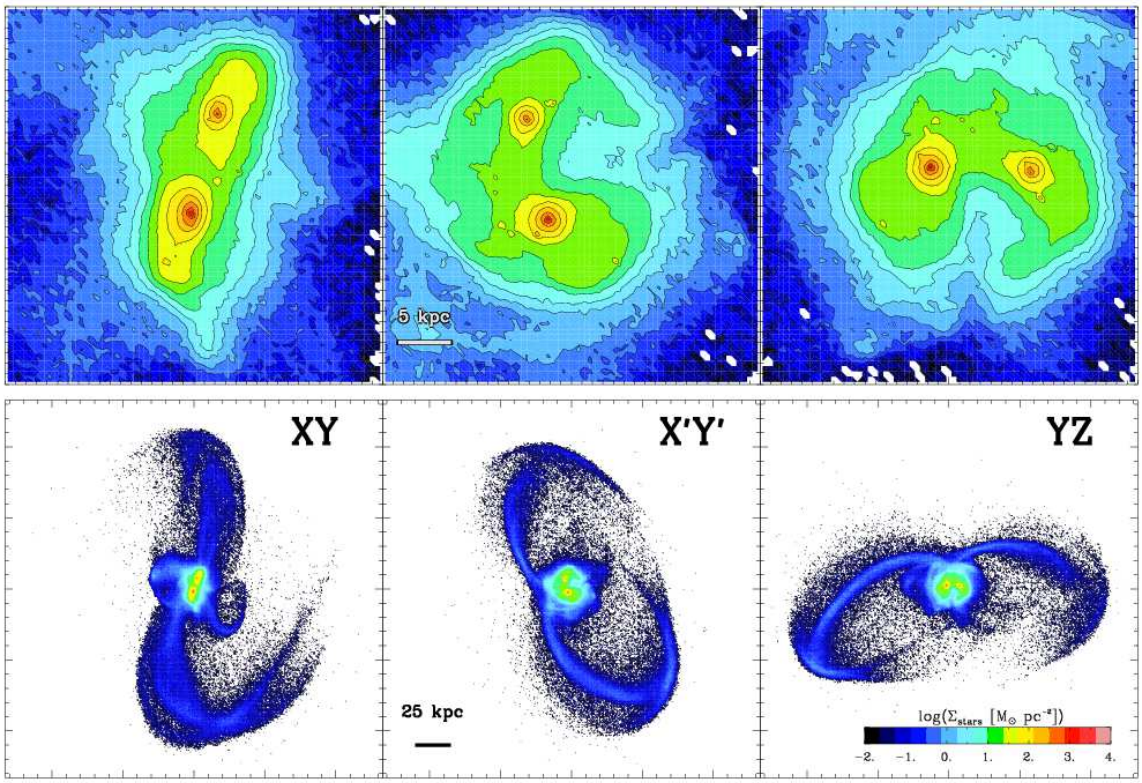

Figure 4.6: Different views of the central *(upper panels)* and the large-scale *(lower panels)* stellar surface densities for the fiducial Antennae simulation. The plane-of-the-sky (X'Y') is shown in the middle panels along with additional views "face-on" (*left column*, XY) and "edge-on" (*right column*, YZ) with respect to the orbital plane.

plane (upper left panel). While the southern tail has a high surface density at its tip due to the super-imposed projection of its bifurcated arm, the northern tail is more diffuse and shows a slight "break" in the surface density profile at distances $\gtrsim 80\,\mathrm{kpc}$ from the main bodies. This may partly explain the unequal length of the real tails in the Antennae (see also discussion of Figure 5.1 in Chapter 5).

Finally, this completes the parameter survey and constrains all the parameters needed to describe our fiducial Antennae model (deferring the discussion of our choice for q_{EQS} to the next Chapter). The time evolution of the stellar and gas surface densities in the plane-of-the-sky for the fiducial simulation is shown in Figure 4.7. After the beginning of the simulation ($t = 0.40\,\mathrm{Gyr}$), the galaxies evolve largely undisturbed on their initial two-body orbit. Following the first pericenter, the galaxies are tidally distorted and develop tidal tails ($t = 0.80\,\mathrm{Gyr}$). Due to a nearly head-on collision of the extended dark matter halos, orbital energy decreases efficiently because of the effect of dynamical friction, leading to a turn-around on an almost radial orbit after the first encounter ($\sim 1.00\,\mathrm{Gyr}$). Following the second encounter, a high-density overlap region has formed at the time of best match, which we find at $t = 1.247\,\mathrm{Gyr}$. In the final merger at $t = 1.30\,\mathrm{Gyr}$, both disks are destroyed and form a spheroidal remnant ($t = 2.30\,\mathrm{Gyr}$, see Chapter 7). The gas component, sharing the same initial phase space with some fraction of its surrounding stellar material, evolves similar to the stellar component. However, due to shocks during the close passages some of the kinetic energy of the gas is converted into heat and is radiated away, leading to high local gas densities and associated star formation, as e.g seen in the overlap region after the second encounter. In addition, after the first encounter, tidal torques efficiently funnel gas to the centers of the galaxies where high densities and short cooling timescales trigger a nuclear starburst.

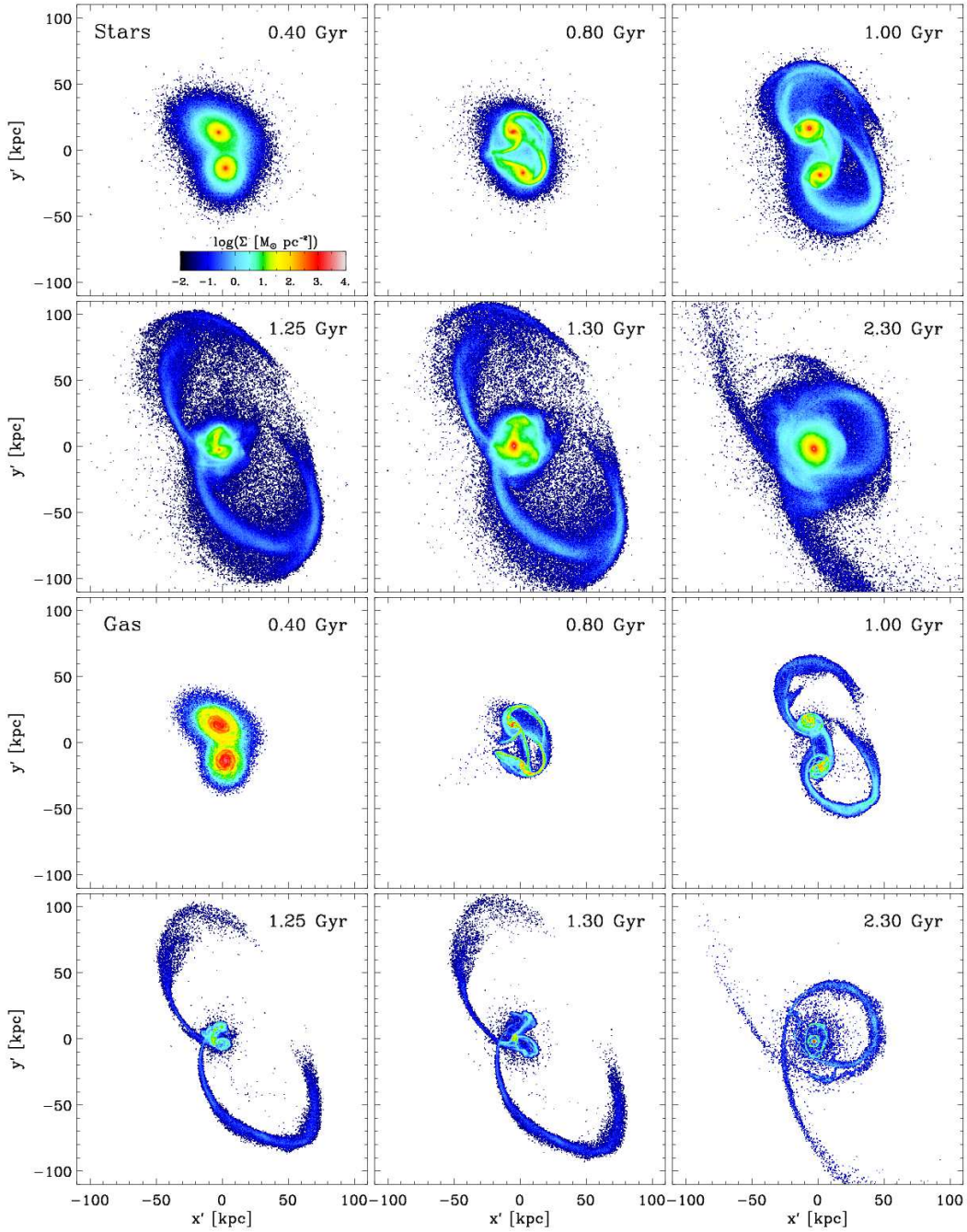

Figure 4.7: Time evolution of the stellar *(two upper rows)* and gas *(two lower rows)* surface densities in the fiducial Antennae simulation projected onto the plane-of-the-sky. The projected plane measures $125\,\mathrm{kpc}$ aside, corresponding to an assumed distance of $D = 30.8\,\mathrm{Mpc}$ to the Antennae. The time elapsed since the beginning of the simulations is indicated in the upper right corner of each panel.

Chapter 5

Star Formation in the Antennae Galaxies

In this Chapter, we present new high-resolution N-body/SPH simulations of an encounter of two gas-rich disk galaxies which closely matches the morphology and kinematics of the interacting Antennae galaxies (NGC 4038/39). The simulations include radiative cooling, star formation and feedback from supernovae of type II. The large-scale morphology and kinematics are determined by the internal structure and the orbit of the progenitor disks. The properties of the central region, in particular the starburst in the overlap region, only match the observations for a very short time interval ($\Delta t \approx 20$ Myr) after the second encounter. This indicates that the Antennae galaxies are in a special phase only about 40 Myr after the second encounter and 50 Myr before their final collision. This is the only phase in the simulations when a gas-rich overlap region between the nuclei is forming accompanied by enhanced star formation. The star formation rate as well as the recent star formation history in the central region agree well with observational estimates if we adopt a very weak parametrization for the stellar feedback, with a parameter for the softened effective equation of state $q_{\rm EQS} = 0.01$. For the first time this new model explains the distributed extra-nuclear star formation in the Antennae galaxies as a consequence of the recent second encounter. First synthetic maps in the FIR and from CO(1-0) emission confirm these conclusions. Both show a strikingly similar spatial distribution of the emission peaks in the observed and simulated maps, revealing the localized sites of on-going star formation in the overlap. The proposed model predicts that the Antennae are in a later merger stage than the Mice (NGC 4676) such that the Antennae would lose their first place in the classical Toomre sequence (Toomre 1977). Parts of this Chapter have been published in Karl et. al. 2010, ApJ, 715, L88.

Table 5.1: Model parameters of the best-fit merger configuration

Property	NGC 4038	NGC 4039
$M_{\rm vir}$ [a]	55.2	55.2
$M_{\rm disk,stellar}$	3.3	3.3
$M_{\rm disk,gas}$	0.8	0.8
$M_{\rm bulge}$	1.4	1.4
$r_{\rm disk}$ [b]	6.28	4.12
z_0	1.26	0.82
$r_{\rm bulge}$	1.26	0.82
c [c]	15	15
λ [d]	0.10	0.07
$v_{\rm rot}^{\rm maxe}$	189	198

[a] Mass in $10^{10}\,{\rm M}_\odot$
[b] Disk and bulge lengths ($r_{\rm disk}$, $r_{\rm bulge}$) and disk scale height (z_0) are given in kpc
[c] Halo concentration parameter
[d] Halo spin parameter
[e] Maximum rotational velocity in $\rm km\,s^{-1}$

5.1 The Antennae as a Laboratory to Study Merger-induced Star Formation

The Antennae galaxies (NGC 4038/39) are the nearest and best-studied example of an on-going major merger of two gas-rich spiral galaxies (Chapter 2). The system sports a beautiful pair of elongated tidal tails extending to a projected size of $\sim 20'$ (i.e. 106 kpc at an assumed distance of 22 Mpc) together with two clearly visible, still distinct galactic disks. The latter has been assumed to be an indication of an early merger state, putting the system in the first place of the Toomre (1977) merger sequence of 11 prototypical mergers (see Section 2.3). Due to their proximity and the ample number of high-quality observations covering the spectrum from the radio to the X-ray (e.g. Neff & Ulvestad 2000; Wang et al. 2004b; Whitmore et al. 1999; Hibbard et al. 2005; Zezas et al. 2006; Section 2.2) the Antennae provide an ideal laboratory for understanding the physics of merger-induced starbursts through comparison with high-resolution simulations.

At the center of the Antennae galaxies, HST imaging has revealed a large number of bright young star clusters ($\gtrsim 1000$), which plausibly have formed in several bursts of star formation induced by the interaction (Whitmore et al. 1999). The spatial distribution and the ages of these clusters are correlated: the youngest clusters are found in the overlap region ($\tau < 5\,{\rm Myr}$), while a young starburst is generally located in the overlap and a ring-like configuration in the disk of NGC 4038 ($\tau \lesssim 30\,{\rm Myr}$). An

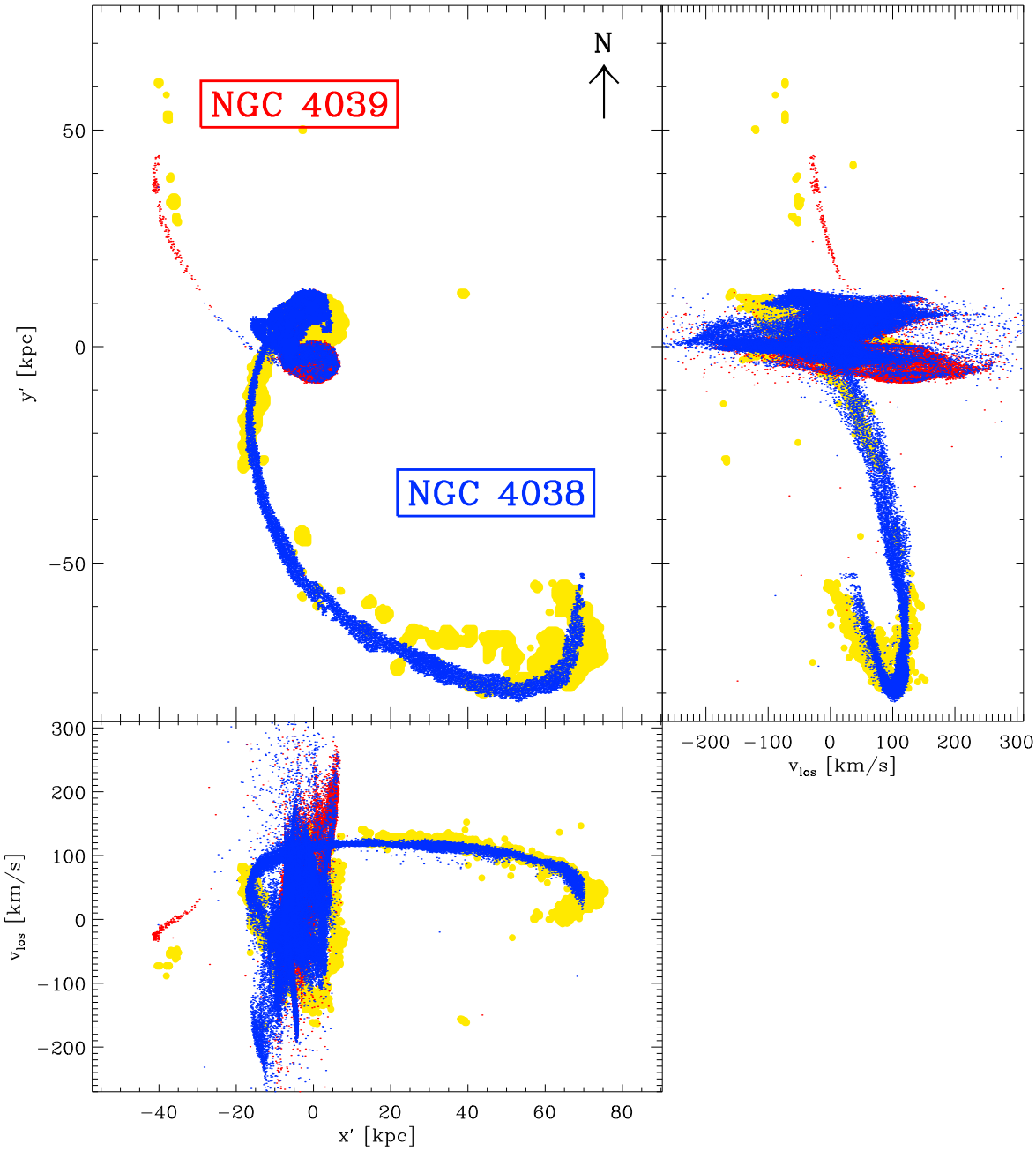

Figure 5.1: Simulated gas properties projected on top of HI kinematic data by Hibbard et al. (2001) at the time of best match. Simulated gas particles are displayed in blue (NGC 4038) and red (NGC 4039). Yellow points represent the observational data. *Upper left panel:* Projected positions in the plane-of-the-sky (x′-y′ plane). *Upper right and lower left panel:* Declination (y′) and Right Ascension (x′) against line-of-sight velocity. Similarly to the observations, we apply a column density threshold of $N_{\rm gas} = 10^{20}\,{\rm cm}^{-2}$ to the simulated gas distribution.

intermediate-age population ($\tau = 500 - 600\,\mathrm{Myr}$) is distributed throughout the disk of NGC 4038 (Whitmore et al. 1999; Zhang et al. 2001).

Of particular interest is the spectacular nature of an extra-nuclear starburst observed in the dusty overlap region between the merging galactic disks (Mirabel et al. 1998; Wang et al. 2004b). The Antennae seem to be one out of only few interacting systems where an off-center starburst is outshining the galactic nuclei in the mid-infrared (see Section 2.2). To date, this prominent feature has not been reproduced in any simulation of the Antennae system (see Section 2.3). In this Chapter, we report on the first high-resolution merger simulations of NGC 4038/39, using cosmologically motivated progenitor disks galaxy models (see Section 4.3) that can explain the formation of the extra-nuclear starburst in a high surface density region between the two galaxy centers. We present the match to the large-scale morphology and the line-of-sight kinematics of the Antennae (Section 5.3), and study the on-going star formation in the Antennae (Section 5.4). Furthermore, we compare with observations (Section 5.5) and shortly recapitulate relevant details of our fiducial high-resolution simulation (Section 5.2). We discuss our results in Section 5.6.

5.2 Simulations

The simulations presented here are the best-fitting models of a larger parameter study (discussed in Chapter 4) and were performed using GADGET 3 (Springel 2005). We include primordial radiative cooling and a local extra-galactic UV background. Star formation and associated feedback of supernovae type II are modeled following the sub-grid multi-phase prescription of Springel & Hernquist (2003), but excluding supernovae-driven galactic winds (see Chapter 3). We employ a fiducial set of parameters governing the multi-phase feedback model resulting in a SFR of $\sim 1\,\mathrm{M}_\odot\,\mathrm{yr}^{-1}$ for a Milky Way-type galaxy (Section 3.1.3), adopting a softened equation of state with three different values $q_{\mathrm{EQS}} = 0.01$, 0.5, and 1.0. We discuss the differences between these three simulations in Section 5.4 below.

In all three simulations, each progenitor galaxy is set up in equilibrium with a total virial mass $M_{\mathrm{vir}} = 5.52 \times 10^{11}\,\mathrm{M}_\odot$, according to the method detailed in Section 3.3. In each galaxy, the exponential stellar disk comprises a constant disk mass fraction $m_{\mathrm{d}} = 0.075$ of the total virial mass. The stellar bulge has a total mass fraction of $m_{\mathrm{b}} = 0.025$, resulting in a bulge-to-disk ratio of $m_{\mathrm{b}}/m_{\mathrm{d}} = 1/3$. The gas mass fraction in the disk is $f_{\mathrm{g}} = 0.2$ with the rest of the disk mass remaining in stars. A summary of the most relevant model parameters is given in Table 5.1.

Each galaxy is realized with $N_{\mathrm{tot}} = 1.2 \times 10^6$ particles, consisting of a total of 400,000 halo particles, 200,000 bulge particles, 480,000 disk particles and 120,000 SPH

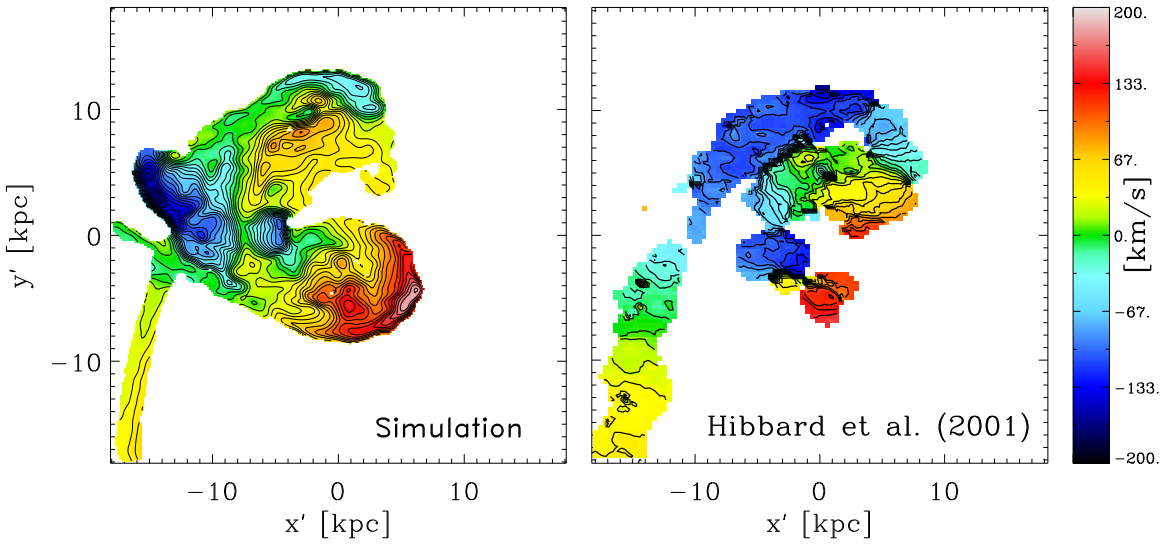

Figure 5.2: Line-of-sight velocity fields inside $\pm 18\,\mathrm{kpc}$ of the simulated and observed central disks. Isovelocity contours are drawn at $10\,\mathrm{km\,s^{-1}}$ intervals ranging from $-200\,\mathrm{km\,s^{-1}}$ to $200\,\mathrm{km\,s^{-1}}$. *Left:* density-weighted velocity map. *Right:* intensity-weighted HI velocity field of the high-resolution data cube. A column density threshold is applied as in Figure 5.1.

particles. In order to avoid spurious two-body effects we ensured that all baryonic particles have the same mass and only *one* stellar particle is spawned per SPH particle. This yields a total baryon fraction of $f_{\mathrm{bary}} = 10\%$ with particle masses for the baryonic components (bulge, disk, formed stars, and gas) of $m_{\mathrm{bary}} = 6.9 \times 10^4\,\mathrm{M}_\odot$ and $m_{\mathrm{DM}} = 1.2 \times 10^6\,\mathrm{M}_\odot$ for the dark matter particles.

The gravitational softening lengths are set to $\epsilon_{\mathrm{bary}} = 0.035\,\mathrm{kpc}$ for baryons, and $\epsilon_{\mathrm{DM}} = 0.15\,\mathrm{kpc}$ for dark matter particles, scaled according to $\epsilon_{\mathrm{DM}} = \epsilon_{\mathrm{bary}}\,(m_{\mathrm{DM}}/m_{\mathrm{bary}})^{1/2}$ (Dehnen 2001).

We adopt an initially nearly-parabolic, prograde orbit geometry (the orbital plane lies in the x-y plane) with a pericenter distance of $r_{\mathrm{p}} = r_{\mathrm{d,4038}} + r_{\mathrm{d,4039}} = 10.4\,\mathrm{kpc}$ and an initial separation of $r_{\mathrm{sep}} = r_{\mathrm{vir}} = 168\,\mathrm{kpc}$. For the orientation of the progenitor disks we found the best match to the Antennae system with inclinations $i_{4038} = 60°$, $i_{4039} = 60°$ and arguments of pericenter $\omega_{4038} = 30°$, $\omega_{4039} = 60°$ (see Table 4.2 for further details).

5.3 The Morphological and Kinematical Match

The morphologies and kinematics of the three simulations with varying q_{EQS} are very similar. In this Section, we will report only results from the simulation with $q_{\mathrm{EQS}} = 0.01$, which are representative for all three simulations.

Comparing to the HI position-velocity data by Hibbard et al. (2001), we determine the time when the simulation best matches the Antennae together with the viewing angles (θ,ψ,ϕ). Additionally, we apply a distance scale ($\mathcal{L}$) relative to a fiducial distance of 22 Mpc (Schweizer et al. 2008, see also Section 2.2) and assume a systemic helio-centric velocity of $1630\,\mathrm{km\,s^{-1}}$ to fit the data to the physical scales in the simulation. We find our best match to the observed large- and small-scale properties of the system with viewing angles of $(93, 69, 253.5)$ and $\mathcal{L} = 1.4$, yielding a distance of $D = 30.8\,\mathrm{Mpc}$ to the system, about 40% above the currently favored distance estimation of $22 \pm 5\,\mathrm{Mpc}$. The "best fit" ($t = 1.247\,\mathrm{Gyr}$ after beginning of the simulation) is reached only $\sim 45\,\mathrm{Myr}$ after the second encounter ($t = 1.20\,\mathrm{Gyr}$), and approximately $50\,\mathrm{Myr}$ before the final merging of the galaxy centers ($t = 1.30\,\mathrm{Gyr}$). From our larger parameter study we found this exact timing to be a mandatory requirement for reproducing the overlap starburst (see Section 4.3 and Figure 4.5). The first close passage of the two progenitor disk galaxies occurred $\sim 600\,\mathrm{Myr}$ ago, which is considerably longer ago than $\sim 200 - 400\,\mathrm{Myr}$ as suggested in earlier models (Barnes 1988; Mihos et al. 1993) and in much better agreement with observed 'intermediate-age' star clusters ($\sim 500 - 600\,\mathrm{Myr}$) (Whitmore et al. 1999, 2010; Kassin et al. 2003, see also Chapter 6).

In Figure 5.1, we show three large-scale projections of the PV cube of our simulated gas particles (NGC 4038: blue, NGC 4039: red) together with a direct comparison with HI observations (yellow) by Hibbard et al. (2001). The HI gas phase is used here as a tracer for the smooth underlying morphological and kinematical structure of the gas in the Antennae and we apply, similarly to the HI observations, a column density threshold of $N_{\mathrm{HI}} \leq 1 \times 10^{20}\,\mathrm{cm^{-2}}$ in the simulation. The top left panel displays the plane-of-the-sky projection, while in the top right and bottom left panels we show two orthogonal position-velocity profiles, Declination versus v_{los} (upper right) and v_{los} versus Right Ascension (lower left), respectively. The simulation matches the morphology and kinematics of the observed system very closely, especially for the southern arm, including the prominent kink in the velocities at the tip of the tidal arm (see Figure 5.1, upper right and lower left panels). Due to the different initial orientations of the progenitor disks, the gas distribution in the northern arm is more diffuse than in the southern arm. The assumed column density cut-off therefore results in the same characteristic stubby geometry as observed (upper left panel of Figure 5.1).

A close-up of the simulated and observed line-of-sight velocity fields in the central 18 kpc of NGC 4038/39 is shown in the left and right panels of Figure 5.2. Gas particles are binned on a SPH-kernel weighted 256^3 grid and summed up along the line-of-sight to produce a density-weighted velocity map (see Hibbard et al. 2001). The grid is smoothed with the observed beam profile and displayed using the same projected pixel sizes ($\Delta_{\mathrm{RA}} = 2.64''$ and $\Delta_{\mathrm{Decl}} = 2.5''$) as in Hibbard et al. (2001). We overlay isovelocity contours spaced by $10\,\mathrm{km\,s^{-1}}$ and apply the same column density threshold as in

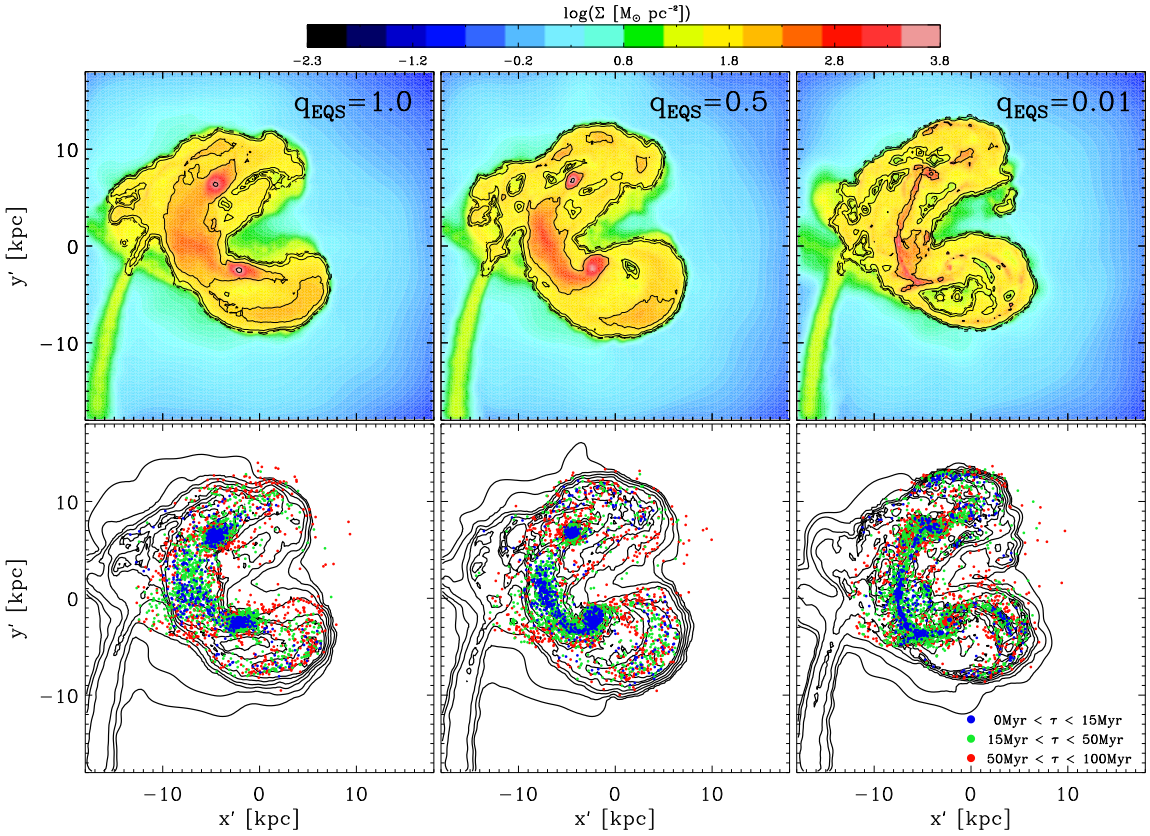

Figure 5.3: Projected gas surface density and star formation in the central $\pm 18\,\mathrm{kpc}$ of the simulated disks for three values of the parameter for the softened equation of state, $q_{\mathrm{EQS}} = 1.0$ (*left*), $q_{\mathrm{EQS}} = 0.5$ (*middle*), and $q_{\mathrm{EQS}} = 0.01$ (*right*). *Upper panels:* Projected gas surface density overlain with contours of the the star formation rate surface density. The contours correspond to levels of $\log(\Sigma_{\mathrm{SFR}} \,/\, \mathrm{M}_\odot\,\mathrm{yr}^{-1}\,\mathrm{kpc}^{-2}) = -6, -5, \ldots, -3, -2$, respectively. *Lower panels:* Gas surface density contours and stellar particles formed within the last $100\,\mathrm{Myr}$, color-coded by their age (see legend).

Figure 5.1. The simulation agrees well with the observed velocity field of the disk in NGC 4038. The northern part is approaching and the southern part is receding with a symmetric spread in the velocities. However, the observed velocity field (right panel) shows a larger spread in the line-of-sight velocities, ranging within about $\pm 150\,\mathrm{km\,s^{-1}}$, about a factor of two larger than in the simulation. Similarly, the simulated disk of NGC 4039 is approaching in the northern part and receding in the southern part very similar to the observations. In the simulation, we have significantly more gas in the overlap region and the southern disk than in the observed HI velocity field. This may be partly due to the fact that we do not distinguish between molecular, atomic, and ionized gas phases in our simulations, whereas most of the gas in the central regions of the Antennae seems to be in molecular form (Gao et al. 2001). We will investigate this further in Section 5.5 below. In addition, the specific distribution in HI may indicate that the two galaxies had quite different gas fractions even before the interaction.

5.4 The Recent Starburst

We want to study the merger-induced star formation in the Antennae. Especially interesting, of course, is the peculiar overlap starburst (Section 2.2). By direct comparison with the detailed multi-wavelength observations we can test and possibly constrain the star formation algorithm used in GADGET 2 & 3. In particular, we aim to put limits on the strength of the applied stellar feedback by choosing three (bracketing) cases of the parameter for the softened equation of state (see Section 3.1.3), namely the 'standard' full feedback model with $q_{\mathrm{EQS}} = 1.0$, an intermediate model with $q_{\mathrm{EQS}} = 0.5$, and a model with very weak feedback $q_{\mathrm{EQS}} = 0.01$. In the upper panels of Figure 5.3 we show a color-coded map of the total gas surface density Σ_{gas} in the central $\pm 18\,\mathrm{kpc}$ of the simulations, overlain with contours of the SFR surface density Σ_{SFR}. For all three parameters, the overall morphology is similar. The nuclei of the progenitor disks are still well distinct, but connected by a ridge of high density gas. In the case of strong feedback, a high-density overlap region has formed, but the highest densities are found in the galactic centers. In the simulations with less vigorous feedback, however, the high surface density regions tend to become more pronounced in the overlap (middle and right upper panels). As a consequence we also find an increasing number of low-density ("void") regions inside the disks for lower values of q_{EQS} due to the decreasing pressure support in the star-forming gas. The star formation contours directly support this picture. Lowering the strength of the stellar feedback leads to ever narrower, more localized regions of intense star formation activity. Note that spatially confined areas of similar extent are observed in the overlap region in the Antennae (e.g. Mirabel et al. 1998; Zhang et al. 2001; Wilson et al. 2000; Wang et al. 2004b; Zhang et al. 2010). In the lower panels of Figure 5.3, we show the corresponding contours in the gas surface density and overplot color-coded all stellar particles (with individual masses of $m_{\mathrm{star}} = 6.9 \times 10^4 M_\odot$) formed in the last $\tau < 15\,\mathrm{Myr}$ (blue), $15\,\mathrm{Myr} < \tau < 50\,\mathrm{Myr}$

Table 5.2: Relative star formation rates between the nuclei and the overlap region in three different simulations with $q_{\rm EQS} = 1.0$, $q_{\rm EQS} = 0.5$, and $q_{\rm EQS} = 0.01$.

Simulation	Region	Area	$N_\star/N_\star^{\rm tot}$	$N_\star(< 1\,{\rm Myr})$	SFR $[{\rm M_\odot\,yr^{-1}}]$
$q_{\rm EQS} = 1.0$	$\rm Nuc_{4038}$	$r = 1\,{\rm kpc}$ at $(-4.4, 6.3)$	10.6 %	25	1.71
	$\rm Nuc_{4039}$	$r = 1\,{\rm kpc}$ at $(-1.7, -2.7)$	32.1 %	53	4.08
	Overlap	$x \in [-10, -3.8]$, $y \in [-3, 5]$	9.6%	10	0.49
$q_{\rm EQS} = 0.5$	$\rm Nuc_{4038}$	$r = 1\,{\rm kpc}$ at $(-4.25, 6.9)$	15.4%	62	4.55
	$\rm Nuc_{4039}$	$r = 1\,{\rm kpc}$ at $(-2.3, -2.1)$	38.1%	40	2.85
	Overlap	$x \in [-9.5, -3.8]$, $y \in [-5., 6.]$	10.6%	27	0.76
$q_{\rm EQS} = 0.01$	$\rm Nuc_{4038}$	$r = 1\,{\rm kpc}$ at $(-4.4, 7.5)$	10.5%	8	0.49
	$\rm Nuc_{4039}$	$r = 1\,{\rm kpc}$ at $(-2.1, -3.1)$	28.5%	5	0.44
	Overlap	$x \in [-10.5, -3.2]$, $y \in [-5.5, 6.]$	15.4%	177	10.88

(green), and $50\,{\rm Myr} < \tau < 100\,{\rm Myr}$ (red). This period corresponds to the time span of the interaction-induced rise in the star formation activity during the recent second encounter. The youngest stars (blue) form predominantly in regions of currently high gas densities, i.e. in the centers, the overlap region, and in the arc-like features along the disks, very similar to observations of the youngest clusters in the Antennae (Whitmore et al. 1999, 2010; Wang et al. 2004b, see also Section 2.2). In particular, the star formation in the galaxy centers is much more pronounced in the simulation with $q_{\rm EQS} = 1.0$ (lower left panel), while the overlap starburst gains more and more in relative importance for $q_{\rm EQS} = 0.5$ and $q_{\rm EQS} = 0.01$ (see below). Furthermore, young stars ($\tau < 50\,{\rm Myr}$) tend to be more concentrated in the overlap region and well-defined arcs in the remnant spirals, while older stars ($50\,{\rm Myr} < 100\,{\rm Myr}$) are dispersed more evenly throughout the disks. A similar trend is observed in the Antennae (e.g. Zhang et al. 2001, Figure 2). This implies that the overlap starburst is a quite recent phenomenon, induced by the second encounter. Simulating the system further in time we find that the total duration of the off-center starburst is no longer than $\approx 20\,{\rm Myr}$ (cf. Figure 4.5).

Brandl et al. (2009) derived spatially resolved SFRs in the nuclei of NGC 4038 ($0.63\,{\rm M_\odot\,yr^{-1}}$) and NGC 4039 ($0.33\,{\rm M_\odot\,yr^{-1}}$), and a total SFR of $5.4\,{\rm M_\odot\,yr^{-1}}$ for five infrared peaks in the overlap region from high-resolution $5 - 38\,\mu m$ spectra using the

"Infrared Spectrograph" (IRS) on-board Spitzer. More recently, thanks to the unprecedented spatial resolution of the Herschel-PACS instrument in the FIR, Klaas et al. (2010) could augment the previously determined IR SEDs of individual star-forming knots by additional flux estimates in $70\,\mu m$, $100\,\mu m$, and $160\,\mu m$ in the central disks and the two nuclei. This gives very precise measurements of the total FIR luminosity $L_{\rm FIR}$ in individual knots resulting in integrated values of $1.17\,{\rm M}_\odot\,{\rm yr}^{-1}$ and $0.50\,{\rm M}_\odot\,{\rm yr}^{-1}$ in the nuclei of NGC 4038 and NGC 4039, and a total of $4.84\,{\rm M}_\odot\,{\rm yr}^{-1}$ summing over all knots in the overlap region (see their Table 2). We compare these values to our simulated SFRs in the galactic nuclei of NGC 4038 and NGC 4039 (defined as the central region of each nucleus with a radius of 1 kpc), and the overlap region (chosen according to the central morphology of the simulations). Details are provided in Table 5.2, where we compare the specific regions in the three simulations, namely, the analyzed area (3rd column), the number of stars found in that area compared to the total number of stars (4th column), the number of stars with ages $\tau < 1\,{\rm Myr}$, and the total SFR (5th column). In the case of strong feedback ($q_{\rm EQS} = 1.0$), we obtain SFRs of $1.71\,{\rm M}_\odot\,{\rm yr}^{-1}$ and $4.08\,{\rm M}_\odot\,{\rm yr}^{-1}$ in the nuclei of NGC 4038 and NGC 4039, respectively, but only $0.49\,{\rm M}_\odot\,{\rm yr}^{-1}$ in the overlap region. For intermediate feedback ($q_{\rm EQS} = 0.5$), we obtain $4.55\,{\rm M}_\odot\,{\rm yr}^{-1}$ (nucleus of NGC 4038), $2.85\,{\rm M}_\odot\,{\rm yr}^{-1}$ (nucleus of NGC 4039), and $0.76\,{\rm M}_\odot\,{\rm yr}^{-1}$ in the overlap, while for very weak feedback ($q_{\rm EQS} = 0.01$), we get $0.49\,{\rm M}_\odot\,{\rm yr}^{-1}$ (nucleus of NGC 4038), $0.44\,{\rm M}_\odot\,{\rm yr}^{-1}$ (nucleus of NGC 4039), and $10.88\,{\rm M}_\odot\,{\rm yr}^{-1}$ in the overlap, respectively. We find that, in the case of strong to intermediate feedback ($q_{\rm EQS} = 1.0$, $q_{\rm EQS} = 0.5$), the simulations fall short of producing the most intense starburst in the overlap compared to only a modest star formation activity in the two nuclei. We note, however, that the ratios ${\rm SFR}_{\rm overlap}/{\rm SFR}_{\rm nuclei}$ found in the two simulations are by a factor of about ~ 15 and ~ 20 (!) higher than that reported in a previous Antennae model by Mihos et al. (1993). Quite contrary, in the simulation with $q_{\rm EQS} = 0.01$, a very vigorous overlap starburst develops. This run actually yields a SFR in this region that is even higher than the observed estimate (by a factor of ~ 2), with a very low ratio of ${\rm SFR}_{\rm nuclei}/{\rm SFR}_{\rm overlap} = 0.09$ compared to ~ 0.35 in the Herschel-PACS observations. Since we cannot expect better agreement between the simulations and the data than to a level of a factor of a few, these values are very well consistent with the observations, especially given the fact that we have not discussed any errors in the comparisons here. The total SFR of $14.32\,{\rm M}_\odot\,{\rm yr}^{-1}$, as measured from the simulated SPH particles, is also in very good agreement with the range of observed values between $\sim 5 - 20\,{\rm M}_\odot\,{\rm yr}^{-1}$ (e.g. Zhang et al. 2001), and in good approximate agreement (factor of ~ 1.5) with the value of $22.2\,{\rm M}_\odot\,{\rm yr}^{-1}$ advocated by Klaas et al. (2010). In addition, the latter value compares favorably with respect to the other two simulations with ${\rm SFR} = 7.16\,{\rm M}_\odot\,{\rm yr}^{-1}$ for $q_{\rm EQS} = 1.0$ and ${\rm SFR} = 8.74\,{\rm M}_\odot\,{\rm yr}^{-1}$ for $q_{\rm EQS} = 0.5$, respectively. Therefore, in summary, we conclude that adopting a rather low feedback efficiency for the stellar feedback seems to give the most consistent results with the observational estimates.

What is the reason for such different SFRs in the galactic nuclei and the overlap in

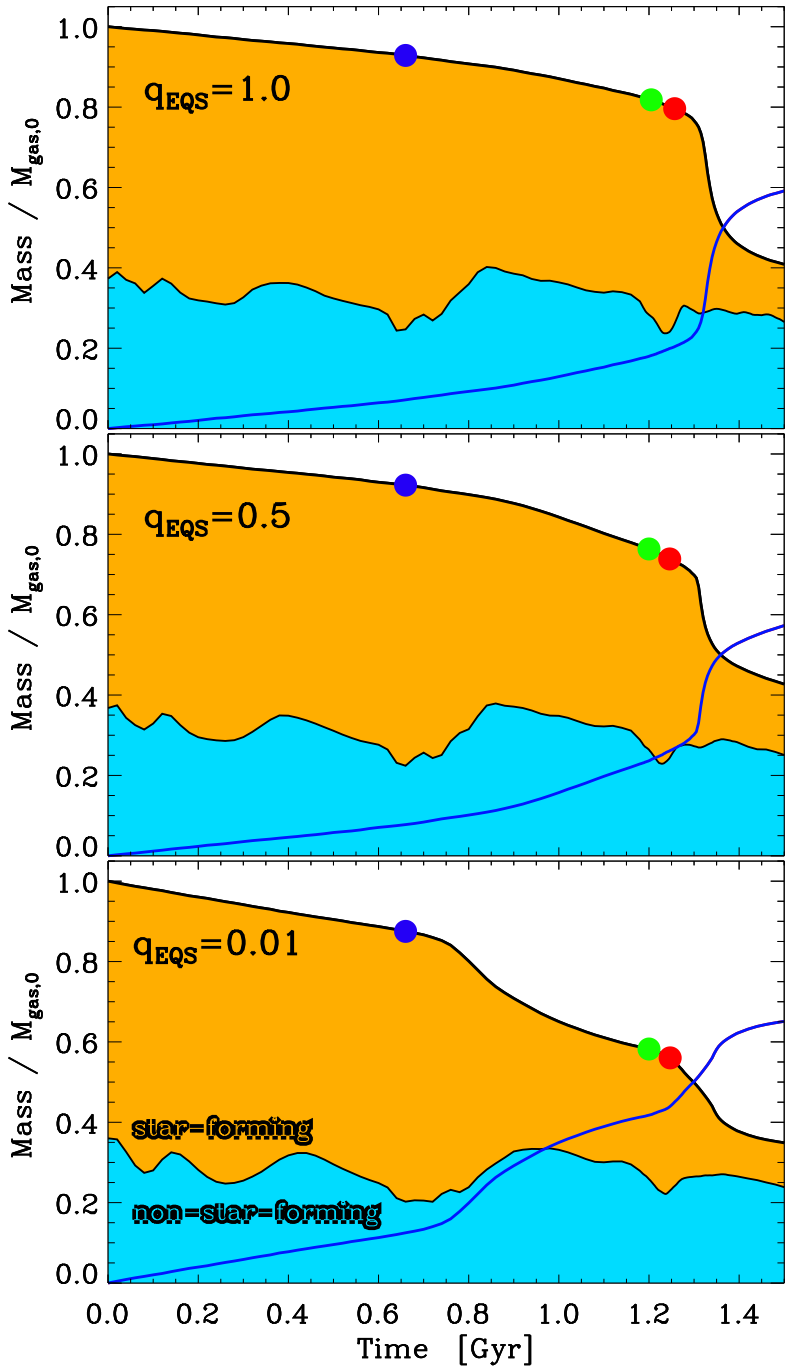

Figure 5.4: Time evolution of the mass in gas (upper black solid line) and newly formed stars (blue line) normalized to the initial gas mass in three simulations with different parameters for the softened equation of state. *Upper panel:* full feedback model $q_{\rm EQS} = 1.0$; *middle panel:* intermediate feedback model, $q_{\rm EQS} = 0.5$; and *lower panel:* model with very weak feedback $q_{\rm EQS} = 0.01$. In addition, we distinguish between the dense star-forming gas ($n > n_{\rm crit}$) treated by the effective multi-phase model (yellow) and non-star-forming gas (blue). The blue, green and red dots indicate the times of first pericenter, second pericenter, and the time of best match in each simulation.

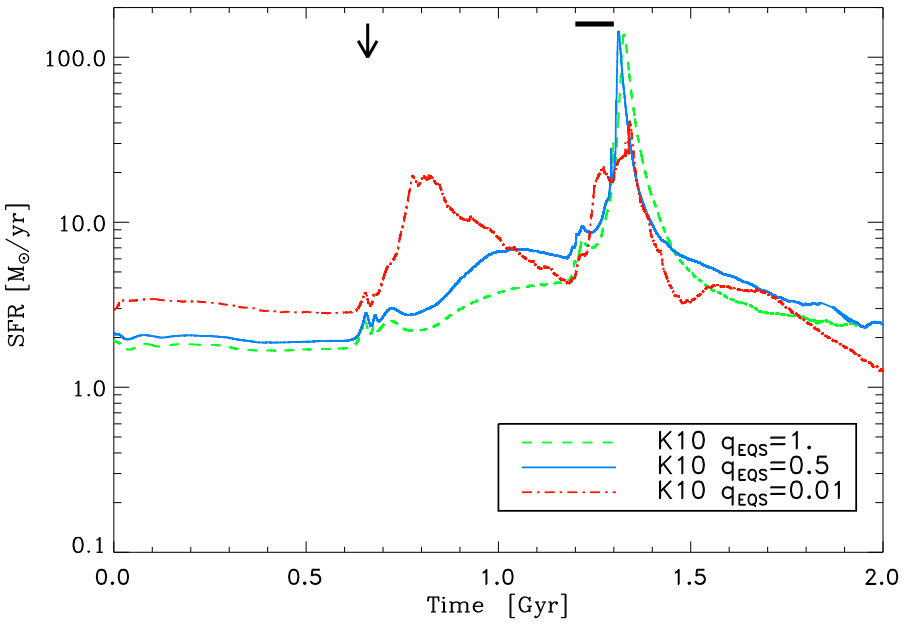

Figure 5.5: Star formation histories for three Antennae simulations with different parameters for the softened equation of state: full (green, $q_{\rm EQS} = 1.0$), intermediate (blue, $q_{\rm EQS} = 0.5$) and weak feedback (red, $q_{\rm EQS} = 0.01$). The arrow gives the time of first close encounter, while the bar indicates the time between second close encounter and final merger.

the simulations with three different $q_{\rm EQS}$? A glimpse at Figure 5.4 reveals a possible explanation. All three simulations show a steady decrease in their gas mass (upper solid line) from the very start of the simulations, corresponding to a gradual build-up of the new stellar component (blue solid line). However, due to the lower pressure support in the effective multi-phase model in the case of the low-feedback simulation (lower panel), it has already turned $\sim 12\%$ of its initial gas mass into stars by the time of the first pericenter (blue dots), whereas the two simulations with stronger feedback (upper and middle panels) have only consumed about $\sim 6\%$ ($q_{\rm EQS} = 1.0$) and $\sim 8\%$ ($q_{\rm EQS} = 1.0$) at the same time. The total amount of non-star-forming gas (blue) stays constant to within $\sim 10\%$ during the whole course of the simulated time span ($t < 1.5\,$Gyr), save some little 'dips' associated with the first and the second pericenter passages ($t = 0.66\,$Gyr and $t = 1.20\,$Gyr). The more dramatic evolution can be seen in the star-forming gas (yellow) which gets efficiently depleted after the first pericenter in the simulation with weak feedback (lower panel), having consumed more than $\sim 40\%$ of its initial gas at the time of second pericenter (green dots). In contrast, in the full-feedback run there are still about 80% of the initial gas mass remaining after the second encounter (green dots), which leads to a very rapid consumption of $\sim 40\%$ of the gas within the first $\sim 100\,$Myr after the final merger (red dots). This is the reason why in the model with weak stellar feedback a large fraction of the high-density gas in the galactic nuclei has already formed stars during the first encounter such that, after

the second encounter, the star formation in localized density peaks of shocked gas in the overlap region gains drastically in relative importance with respect to the nuclear star formation.

A complementary view of this picture is offered by the star formation histories in the three simulations (Figure 5.5, see also Chapter 6). While the simulations with $q_{\rm EQS} = 1.0$ (green dotted line) and $q_{\rm EQS} = 0.5$ (blue solid line) show very similar SFRs initially, the SFR for the $q = 0.01$ simulation is larger by a factor of ~ 2 from the very start. After the first pericenter (indicated by the black arrow), the low-feedback run experiences a significant rise in the SFR by almost a factor of ten, while the other two simulations show a more gradual increase. However, while the low-feedback simulation shows a higher total SFR of $\sim 14\,{\rm M}_\odot\,{\rm yr}^{-1}$ at the time of best match, powered by the short-lived overlap starburst shortly after the second pericenter, the other two simulations build up very powerful nuclear starbursts after the final merger with maximum total SFRs of ${\rm SFR}_{\rm max} \sim 140\,{\rm M}_\odot\,{\rm yr}^{-1}$. An equally powerful starburst does not develop in the case of weak feedback (with ${\rm SFR}_{\rm max} = 40.8\,{\rm M}_\odot\,{\rm yr}^{-1}$). The time between second encounter and final merger is indicated by the horizontal bar in Figure 5.5.

5.5 Comparisons with Observations

The overlap region in the Antennae is dominated by molecular gas. Given that we now have a dynamically viable model, which explains how the overlap region could have possibly formed, detailed investigations of the molecular gas formation process can be undertaken using improved theoretical models (e.g. Robertson & Kravtsov 2008; Pelupessy & Papadopoulos 2009). However, the simulations presented in this and the previous Chapters do not include models for the formation of molecular gas. Therefore, we use an adaptive 3D radiative transfer algorithm to post-process our simulation outputs, as detailed in Section 3.2, to assess the FIR dust emission expected from our simulated data. To summarize shortly, we construct the synthetic FIR maps of the inner regions, covering the galactic disks by iteratively solving the radiation transfer equations until we have converged to the dust equilibrium temperatures. In addition to the stellar emission, we have also included the effects of dust self-absorption and heating. The stellar populations are modeled using Bruzual & Charlot (2003) templates, where we assign ages for the pre-existing disk and bulge particles equally distributed between $0 - 4\,{\rm Gyr}$ and $3 - 7\,{\rm Gyr}$, respectively. Note that a slightly different choice for the particular disk and bulge ages will not change the FIR emission dramatically since it is dominated by the heating of the dust by young stars. The stellar particles formed over the course of the simulation have their age assigned corresponding to the time elapsed since their formation. In addition, we assume (nearly) solar metallicity ($Z = 0.02$) for all stellar particles. This is in reasonable agreement with estimates from young star clusters and the complex hot diffuse gas component in the Antennae

Table 5.3: Model parameters of the radiative transfer calculations.

Property	RT parameter
constant gas-to-dust ratio	124 : 1
extinction law	$R_V = 3.1$
dust model	Draine (2003)
stellar emission model	Bruzual & Charlot (2003)
metallicity	$Z = 0.02$
ages for disk particles	0 - 4 Gyr
ages for bulge particles	3 - 7 Gyr

(e.g. Bastian et al. 2009; Baldi et al. 2006b; Brandl et al. 2009). Finally, we convolve our synthetic images to the resolution of the Herschel PACS camera. We give the RT model parameters in Table 5.3 and refer to Section 3.2 for further details.

In Figure 5.6 we compare FIR maps at 70 μm, 100 μm, and 170 μm with observations by Klaas et al. (2010). Emission from these bands, in general, reveals the sites of hidden recent star formation, that are still embedded in the dusty molecular clouds from which they have formed. We obtain very reassuring agreement between simulations and observations. In particular, the simulated 70 μm, 100 μm, and 160 μm maps all trace the same characteristic sequential locations of the well-confined star-forming regions in the overlap in a very similar way to Figure 1 in Klaas et al. (2010), which we have reproduced in the lower row of Figure 5.6 for better comparison. In addition, the simulated maps recover the locations of individual star-forming knots in the overlap area very well in all three bands compared to similar knots in the Antennae. However, the simulations show additional knotty sub-structure in the northern overlap region which is not detected at a similar level in the observations. We find that the brightest emission in all three bands comes from the overlap region. More specifically, more than 50% of the simulated FIR emission in the three bands originates from the overlap region, compared to only $\lesssim 10\%$ from the two nuclei in NGC 4038 and NGC 4039 combined. A similar percentage (6-8 %) is detected from the two nuclei in the observations in all three Herschel PACS bands. The combined emission from knots K1 to K4 gives a lower bound for the total emission from the overlap region, yielding a total of $\sim 15 - 25\%$ for the three different bands. However, detailed inspection reveals similar differences in the spatial distribution of the simulated and observed FIR emission as in the HI observations (see Figure 5.2). All three upper panels in Figure 5.6 show substantial emission from the southern disk (NGC 4039) that is not seen in the observations (lower panels). This makes the observed disks also look slightly more "tilted" than the simulated ones. Note, however, that this discrepancy is remedied to some extent in the Herschel 160 μm map, which has twice the exposure time than the 70 μm and 100 μm bands. Similarly, we do not find equally strong emission for the progenitor disks, including the arc-like feature in the northern spiral, as is detected

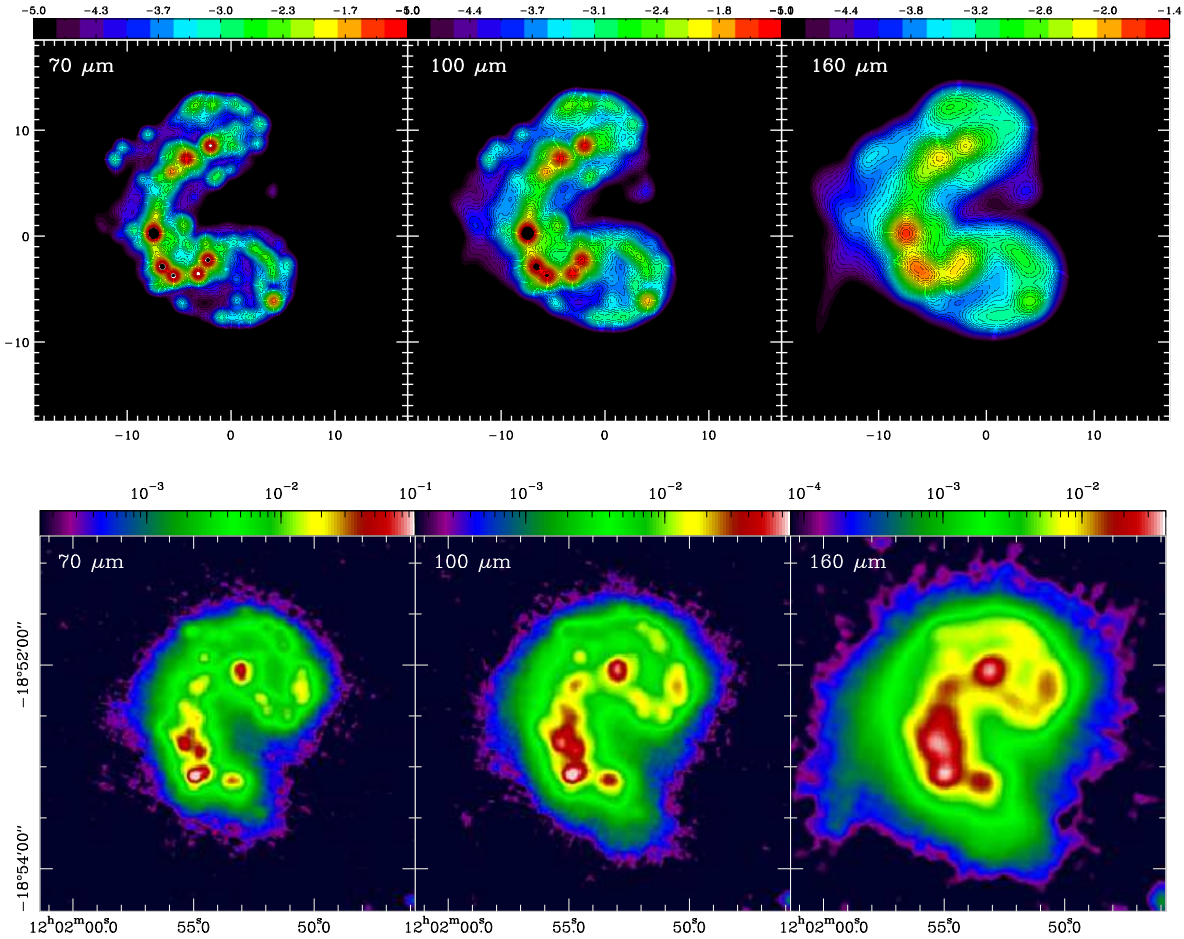

Figure 5.6: Synthetic observations of the inner region of the Antennae at 70 μm *(left column)*, 100 μm *(middle column)*, and 160 μm *(right column)* from the fiducial simulation with $q_{\rm EQS} = 0.01$ *(upper panels)*, obtained by using 3D radiative transfer calculations. These are compared to Herschel PACS observations in the same bands from Klaas et al. (2010; *lower panels*).

in the 100 μm and 160 μm Herschel maps (note also the adopted lower limits in the simulated FIR maps). This may partly be caused by the weak stellar feedback adopted in the simulation, leading to very high local gas densities in the overlap region relative to the rest of the disks, which, in turn, is seen in our simulated FIR maps.

As a further test, we also constructed a simple CO-map from our simulations. Hereby, we first invoke the amount of molecular H_2 from the SFR of the simulated gas particles by using an "inverse" Bigiel et al. (2008) relation of the form

$$\Sigma_{\rm H_2} \;=\; 10 \cdot \left(\frac{\Sigma_{\rm SFR}}{A} \right)^{1/N} \; {\rm M_\odot \, pc^{-2}}. \tag{5.1}$$

where, $\Sigma_{\rm H_2}$ and $\Sigma_{\rm SFR}$ are the surface densities in H_2 and the SFR, respectively, and the

latter is given in $M_\odot\,yr^{-1}\,kpc^{-2}$. A is a normalization constant with $\log(A) = -2.06$, and $N = 0.96$ is a power-law index near unity (see Bigiel et al. 2008, Equation 2 and Table 2). Then, we relate the H_2 masses back to CO by adopting the same CO-to-H_2 conversion factor (see Wilson & Scoville 1990) as given in CO observations by Wilson et al. (2000). We show the synthetic CO map in the left panel of Figure 5.7, compared to an integrated CO map (taken from Figure 1 in Wilson et al. 2000). Since we find it hard to exactly match the contours in the observations (right panel in Figure 5.7), we adopt a very similar, but slightly larger contour range. In particular, we use the same contour range as the observations, putting additional contours at 0.01 and 100, 120, 140, 160 Jy/beam $km\,s^{-1}$ to account for the larger range in the simulations. In the synthetic CO map (left panel in Figure 5.7) we find the CO emission to be entirely confined to the central regions of the merger in a number of distinct high-density peaks in the southern overlap and near the two nuclei. To a lesser extent, we also find emission from two arcs along the southern and northern remnant spirals. The observations exhibit a strikingly similar picture (see right panel in Figure 5.7). The strongest emission peaks from the CO(1-0) transition are detected in the two galactic nuclei, the overlap region, and the north-western spiral arc in NGC 4038, whereas, again, there is no emission in the southern disk as detected at a very low level in the simulation.

Comparing with Figure 5.6, we find that the peaks of both FIR and CO emission coincide very well in the southern part of the overlap region. This is also seen in multi-wavelength comparisons of the Antennae galaxies (e.g., Haas et al. 2000; Klaas et al. 2010), where, e.g. the highest peak at 100 μm, east of the southern nucleus (Klaas et al. 2010, knot "K1"), includes the super-giant molecular cloud complexes SGM3 - SGM5 (indicated in the right panel of Figure 5.7). Similarly, other luminous FIR emission peaks (knots "K2a" and "K2b") are identified with the CO complexes SGM 1 and SGM 2, as well as with peaks number 3 and 4 on radio maps by Hummel & van der Hulst (1986). Note that the latter two FIR knots together encompass the brightest emission region at 160 μm and are located to the north of knot K1 in the highly obscured part of the overlap region (see Figure 3 in Klaas et al. 2010).

5.6 Conclusions

The new numerical model for the Antennae galaxies presented in this Chapter improves on previous models in several key aspects. We find an excellent morphological and kinematical match to the observed large-scale morphology and HI velocity fields (Hibbard et al. 2001). In addition, our model produces a fair morphological and kinematical representation of the observed central region. A strong off-center starburst naturally develops in our fiducial simulation - in good qualitative and quantitative agreement with the observed extra-nuclear star-forming sites (Mirabel et al. 1998; Wang et al. 2004b; Brandl et al. 2009; Klaas et al. 2010). This is a direct consequence of our im-

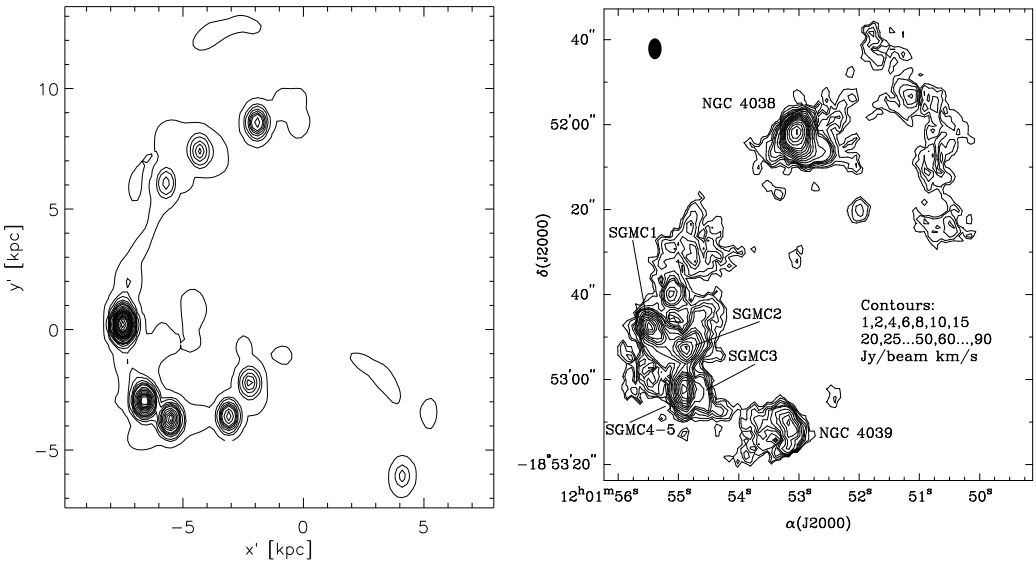

Figure 5.7: *Left panel:* Synthetic CO map of the inner regions of the Antennae from the fiducial simulation with $q_{\rm EQS} = 0.01$, where the integrated CO masses are obtained in a two-step process. H_2 surface densities are obtained from the SFR surface densities of the SPH particles using an "inverse" Bigiel et al. (2008) relation. Then, we apply the same CO-to-H_2 conversion factor as the observations to map the H_2 masses back to CO. *Right panel:* CO integrated intensity map, adapted from Figure 1 in Wilson et al. (2000). The two galactic nuclei and five super-giant molecular clouds in the overlap region are indicated. The filled black oval in the upper left corner gives the size of the synthesized beam in the observations.

proved merger orbit. All previous studies using traditional orbits failed to reproduce the overlap starburst (see e.g. Karl et al. 2008). Additionally, we are naturally guided to choose a less vigorous stellar feedback in our adopted star formation model in order to reproduce the observed properties related to the extra-nuclear starburst in the Antennae.

The exact timing after the second encounter shortly before the final merger ensures that the galaxies are close enough for the efficient tidally-induced formation of the overlap region. The formation of the extra-nuclear starburst is likely to be supported by compressive tidal forces, which can dominate the overlap region in Antennae-like galaxy mergers during close encounters as discussed by Renaud et al. (2008, 2009). In particular, in this simulation, and other simulations in our parameter study with similar central properties, we only find prominent star formation in the overlap region for a very short period of time after the second encounter (see also Figure 4.5). In addition, we find that the observed high-surface density region in the Antennae is not just a chance overlap of the two disks projected along our line-of-sight. Rather it is caused by the actual proximity of the two galaxies after the second close encounter. Thus, a central conclusion of our study is that the strong localized, off-center starbursts observed in the overlap region is a short-lived transient phase in the merging process associated with the recent second encounter, which has a very short lifetime

($\approx$ 20 Myr) if compared to the full merger process ($\approx$ 650 Myr from first encounter to final merger). This serves as a plausible explanation for the fact that such features are scarcely observed in interacting galaxies (Xu et al. 2000). However, the observed puzzling gas concentration between the two nuclei of NGC 6240 (Tacconi et al. 1999; Engel et al. 2010) and the off-center star formation found in other interacting systems (see Section 2.2) might be of a similar origin suggesting that the Antennae overlap region, although rare, is not a unique feature.

Most importantly, our improved model can serve as a solid basis and testbed for further theoretical studies of the enigmatic interacting NGC 4038/39 system, such as the studies presented in detail in the following Chapters. Apart from these, in a first application using this new orbital configuration, we have been able to qualitatively and quantitatively reproduce the magnetic field morphology of the Antennae galaxies (Kotarba et al. 2010) as observed by Chyży & Beck (2004). Thereby, the magnetic field strength was found to saturate at a level corresponding to equipartition between turbulent and magnetic pressure, independent of the initial field strength. High amplifications of the magnetic fields during the interaction suggest that galaxy mergers may be efficient drivers for the cosmic evolution of magnetic fields (see also Drzazga et al. 2011 and Geng et al. 2011 for further discussion).

Finally, accurate modeling of other nearby interacting systems would be desirable to provide further insights into the merger dynamics and timing of observed merging systems. The Antennae galaxies are traditionally in the first place of the classical Toomre sequence which orders galaxies according to their apparent merger stage (Toomre 1977; see also Laine et al. 2003). The "Playing Mice" galaxies (NGC 4676) usually take the second place in the sequence behind the Antennae. They have been successfully modeled with a time of best match between their first and second pericenter (Barnes 2004). According to our proposed model, however, the Antennae galaxies would be in a later merger phase than the Mice, already past the second pericenter. As a consequence, the Antennae would lose their first place in the sequence to the Mice galaxies, requiring a revision of the classical Toomre sequence.

Chapter 6

Disruption of Star Clusters in the Antennae Galaxies

In this Chapter, we reexamine the age distribution of star clusters in the Antennae in the context of N-body+hydrodynamical simulations of these interacting galaxies. All of the simulations that account for the observed morphology and other properties of the Antennae have star formation rates that vary relatively slowly with time, by factors of only $1.3 - 2.5$ in the past 10^8 yr. In contrast, the observed age distribution of the clusters declines approximately as a power law, $dN/d\tau \propto \tau^{\gamma}$ with $\gamma = -1.0$, for ages 10^6 yr $\lesssim \tau \lesssim 10^9$ yr. These two facts can only be reconciled if the clusters are disrupted progressively for at least $\sim 10^8$ yr and possibly $\sim 10^9$ yr. When we combine the simulated formation rates with a power-law model, $f_{\rm surv} \propto \tau^{\delta}$, for the fraction of clusters that survive to each age τ, we match the observed age distribution with exponents in the range $-0.9 \lesssim \delta \lesssim -0.6$ (with a slightly different δ for each simulation). The similarity between δ and γ indicates that $dN/d\tau$ is shaped mainly by the disruption of clusters rather than by the variations in their formation rate. Thus, the situation in the interacting Antennae resembles that in relatively quiescent galaxies such as the Milky Way and the Magellanic Clouds. Parts of this Chapter have been published in Karl, Fall, & Naab 2011, ApJ, 734, 11.

6.1 Why Study Star Clusters in the Interacting Antennae Galaxies?

Interacting galaxies in the nearby universe are laboratories for direct studies of several physical processes that were important in the formation and early evolution of galaxies. From such studies, we hope to learn, for example, how interactions and mergers affect the cycle in which baryonic matter is converted from diffuse interstellar gas into

dense molecular clouds, then into star clusters, and eventually, by disruption, into a relatively smooth stellar field. It is clear that interactions and mergers boost the rate of star and cluster formation. But do they also change the rate at which clusters are disrupted? This is the question we address in this Chapter.

The most intensively studied interacting galaxies are the Antennae (NGC 4038/39), at a distance $D \sim 20\,\mathrm{Mpc}$ (Schweizer et al. 2008, see also Section 2.2). They consist of two normal disk galaxies that began to collide a few $\times 10^8$ yr ago. The stellar population and ISM of the Antennae have been observed over an enormous range of wavelengths, from X-ray to radio (see, e.g. Zhang et al. 2001; Hibbard et al. 2001; Kassin et al. 2003; Zezas et al. 2006; Brandl et al. 2009; Klaas et al. 2010, and Chapter 2). The star clusters have been the focus of numerous studies based on observations with the HST, culminating in well-determined luminosity, mass, age, and space distributions (see Whitmore et al. 2010, Section 2.2, and references therein).

The Antennae have also been the focus of several dynamical simulations, first by Toomre & Toomre (1972) and then by Barnes (1988). As laid out in Chapter 3, these pioneering studies demonstrated that gravity alone can account for the gross features of the observed morphology and kinematics of the stellar components of the merger. Subsequent simulations have included an interstellar medium and star formation, with the additional goal of matching the observed space distribution of young stars in the Antennae (Mihos et al. 1993; Teyssier et al. 2010; Karl et al. 2010, hereafter MBR93, TCB10, and K10, respectively; see also Chapter 5). There have also been two recent attempts to match the observed age distribution of the clusters, with different assumptions about their disruption histories (Bastian et al. 2009, K10).

The purpose of this Chapter is to investigate the issues raised by the observed age distribution of the clusters in the Antennae. We can show that there is nothing special about the disruption history of clusters in the interacting Antennae galaxies; it is similar to that in quiescent (non-interacting) galaxies. The Chapter is organized as follows. In Section 6.2, we review the evidence for a quasi-universal age distribution of star clusters in different galaxies, and in Section 6.3, we assemble the star formation histories from all available N-body+hydrodynamical simulations of the Antennae. We then combine these and compare the results with observations in Section 6.4. We summarize our conclusions and their implications in Section 6.5.

Before proceeding, we offer a few remarks about nomenclature. We use the term "cluster" for any concentrated aggregate of stars with a density much higher than that of the surrounding stellar field, whether or not it also contains gas and whether or not it is gravitationally bound. This is the standard definition in the star formation community (see, e.g. Lada & Lada 2003; McKee & Ostriker 2007). Some authors use the term "cluster" only for gas-free or gravitationally bound objects. Such definitions are not appropriate in the present context for two reasons: (1) A key element in our

analysis is the connection between the formation rates of stars and clusters. We would break this connection artificially if we were to exclude the gas-rich clusters in which stars form. (2) It is virtually impossible to tell from observations which clusters satisfy the virial theorem precisely and which do not, especially at the distance of the Antennae. Indeed, *N*-body simulations show that an unbound cluster retains the appearance of a bound cluster for remarkably long times, more than 10 crossing times (Baumgardt & Kroupa 2007).

6.2 Disruption of Star Clusters

Star clusters form in the dense inner parts of molecular clouds (Lada & Lada 2003; McKee & Ostriker 2007). Most of them are subsequently destroyed by various mechanisms, beginning with the expulsion of interstellar material by massive young stars ("feedback"), later mass loss from intermediate- and low-mass stars, tidal disturbances from passing molecular clouds, and stellar escape driven by internal two-body relaxation (Spitzer 1987; Binney & Tremaine 2008). This leads to the eventual dispersal of stars from the clusters into the surrounding stellar field. In the Milky Way, the fraction of stars in clusters declines with age τ, from $f_{\rm clus} \gtrsim 50\%$ at $\tau \sim 10^6$ yr to $f_{\rm clus} \lesssim 1\%$ at $\tau \sim 10^9$ yr (Binney & Merrifield 1998; Lada & Lada 2003). The goal of this Chapter is to test whether a similar situation holds in the Antennae.

The age distribution of clusters $dN/d\tau$ in a galaxy represents the formation rate $(dN/d\tau)_{\rm form}$ modified by subsequent disruption, leaving behind the *survival* fraction $f_{\rm surv}(\tau)$ of clusters at each age τ:

$$dN/d\tau \;\; = \;\; f_{\rm surv} \cdot (dN/d\tau)_{\rm form}. \qquad (6.1)$$

Thus, if the formation rate varies slowly with time, the age distribution primarily reflects the disruption history of the clusters, i.e., $dN/d\tau \propto f_{\rm surv}$. If, on the other hand, the survival fraction varies slowly, the age distribution primarily reflects the formation history, i.e., $dN/d\tau \propto (dN/d\tau)_{\rm form}$. We assume throughout this work that the formation rates of clusters and stars, $(dN/d\tau)_{\rm form}$ and $dN_*/d\tau$, track each other:

$$(dN/d\tau)_{\rm form} = c \cdot dN_*/d\tau \qquad \text{with} \;\; c = \text{constant}. \qquad (6.2)$$

This is certainly true if most stars form in clusters, as in the Milky Way (Lada & Lada 2003; McKee & Ostriker 2007). Equation (6.2) is the most direct connection between $(dN/d\tau)_{\rm form}$ and $dN_*/d\tau$; hence it may be a good approximation whether or not most stars form in clusters. In the Antennae, we know from Hα observations that at least 20% and possibly all stars form in clusters (Fall et al. 2005).

Fall et al. (2005) found that the age distribution of massive clusters in the Antennae galaxies can be approximated by a power law, $\chi(\tau) \equiv dN/d\tau \propto \tau^\gamma$ with $\gamma \approx -1$.

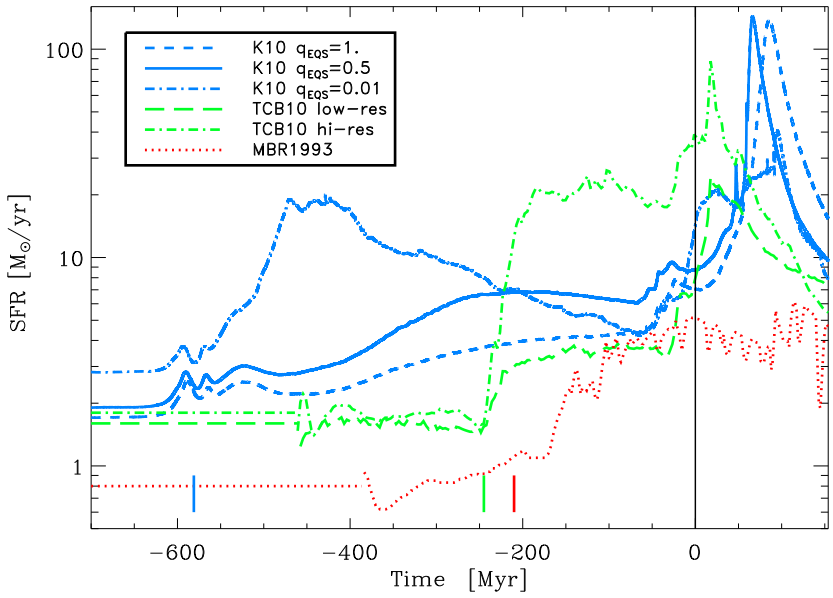

Figure 6.1: Evolution of the star formation rates in different N-body+hydrodynamical simulations of the Antennae galaxies. Blue (Karl et al. 2010, K10; and Chapter 5): strong feedback (dashed), intermediate feedback (solid), weak feedback (dot-dashed); green (Teyssier et al. 2010, TCB10): low-resolution (dotted), high-resolution (dot-dashed); and red dotted (Mihos et al. 1993, MBR93). The time of best match for each simulation is $t = 0$ (at the vertical solid line). The time of first pericenter passage is indicated by colored vertical bars. Straight horizontal lines show the assumed constant star formation rates in the pre-interaction disks.

The mass function of the clusters is also a power law, $\psi(M) \equiv dN/dM \propto M^{\beta}$ with $\beta \approx -2$ (Zhang & Fall 1999). In fact, these results are parts of a broader finding; the bivariate distribution of masses and ages can be approximated by a product of power laws: $g(M,\tau) \propto \psi(M)\chi(\tau) \propto M^{\beta}\tau^{\gamma}$. This model has been derived from observations of massive clusters in the Antennae (roughly $M \gtrsim 10^4(\tau/10^7\mathrm{yr})^{0.7}\,\mathrm{M}_\odot$). The decomposition of $g(M,\tau)$ into a product of $\psi(M)$ and $\chi(\tau)$ implies that the (net) formation and disruption rates of the clusters are independent of their masses[1]. The power-law model for $g(M,\tau)$ has been confirmed in subsequent observational studies of the Antennae clusters (Whitmore et al. 2007; Fall et al. 2009; Whitmore et al. 2010).

Similar results have now been obtained for the age distributions of clusters in about 20 other galaxies (although with smaller samples and thus larger uncertainties than for the Antennae galaxies). These include the Milky Way (Lada & Lada 2003); the Large and Small Magellanic Clouds (Chandar et al. 2010a); NGC 1313, NGC 4395, NGC 5236 (M83), NGC 7793 (Mora et al. 2009; Chandar et al. 2010c); NGC 922 (Pellerin

[1]There is no evidence for mass-dependent disruption of clusters in the Antennae. Claims for mass-dependent disruption in other galaxies (e.g., Gieles et al. 2005) have been largely contradicted by better data and more direct analyses (e.g., Chandar et al. 2011).

et al. 2010); NGC 3256 (Goddard et al. 2010); Arp 284 (Peterson et al. 2009); and nine nearby dwarf galaxies (Melena et al. 2009). The masses and ages of the clusters in these galaxies cover the ranges $10^2\,\mathrm{M}_\odot \lesssim M \lesssim 10^6\,\mathrm{M}_\odot$ and $\tau \lesssim 10^9$ yr. The galaxies themselves are also diverse, ranging from dwarf to giant, quiescent to interacting. Yet in all cases, the observed age distribution of the clusters can be represented by a power law,

$$dN/d\tau \propto \tau^\gamma \quad \text{with} \quad -1.0 \lesssim \gamma \lesssim -0.7, \tag{6.3}$$

where the exponents have uncertainties $\Delta\gamma \approx 0.1 - 0.2$. See Chandar et al. (2010b) for a more complete discussion of these results and the methods used to obtain them.

The *stellar* age distribution is known in detail only for three of the galaxies mentioned above: the Milky Way (Binney & Merrifield 1998 and references therein), the LMC (Harris & Zaritsky 2009), and the SMC (Harris & Zaritsky 2004). In these cases, the SFR has been constant to within a factor of 2 over the past $\sim 10^9$ yr, and we can be certain that the observed age distribution of the clusters primarily reflects their disruption history. From Equations (6.1) and (6.2) and the observed $dN/d\tau$ we obtain[2]

$$f_{\mathrm{surv}} \propto \tau^\delta \quad \text{with} \quad \delta \approx \gamma \approx -1. \tag{6.4}$$

Less is known about the star formation histories in the other galaxies. For some, the rate may have increased over the past $\sim 10^9$ yr, while for others, it may have decreased. However, if we assume that the average formation rate for the sample (which includes a fairly typical mix of galaxies) has been roughly constant, then Equations (6.1) and (6.2) and the observed $dN/d\tau$ again imply $f_{\mathrm{surv}} \overset{\propto}{\sim} \tau^\delta$ with $\delta \approx \gamma \approx -1$. In fact, the average SFR over all galaxies has declined slightly in the past $\sim 10^9$ yr (Lilly et al. 1996; Madau et al. 1996). The alternative to this interpretation is that all 20 galaxies have the same rising star formation rate. However, the probability of this happening by chance is minuscule (roughly $(1/2)^{20} \approx 10^{-6}$ for equal numbers of rising and falling SFRs).

For the Antennae, we have another indication that the observed age distribution of the clusters reflects their disruption history rather than their formation history. Specifically, $dN/d\tau$ has approximately the same power-law shape in regions separated by ~ 10 kpc (Whitmore et al. 2007). This observation can be explained, in principle, either by disruption or by synchronized formation throughout the Antennae. Indeed, the spatial uniformity of $dN/d\tau$, combined with causality restrictions, places interesting constraints on possible temporal variations in the formation rate as follows (Fall et al.

[2]Strictly speaking, the survival fraction must have the limiting behavior $f_{\mathrm{surv}} \to 1$ for $\tau \to 0$ (i.e., before any clusters are disrupted), whereas the power-law model diverges. We could fix this by introducing a bend at some young age τ_b ($\lesssim 10^6$ yr) such that $f_{\mathrm{surv}} \approx 1$ for $\tau < \tau_b$ and $f_{\mathrm{surv}} \propto \tau^\delta$ for $\tau > \tau_b$. This is not necessary in practice, however, because we only make comparisons with binned data (in Section 4), for which the exact behavior of f_{surv} near $\tau = 0$ is irrelevant.

2005, 2009; Whitmore et al. 2007). The timescale for variations in the formation rate, if these are driven by gravitational interactions, is the galactic orbital period, $\sim 10^8$ yr. Similarly, the communication time is 10^8 yr or 10^9 yr for a signal traveling a distance of 10 kpc at a velocity of 100 km s^{-1} or 10 km s^{-1}, respectively, plausible values for pressure disturbances in the ISM. In either case, we expect the formation rate to vary relatively slowly, an expectation borne out nicely by the N-body+hydrodynamical simulations presented in the next section.

The mechanisms that disrupt clusters include the following: (1) removal of ISM by stellar feedback, $\tau \lesssim 10^7$ yr (Hills 1980); (2) continued mass loss from intermediate- and low-mass stars, 10^7 yr $\lesssim \tau \lesssim 10^8$ yr (Chernoff & Weinberg 1990); (3) tidal disturbances by passing molecular clouds, $\tau \gtrsim 10^8$ yr (Spitzer 1958); (4) stellar escape driven by internal two-body relaxation, $\tau \gtrsim 10^9$ yr (Spitzer 1987). The timescales quoted above are highly approximate, and some of the mechanisms must in fact operate simultaneously. The interested reader is referred to Fall et al. (2009) and Fall et al. (2010) for further discussion of disruption mechanisms and how they relate to the mass and age distributions. In the present context, it is important to note that mechanisms (1), (2), and (4) have little or no dependence on the properties of the host galaxy. Only mechanism (3)—encounters with molecular clouds—is expected to have such a dependence, through the mean density of molecular gas. In practice, however, this is likely to make relatively little difference over much of the observed range of ages, and we therefore expect $f_{\rm surv}$ to be similar in different galaxies, consistent with the observations summarized above.

6.3 N-Body+Hydrodynamical Simulations

Interacting and merging galaxies like the Antennae generally show signs of enhanced star formation in the past few $\times 10^8$ yr, along with more complex morphology and kinematics, compared with isolated disk galaxies. In this Section, we briefly present and analyze all previously published simulations of the Antennae galaxies together with three simulations with varying $q_{\rm EQS}$ we presented in Chapter 5, that make specific predictions for their star formation history. We do not claim that any of these simulations uniquely represents the real Antennae system. In particular, the spatial and temporal resolution in the simulations is much too low to model the ISM accurately on the scales of individual star clusters (Bekki et al. 2002; Kravtsov & Gnedin 2005; Li et al. 2004)[3]. Nevertheless, these simulations provide us with a suite of plausible star formation histories for the Antennae. We adopt this approach because it would be difficult, if not impossible, to determine the stellar age distribution in the Antennae directly from observations.

[3]See Bournaud et al. (2008) for a first attempt to simulate cluster formation directly and Renaud et al. (2008, 2009) for the possible effects of compressive tides on cluster formation.

Following the first *N*-body simulation of the Antennae galaxies by Toomre & Toomre (1972), several groups have improved the purely stellar dynamical models of the system (Barnes 1988; Hibbard 2003; Renaud et al. 2008, 2009). However, there are still only a few *N*-body+hydrodynamical simulations that predict star formation histories of the Antennae and, at the same time, provide a reasonable match to the gross morphology and kinematics of the system.

In the MBR93 simulation, the ISM is represented by discrete clouds that evolve by merging and fragmentation. Star formation is modeled using a Schmidt (1959) relation, $\dot{\rho}_* \propto \rho^{1.8}$, with an initial gas depletion timescale of $\approx 7\,\mathrm{Gyr}$ (see Mihos et al. 1991, 1992 for details). The spatial and mass resolutions for the baryonic component (stars) are $x_{\mathrm{res}} = 200\,\mathrm{pc}$ and $m_{\mathrm{res}} = 6.8 \times 10^6\,\mathrm{M}_\odot$. The Antennae are modeled as two interacting identical disk galaxies (see Barnes 1988) on an elliptical orbit with initial disk inclinations as in Toomre & Toomre (1972). At the time of best match, after the first pericenter passage, the total SFR has increased by a factor of 6 with respect to the progenitor disks. Most of the star formation is concentrated in the two nuclei, with very little in the overlap region between them. Observations show, however, that most of the recent star and cluster formation takes place in the overlap region (e.g. Stanford et al. 1990; Mirabel et al. 1998; Zhang et al. 2001). We have reproduced the star formation history from Figure 10 of MBR93 in our Figure 6.1 (red dotted line). The intermittent nature of star formation in the MBR93 simulation, i.e. the rapid fluctuations in the overall SFR, is very likely a result of their particular discrete-cloud model of the ISM. To extend the simulated star formation histories to $\tau \gtrsim 10^9\,\mathrm{yr}$, we assume a constant rate of star formation before the start of the simulations (i.e., the time at which the full *N*-body+hydrodynamical interactions are switched on). We adopt the same procedure for all the other simulations presented in the remainder of this Section (see the constant horizontal lines in Figure 6.1).

In Chapter 5, we presented the first simulations of the Antennae that account for the extended star formation in the overlap region. Since these simulations all share the same orbit, we name them "K10", in reference to the first publication of the orbit in Karl et al. (2010), in order to distinguish them from the other hydrodynamical simulations discussed in this Chapter. For the K10 simulations, the ISM is modeled using the SPH method (Chapter 3, see also Monaghan 1992 for a review). Star formation again follows a Schmidt relation, with $\dot{\rho}_* \propto \rho^{3/2}$ and a characteristic gas depletion timescale of $t_0^* = 8.4\,\mathrm{Gyr}$ at the star formation threshold, $n_{\mathrm{crit}} = 0.128\,\mathrm{cm}^{-3}$. The simulations also include stellar feedback (Springel & Hernquist 2003), and the baryonic spatial and mass resolutions are $x_{res} = 35\,\mathrm{pc}$ and $m_{res} = 7 \times 10^4\,\mathrm{M}_\odot$. The progenitor galaxies were merged on a mildly elliptical orbit with disk orientations and a time of best match that resulted in better agreement with the observed large- and small-scale morphology and line-of-sight kinematics compared with previous Antennae simulations. In particular, the K10 simulations are the only published simulations that give a reasonable spatial

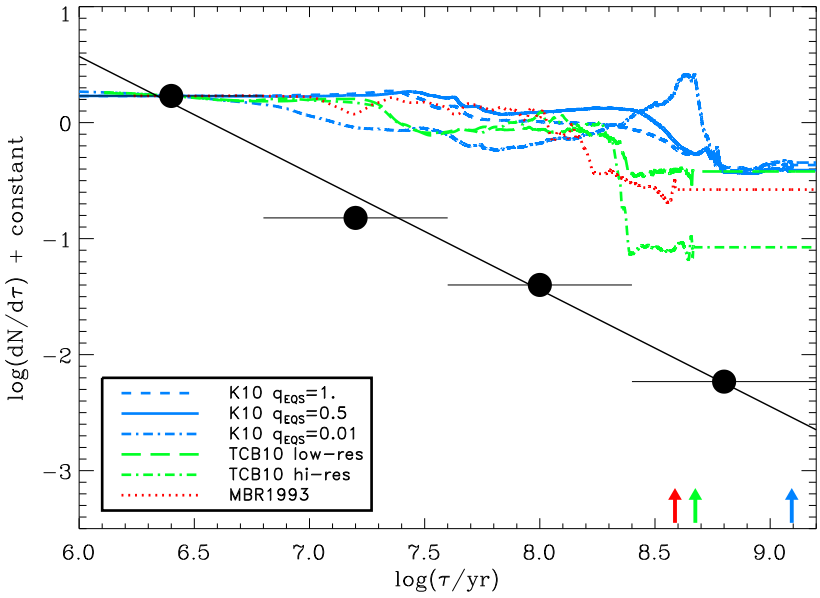

Figure 6.2: Age distribution of star clusters derived from the star formation histories in the simulations shown in Figure 6.1 (without disruption). For comparison, we plot the observed age distribution of clusters with $M \geq 2 \times 10^5\,\mathrm{M}_\odot$ in the Antennae (filled dots) from Fall et al. (2005). The diagonal line represents the power-law model, $dN/d\tau \propto \tau^\gamma$ with the best-fitting exponent $\gamma = -1.01 \pm 0.03$. The simulated age distribution has been normalized to match the observed one at the midpoint of the youngest bin. The zeropoint of age is the time of best match in the simulations. The colored arrows indicate the starting times of the simulations.

distribution of recent star formation activity, including the observed starburst in the overlap region (Karl et al. 2010; Kotarba et al. 2010, Chapter 5).

For the present analysis, we shortly summarize the results from the simulations presented in Chapter 5. In these simulations, stellar feedback heats and pressurizes the ISM, thereby suppressing and regulating star formation (Springel & Hernquist 2003). The energy input is controlled by a dimensionless parameter q_{eqs} that ranges from 0 (no feedback) to 1 (full feedback, see Springel et al. 2005 for details). In Figure 6.1, we show the star formation histories for the simulations with full feedback ($q_{\mathrm{eqs}} = 1$, blue dashed), intermediate feedback ($q_{\mathrm{eqs}} = 0.5$, blue solid), and very weak feedback ($q_{\mathrm{eqs}} = 0.01$, blue dot-dashed). The SFR in the simulation with the strongest feedback ($q_{\mathrm{eqs}} = 1$) increases only modestly after the first pericenter passage (vertical blue bar) and then again after the second pericenter passage, until it is 4 times higher at the time of best match than in the pre-interaction disk phase. Reducing the feedback ($q_{\mathrm{eqs}} = 0.5$) results in a more efficient consumption of gas after the first close passage. At the time of best match, the SFR has increased only by a factor of 5. In the case of weak feedback ($q_{\mathrm{eqs}} = 0.01$), the gas is consumed more rapidly in an early interaction phase, with a peak in star formation about 150 Myr after the first pericenter passage.

Thereafter, the SFR drops rapidly and then increases following the second pericenter passage to 5 times the initial value at the time of best match (see also discussion in Section 5.4). Most of the star formation then occurs in the overlap region rather than in the two nuclei, in reasonable agreement with observations (Zhang et al. 2001; Wang et al. 2004b; Brandl et al. 2009; Klaas et al. 2010; see also Section 2.2).

TCB10 have recently presented a set of Antennae simulations based on the adaptive mesh refinement (AMR) grid code RAMSES (Teyssier 2002) with the orbit of an earlier *N*-body simulation by Renaud et al. (2008, 2009). They model the ISM with a polytropic equation of state. Stellar feedback is not included, but thermal support is added on small scales to avoid artificial fragmentation. As in the simulations described above, star formation is modeled using a Schmidt relation in the form $\dot{\rho}_* \propto \rho^{3/2}$. TCB10 present low-resolution ($x_{res} = 96\,\mathrm{pc}, m_{res} = 10^6\,\mathrm{M}_\odot$) and high-resolution ($x_{res} = 12\,\mathrm{pc}, m_{res} = 4 \times 10^4\,\mathrm{M}_\odot$) simulations in which the star formation thresholds are scaled (by almost two orders of magnitude higher in the latter case) to give similar SFRs in the progenitor disks. The gas depletion timescales at the star formation threshold are 16 Gyr and 2 Gyr, respectively, for the low- and high-resolution simulations. The star formation history of the TCB10 low-resolution simulation is shown by the green dashed line in Figure 6.1. As in the MBR93 simulation, the SFR increases moderately after the first pericenter passage (vertical green bar), by a factor of 4 at the time of best match. In the high-resolution simulation (green dot-dashed), the increase in the SFR after first pericenter passage is more dramatic, about 20 times higher at best match than in the progenitor disks. The star formation history, however, parallels the low-resolution case with an almost constant offset. In the K10 simulation with $q_{\mathrm{eqs}} = 0.01$, a similar rise in the SFR after the first pericenter passage resulted from weak feedback. The high-resolution TCB10 simulation shows a more extended distribution of star-forming sites, but these are not as smoothly connected as in the K10 simulations or as in the real Antennae (see Figure 1 in TCB10). Furthermore, the TCB10 simulations do not reproduce the observed starburst in the overlap region.

The star formation histories in the simulations assembled here show a great deal of diversity, due to different orbits (merger timescales, orientations, etc.) and/or different prescriptions for star formation and stellar feedback. The differences in the SFRs can be as much as an order of magnitude at a given evolutionary phase (e.g., the first pericenter passage). In all cases, the SFR is enhanced by the interaction relative to the quiescent disk phase, by factors of $4 - 20$ at the time of best match. However, most of this variation occurs early during the interaction, shortly after the first pericenter passage. In contrast, for $\tau \lesssim 2 \times 10^8$ yr, the SFR varies remarkably slowly, by factors of 3 or less. This near-constancy of the recent SFR plays an important role in our interpretation of the observed age distribution of the star clusters in the Antennae galaxies.

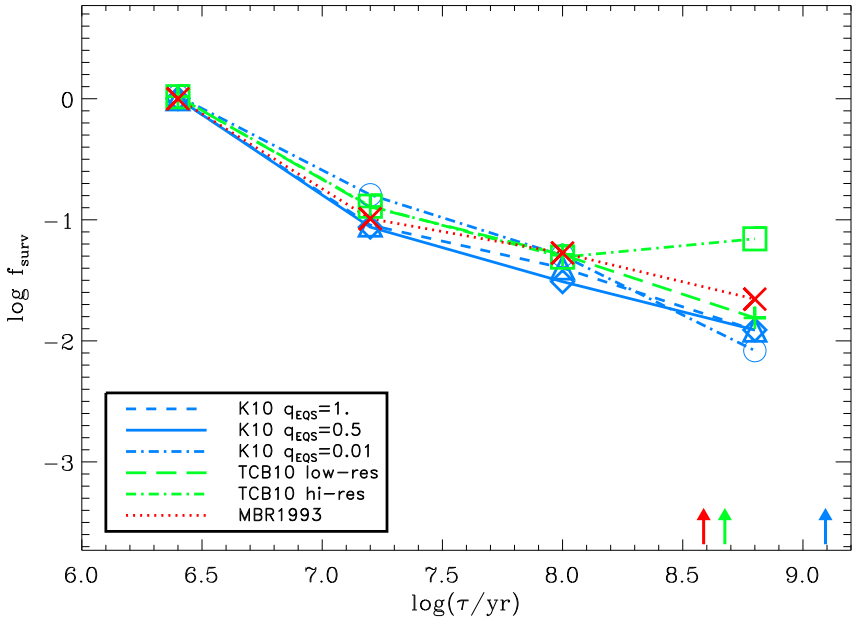

Figure 6.3: Implied survival fraction of star clusters in the Antennae, $f_{\rm surv} \equiv (dN/d\tau)/(dN/d\tau)_{\rm form}$, plotted against age, with $dN/d\tau$ from Fall et al. (2005) and $(dN/d\tau)_{\rm form}$ from the simulations shown in Figure 6.1 (binned in the same way as the observations). The colored arrows indicate the starting times of the simulations.

6.4 Comparisons with Observations

We now compare the simulations with observations. The smooth curves in Figure 6.2 show the same simulated SFRs as Figure 6.1, but now plotted as $\log(dN/d\tau)$ against $\log(\tau/{\rm yr})$ with the zeropoint of age ($\tau = 0$) taken to be the time of best match for each simulation. The data points in Figure 6.2 show the observed age distribution of massive clusters ($M \geq 2 \times 10^5\,{\rm M}_\odot$) in the Antennae from Fall et al. (2005). The statistical uncertainties ($\sqrt{N}$) in each bin are 0.05 – 0.06 dex, about half the radius of the plotted symbols. The diagonal line in Figure 6.2 shows the power law that best fits the observations: $dN/d\tau \propto \tau^\gamma$ with $\gamma = -1.01 \pm 0.03$. We have normalized the simulated and observed $dN/d\tau$ to a common value at the first data point. What is striking about Figure 6.2 is the divergence between the simulations and observations with increasing age, indicative of progressive disruption. At $\tau = 10^8$ yr, for example, the observed age distribution has declined by a factor of 42, while the simulated formation rates have declined by factors of only 1.3 – 2.5, even in the midst of a dramatic collision between the galaxies. This illustrates the main conclusion of this Chapter: both the observed age distribution and simulated formation rates of clusters in the interacting Antennae galaxies resemble those in quiescent (non-interacting) galaxies. We demonstrate this conclusion more quantitatively in the remainder of this section.

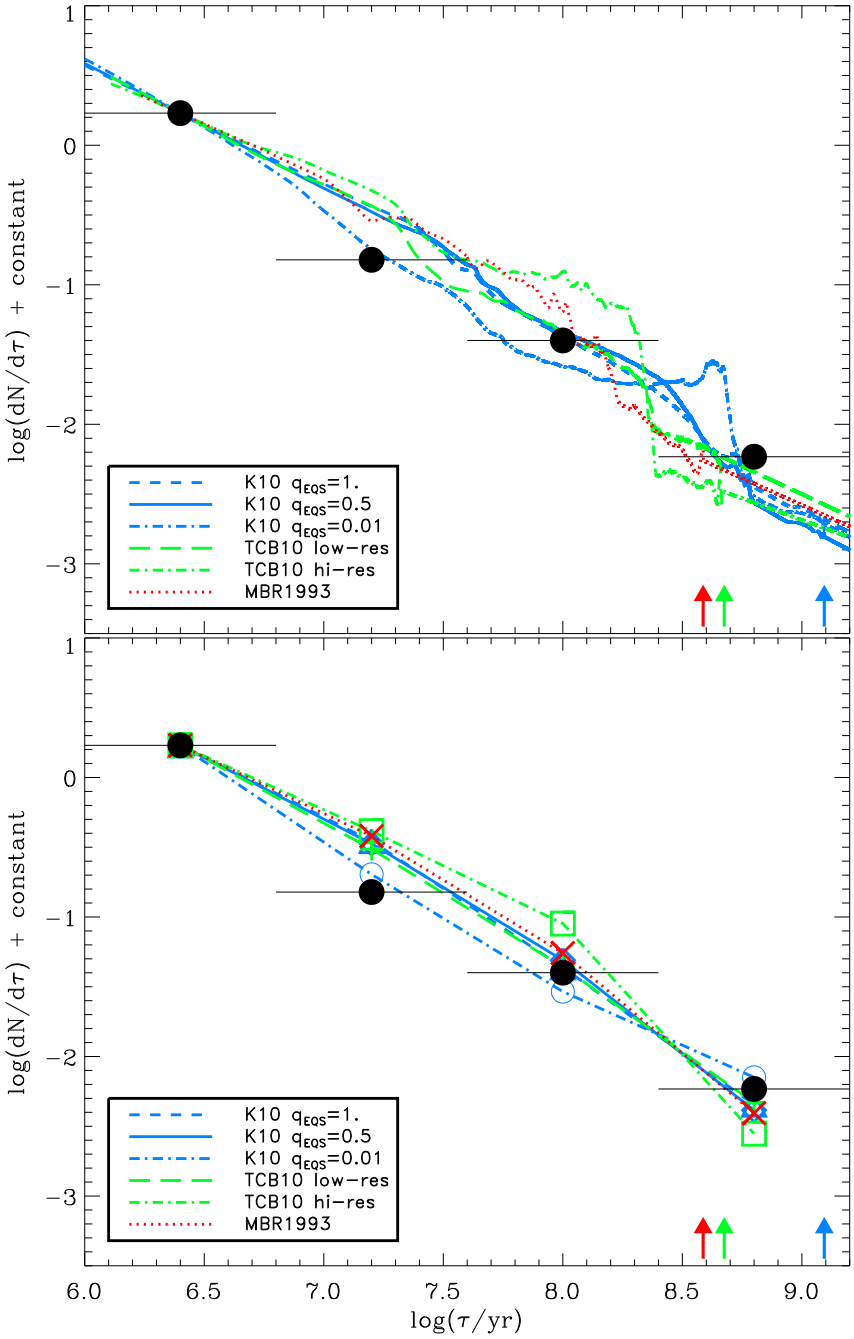

Figure 6.4: Predicted age distribution of star clusters based on the simulated formation rates shown in Figure 6.1 and the power-law model for the survival fraction, $f_{\rm surv} \propto \tau^{\delta}$, with the best-fitting exponents listed in Table 6.1. For comparison, we show the observed age distribution (filled dots) from Fall et al. (2005). In the upper panel, the formation rates are unbinned; in the lower panel, they are binned in the same way as in the observations. The colored arrows indicate the starting times of the simulations.

The age distribution shown in Figure 6.2 is based on *UBVI*Hα images taken with the Wide Field Planetary Camera 2 on *HST*. The masses and ages of the clusters were derived by comparing their luminosities and colors with stellar population models while correcting for interstellar extinction. The resulting age distribution is not sensitive to the particular choice of models or extinction curve. The data points plotted in Figure 6.2 pertain to a mass-limited sample with $M \geq 2{\times}10^5\,\mathrm{M}_\odot$, which is essentially complete for ages up to $\tau \approx 10^9$ yr. The age distributions for samples limited at lower masses have the same power-law shape but do not extend to such large ages. In constructing the age distribution, relatively large bins were chosen ($\Delta \log \tau = 0.8$) in order to smooth over small-scale features caused by the systematic errors that arise whenever masses and ages are estimated from multiband photometry. The most insidious of these is the artificial gap at $\tau \approx (1-2) \times 10^7$ yr resulting from stochastic variations in the colors of clusters caused by rapid evolution of a few bright red supergiant (RSG) stars. This so-called RSG gap, and other, less prominent features, affect *every* age distribution in this field — not just the one for the Antennae. The only practical way to minimize the corresponding systematic errors in the age distribution is to choose relatively large bins and to avoid centering any of them on the RSG gap. In the future, it may be possible to reduce the prominence of the RSG gap by augmenting the *UBVI*Hα photometry with additional infrared photometry in several bands and/or spectra of large samples of clusters. The interested reader is referred to Fall et al. (2005) for a more complete discussion of the age distribution shown in Figure 6.2, including the many tests that were performed to determine its accuracy and robustness. Confirmation and further analysis can be found in the papers by Whitmore et al. (2007, 2010) and Fall et al. (2009).

The common normalization of $dN/d\tau$ at small τ in Figure 6.2 for both simulations and observations is required by our assumption that the formation rates of stars and clusters are linked together by Equation (6.2). In principle, we should equate $dN/d\tau$ and $(dN/d\tau)_{\rm form}$ at $\tau = 0$, the only age at which we can be certain that no clusters have yet been disrupted, that they are all intact and observable, even if some of them are not gravitationally bound and will eventually disperse. This procedure implicitly fixes the constant of proportionality c in Equation (6.2) between the formation rates of stars and observed clusters (in this case, those with $M \geq 2 \times 10^5\,\mathrm{M}_\odot$). The dispersal time for unbound clusters is $\Delta\tau \sim 10^7$ yr (~ 10 crossing times; see Fall et al. 2005 and Baumgardt & Kroupa 2007). Thus, by matching $dN/d\tau$ and $(dN/d\tau)_{\rm form}$ at $\tau = 2.5 \times 10^6$ yr rather than $\tau = 0$, we likely make only a small error, of order unity or much less. It would be a mistake to equate $dN/d\tau$ and $(dN/d\tau)_{\rm form}$ at $\tau >> 10^7$ yr because in general this would cause a mismatch at young ages, the only part of the distribution for which disruption is guaranteed to be negligible.

We now explore several quantitative measures of the progressive disruption of clusters indicated by Figure 6.2. First, we divide the observed age distribution by the simulated formation rates (after binning in the same way) to obtain the implied sur-

Table 6.1: Best-fit exponent δ in the power-law model of the survival fraction.

Model	K10 $q = 1.0$	$q = 0.5$	$q = 0.01$	TCB10 low-res	hi-res	MBR1993
δ	-0.86	-0.89	-0.88	-0.80	-0.62	-0.77
Errors	0.01	0.01	0.02	0.01	0.02	0.01

vival fraction, $f_{\rm surv} \equiv (dN/d\tau)/(dN/d\tau)_{\rm form}$. This is plotted as a function of age in Figure 6.3. Evidently, $f_{\rm surv}$ declines monotonically up to $\tau = 10^8$ yr for all simulations and up to $\tau = 6 \times 10^8$ yr for all but one simulation. The statistical significance of the decline in $f_{\rm surv}$ is 17–20 σ from the first bin to the second, 5–9 σ from the second bin to the third, and 8–16 σ from the third bin to the fourth (again with one exception). Thus, a constant $f_{\rm surv}$ is definitely ruled out. A corollary of this result is that disruption continues at least up to $\tau \sim 10^8$ yr and possibly up to $\tau \sim 10^9$ yr. From Figure 6.3, it also appears that the survival fraction declines roughly as a power law of age.

We can make a more direct test of the power-law model for the survival fraction, $f_{\rm surv} \propto \tau^{\delta}$, by combining it with the formation rate $(dN/d\tau)_{\rm form}$ as in Equations (6.1) and (6.2). We then obtain the best-fit values of δ by minimizing χ^2 between the predicted and observed age distributions $dN/d\tau$. The results of this comparison are listed in Table 6.1 and shown in Figure 6.4. In the upper panel of the figure, we plot the predicted $dN/d\tau$ without binning, while in the lower panel, we plot it with the same binning as the observations. The best-fit exponents lie in the range $-0.9 \lesssim \delta \lesssim -0.6$ (with minor differences among the simulations). These are similar to, but slightly larger than the exponent $\gamma = -1.0$ of the observed age distribution, because the simulated formation rates decline gradually with age (at least for $\tau \lesssim 2 \times 10^8$ yr). We do not expect perfect agreement between any of the predicted and observed age distributions, because, as noted in Section 6.3, there is substantial diversity among the simulated formation histories themselves. Nevertheless, as Figure 6.4 shows, the predicted age distributions for all six simulations follow the same general, power-law trend as the observed age distribution. This is additional support for our conclusion that clusters in the Antennae are disrupted progressively over an extended period and in a manner similar to that in more quiescent galaxies such as the Milky Way and the Magellanic Clouds. It is also gratifying to note that the simulation that best matches the age distribution (the K10 $q_{\rm EQS} = 0.01$ simulation, dot-dashed blue line in Figure 6.4) also reproduces the extended star formation in the overlap region (see Chapter 5).

Bastian et al. (2009) reached a different conclusion: that the disruption of clusters ceases at $\tau \sim 10^7$ yr in the Antennae. Their analysis differs from ours in several respects. (1) Bastian et al. base their claim only on the MBR93 simulation. This simulation, however, fails to reproduce the observed spatial extent of recent star formation in the overlap region of the Antennae. (2) They equate the observed age distribution $dN/d\tau$ and the simulated formation rate $(dN/d\tau)_{\rm form}$ at relatively old ages, $\tau \sim 10^8$ yr.

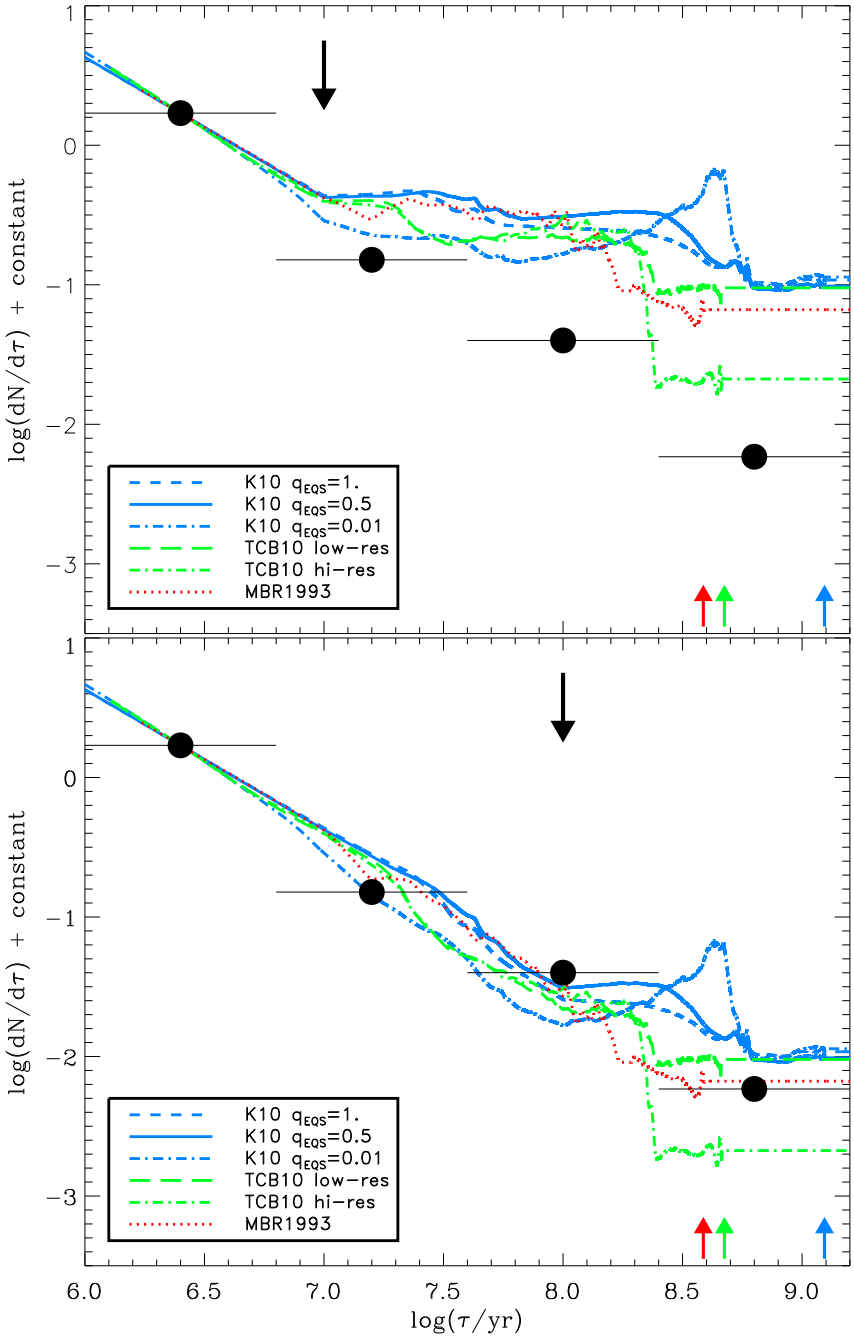

Figure 6.5: Predicted age distribution of star clusters based on the simulated formation rates shown in Figure 6.1, the power-law model for the survival fraction, $f_{\rm surv} \propto \tau^{\delta}$ with $\delta = -1.0$, and different assumptions about when disruption ends. We set $f_{\rm surv} = \text{constant}$ for $\tau \geq 10^7\,{\rm yr}$ in the upper panel and for $\tau \geq 10^8\,{\rm yr}$ in the lower panel (indicated by the black arrows). The filled circles denote the observed age distribution from Fall et al. (2005). The colored arrows indicate the starting times of the simulations.

As we have emphasized above, $dN/d\tau$ and $(dN/d\tau)_{\rm form}$ must be matched near $\tau \approx 0$ in order to connect the formation rates of clusters and stars. (3) Bastian et al. have adopted an age distribution with a dip at $\tau = (1-3) \times 10^7$ yr and a secondary peak at $\tau = (3-10) \times 10^7$ yr from Whitmore et al. (2007). This is based on the same observations as the age distribution adopted here, but it has narrower bins ($\Delta \log \tau = 0.5$), one of which, unfortunately, is centered right on the RSG gap[4].

We can now perform a test on the hypothesis of a "young-aged" cluster disruption by adopting the power-law model $f_{\rm surv} \propto \tau^{\delta}$ with $\delta = -1.0$, assuming disruption to end at some age $\tau_{\rm end}$, and setting $f_{\rm surv} =$ constant thereafter. The particular choice of $\delta = -1.0$ states the limiting case given by the observations (presupposed that the star formation is not falling in the Antennae over the last $\sim 10^{7...8}$ yr), assuring that we assume efficient disruption for clusters with ages $\tau < \tau_{\rm end}$. The results are shown in the upper panel of Figure 6.5 for $\tau_{\rm end} = 10^7$ yr and in the lower panel for $\tau_{\rm end} = 10^8$ yr, using the same format as Figure 6.4 (which, in effect, has $\tau_{\rm end} \rightarrow \infty$). The fact that the predicted age distributions always lie well above the observed one, at least for short-lived cluster disruption ending at $\tau_{\rm end} = 10^7$ yr, demonstrates again the necessity for disruption over an extended period, certainly up to 10^8 yr and possibly beyond. In order to be consistent with Figure 10 from Bastian et al. (2009), we repeat our analysis using the age distribution from Whitmore et al. (2007) and find consistent results. We show the comparisons based on a power-law $f_{\rm surv}$ truncated at $\tau_{\rm end} = 10^7$ yr and 10^8 yr in Figure 6.6. Here again, the predictions lie well above the observations for $\tau_{\rm end} = 10^7$ yr. Hence, we cannot confirm the picture of a short cluster disruption for young ages ($\tau \lesssim 10^7$ yr), rather Figures 6.5 and 6.6, again, reinforce our conclusion that disruption seems to be important over extended periods. Moreover, the characteristic dip-peak structure in the age distribution is not reproducible by any of the simulations considered here and we, therefore, regard it as an unphysical artifact associated with the RSG gap.

6.5 Conclusions

The main conclusion of this Chapter is that the star clusters in the interacting Antennae galaxies are disrupted in much the same way as those in other galaxies. In most if not all star-forming galaxies, including the Antennae, the observed age distribution of clusters can be approximated by a power law, $dN/d\tau \propto \tau^{\gamma}$, with an exponent in the range $-1.0 \lesssim \gamma \lesssim -0.7$ (see Chandar et al. 2010b and Section 6.2 here). In general, this must reflect the combined formation and disruption histories of the clusters. However,

[4]In fact, Whitmore et al. (2007) present two age distributions (in their Figures 4 and 15). The first one, adopted by Bastian et al. (2009), was intended mainly for comparison with Monte Carlo simulations. When we fit a power law to this age distribution, we obtain $\gamma = -0.98 \pm 0.14$. The second age distribution presented by Whitmore et al. is essentially the same as the one presented by Fall et al. (2005).

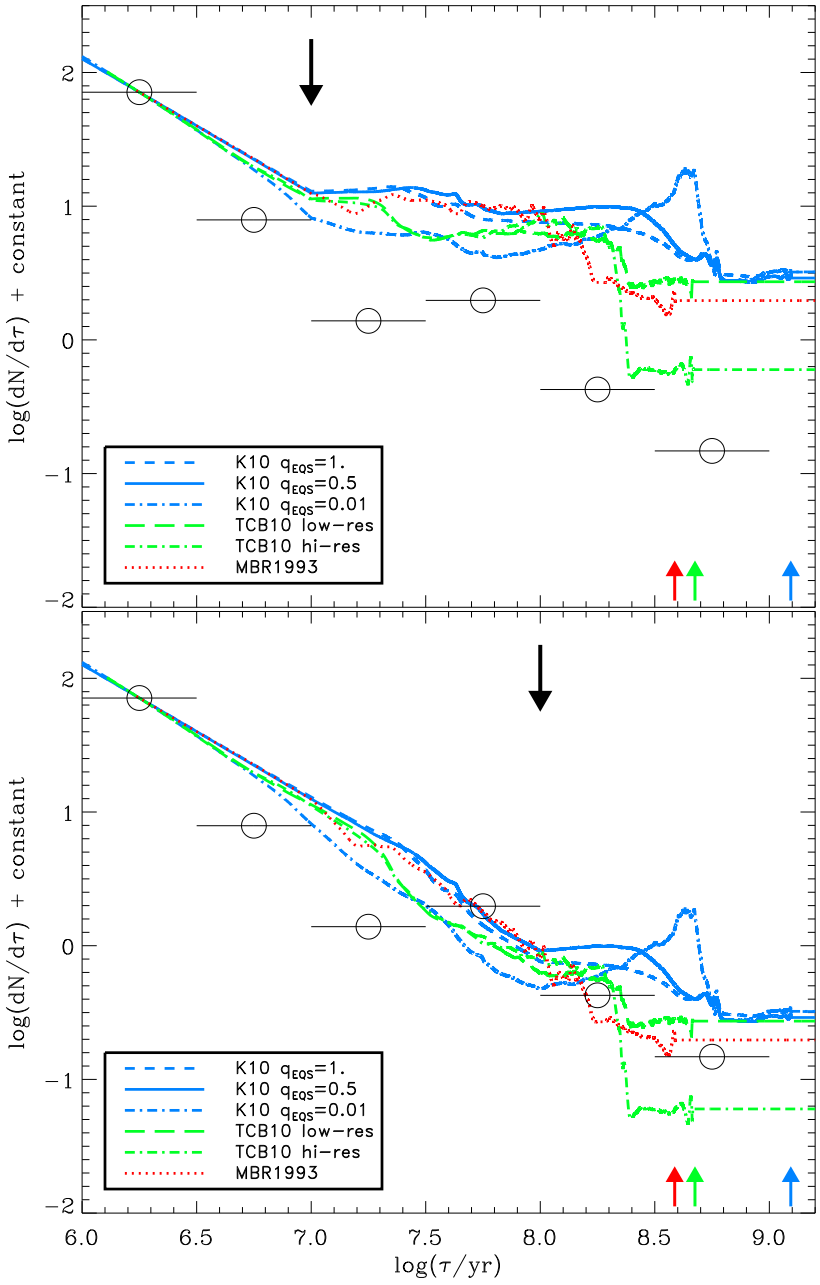

Figure 6.6: Predicted age distribution of star clusters based on the simulated formation rates shown in Figure 6.1, the power-law model for the survival fraction, $f_{\rm surv} \propto \tau^{\delta}$ with $\delta = -1.0$, and different assumptions about when disruption ends. We set $f_{\rm surv} = {\rm constant}$ for $\tau \geq 10^7\,{\rm yr}$ in the upper panel and $\tau \geq 10^8\,{\rm yr}$ in the lower panel (indicated by the black arrows). The colored arrows indicate the starting times of the simulations. This diagram is the same as Figure 6.5 except that the observed age distribution here is taken from Figure 4 of Whitmore et al. (2007).

variations in the formation rate are expected to be of minor influence because $dN/d\tau$ is so similar in different galaxies and declines by such a large factor, typically $\sim 10^2$, over a relatively small range of age, $\tau \lesssim 10^8$–10^9 yr (i.e., less than 10% of the lifetime of the galaxies). Indeed, in several well-studied galaxies (the Milky Way and the Magellanic Clouds), the SFR is known from observations to have been nearly constant for the past $\sim 10^9$ yr, compelling evidence that the decline in $dN/d\tau$ is mainly a consequence of disruption (Binney & Merrifield 1998; Harris & Zaritsky 2004, 2009; Chandar et al. 2010a).

The interpretation is less straightforward for the Antennae galaxies, since they are too far away to determine their star formation history from observations. Furthermore, it is natural to wonder whether the interaction could trigger enough recent formation to explain the shape of $dN/d\tau$ without disruption. Fall et al. (2005) argued that the formation rate would vary by factors of a few on the orbital timescale ($\sim 10^8$ yr), too gradually to account for most of the decline in $dN/d\tau$ (see also Whitmore et al. 2007 and Fall et al. 2009). The results presented here support this suggestion. We have assembled the star formation histories in all the available N-body+hydrodynamical simulations of the Antennae. These are based on different numerical methods, different orbits, and different prescriptions for star formation and stellar feedback. The treatment of small-scale processes is still approximate at best, due to the low resolution in the simulations compared to molecular clouds and clumps in the real ISM. The SFRs differ greatly among the simulations, both in absolute level and in time dependence. Nevertheless, we find that they *all* vary slowly, by factors of only $1.3 - 2.5$ in the past 10^8 yr. When we combine the formation rates in the simulations with a power-law model for the survival fraction of clusters, $f_{\rm surv} \propto \tau^{\delta}$, we find good agreement with the observed age distribution over the range 10^6 yr $\lesssim \tau \lesssim 10^9$ yr for $-0.9 \lesssim \delta \lesssim -0.6$. The similarity between δ and γ indicates that $dN/d\tau$ is shaped mainly by the disruption of clusters rather than variations in their formation rate.

The only caveat to this conclusion stems from our assumption that the formation rates of clusters and stars are proportional to each other, i.e. $(dN/d\tau)_{\rm form} = c \cdot dN_*/d\tau$ with $c =$ constant (cf. Equation (6.2)). This is certainly true if most stars form in clusters, a hypothesis consistent with Hα observations of the Antennae (Fall et al. 2005). However, even if we were to abandon this assumption entirely, and allow c to vary arbitrarily with τ, a slightly modified version of the analysis presented above would then lead to the alternative result $c(\tau) \cdot f_{\rm surv}(\tau) \propto \tau^{\delta}$ with $-0.9 \lesssim \delta \lesssim -0.6$. We would then be left with the problem of explaining why the product $c \cdot f_{\rm surv}$ but not $f_{\rm surv}$ in the Antennae happens to be the same as $f_{\rm surv}$ alone in other galaxies. The simplest interpretation — the one advocated here — is that the formation rates of clusters and stars *do* track each other and that the survival fractions and hence the disruption histories *are* similar in different galaxies, including the Antennae.

Chapter 7

The Fate of the Antennae Galaxies – the Merger Remnant

What are the Antennae galaxies going to look like once they will have merged into one single object? In this Chapter, we will allow ourselves a quick glimpse into the (model) future. First, we investigate the properties of the dynamically relaxed merger remnant at an age $\tau_{\rm remnant} \approx 1\,{\rm Gyr}$ after the final coalescence of the main bodies in our fiducial Antennae model. We find that the Antennae remnant resulting from the major spiral-spiral merger represents a typical extra-light elliptical to very good approximation, showing a projected surface brightness profile that is well represented by a Sérsic function with index $n \sim 5$. This is expected from the current picture of elliptical galaxy formation for a gas-rich merger of two disk galaxies with comparable masses to the Antennae progenitor galaxies. Furthermore, we assess the evolution of the Antennae from the time of best match near their final merger, studied at length in the previous Chapters, to their future state, assuming star formation to be suppressed for remnant ages $\tau_{\rm remnant} > 1\,{\rm Gyr}$. For high present-day metallicities ($Z \gtrsim Z_{\odot}$), consistent with observed estimates in the Antennae, the remnant stellar population shows properties (e.g. mean age, color, and absolute magnitude) similar to local early-types if evolved to remnant ages $2.5\,{\rm Gyr} < \tau_{\rm remnant} < 3\,{\rm Gyr}$. This indicates that a plausible future remnant of an Antennae-like present-day galaxy merger may evolve into a normal present-day elliptical galaxy after additional $\sim 2.5-3\,{\rm Gyr}$ of secular evolution after the final merger of the galaxies, reddening even further at older ages.

7.1 The Role of Mergers for Elliptical Galaxy Formation

Elliptical galaxies are a homogeneous class of galaxies characterized by their roundish photometric shapes and old stellar populations. They generally consist of a dominant stellar bulge with only very little gas and a low level of star formation. Nowadays it is well established that elliptical galaxies exhibit a trend in their structural properties with increasing total magnitude. Bright ellipticals ($M_{\rm B} \lesssim -20.5$) are typically slowly rotating systems with boxy isophotes and shallow central surface brightness profiles ("cores"). Their low rotation velocities suggest that the observed flattening (with ellipticities $\epsilon \lesssim 0.3$) is due to anisotropic velocity dispersions rather than rotation. Fainter giant ellipticals ($-20.5 \lesssim M_{\rm B} \lesssim -18$), on the other hand, in general are oblate, nearly-isotropic systems, which are flattened by rotation. Their isophotal shapes generally show disky deviations from perfect ellipses and they have steep "cuspy" central surface brightness profiles (see e.g. Davies et al. 1983; Bender et al. 1989; Kormendy & Bender 1996; Lauer et al. 2005; Cappellari et al. 2007; Emsellem et al. 2007; Kormendy et al. 2009; Emsellem et al. 2011).

In their "merger hypothesis" Toomre & Toomre (1972) coined the idea that elliptical galaxies may form from the merger of two disk galaxies (Toomre 1977, see Chapter 2). Many numerical studies tested this hypothesis using binary merger simulations. First collisionless simulations were able to show that the remnants of equal-mass disk mergers broadly reproduce the principal structural properties of bright ellipticals (Toomre 1977; Negroponte & White 1983; Barnes 1988, 1992). The remnants generally represented slowly-rotating, anisotropic ellipsoids that follow a characteristic $\sim R^{1/4}$ surface density profile at large galactocentric radii. Naab & Burkert (2003) showed that simulations of unequal mass disk mergers (with ratios of 3:1 and 4:1) result in remnant properties more akin to intermediate mass ellipticals, i.e. they are nearly isotropic systems with predominantly disky isophotes, and supported by rotation.

Tidal perturbations can lead to dynamical instabilities that drive large gas fraction to the centers of interacting galaxies (Negroponte & White 1983; Noguchi 1988; Barnes & Hernquist 1996). When including additional star formation, numerical studies of gas-rich mergers report high central densities of the stellar remnants, similar to the steep "extra-light" cusps observed at the centers of faint giant elliptical galaxies (e.g. Mihos & Hernquist 1994). In general, including gas dissipation and the associated star formation results in merger remnants that are in better structural and kinematical agreement with disky, fast-rotating intermediate-mass ellipticals (e.g. Naab et al. 2006; Cox et al. 2006; Hopkins et al. 2009; Bois et al. 2011). In particular, the presence of gas favors rounder, more disky isophotes and leads to changes in the stellar kinematics of the remnants, e.g. a larger range of rotational velocities in the systems (e.g. Barnes & Hernquist 1996; Cox et al. 2006; Naab et al. 2006). Furthermore, remnants from wet mergers tend to show shapes of the stellar line-of-sight velocity distributions with

steep leading wings, consistent with the kinematics of observed intermediate ellipticals (Naab et al. 2006). This has led to the suggestion that the most massive elliptical galaxies in general form from dissipation-less (early-type) mergers, while intermediate-mass ellipticals are more likely the remnants of 'wet' binary disk mergers.

Nowadays, the Toomre merger hypothesis has to be taken in the broader picture of hierarchical structure formation in the universe, as described to very good precision by modern hierarchical theories like the favored ΛCDM model (e.g. Komatsu et al. 2011). Observations predict that an average elliptical galaxy-sized halo is expected to have experienced ~ 1 major merger since $z \sim 2-3$ (Bridge et al. 2007; Conselice et al. 2007, 2009), and, presently, about $\sim 5-10\%$ of all galaxies are interacting or in the process of merging (e.g. Lotz et al. 2008; Bridge et al. 2010; Lotz et al. 2011).

A popular approach to study the formation of elliptical galaxies is to use controlled experiments of isolated disk galaxy merger simulations. These allow to study the properties of a statistically large number of "mock" merger remnants and compare them with observational samples of elliptical galaxies. In this Chapter, however, we will use a complementary approach: we will use *one* bona-fide representation of a specific real system — the Antennae galaxies — and study whether the resulting merger remnant will evolve into a typical elliptical galaxy. The Antennae galaxies provide us with a prime example of a present-day spiral merger with substantial on-going star formation, and we expect them to be predecessors of typical local star-bursting ULIRGs. These are thought to be disk mergers with mass ratios of 1:1 to 3:1 having global properties in line with present-day ellipticals (Genzel et al. 2001; Dasyra et al. 2006a,b). Since we can be optimistic that the simulation closely resembles the Antennae galaxies at the present time, owing to the many positive tests carried out in Chapters 5 - 6, we want to assess the properties of a future Antennae remnant at later times, when the galaxies will have merged. Therefore, we use our fiducial simulation presented in Chapters 4 and 5, but evolve it further in time for about 1 Gyr past final coalescence (occurring at time $t \sim 1.3\,\mathrm{Gyr}$)[1]. This ensures that the remnant has relaxed to approximate dynamical equilibrium. We will report on the intrinsic structural and kinematic properties of the remnant at time $t = 2.3\,\mathrm{Gyr}$ in Section 7.2. Using simple stellar population synthesis models, we estimate the photometric properties of the remnant and fit the photometric profile with a Sérsic function in Section 7.3. Moreover, in this Section, we construct two-dimensional kinematic maps following the kinemetric methods introduced by Krajnović et al. (2008), which are commonly used in the data analysis of modern integral field spectrographs. Furthermore, we investigate the evolution of the remnant color and mean stellar age with time in Section 7.4. Finally, we conclude in Section 7.5.

[1]Note that, for the further analysis, we will identify the remnant to have age $\tau_{\mathrm{remnant}} = 0$ at the time of the final galaxy merger.

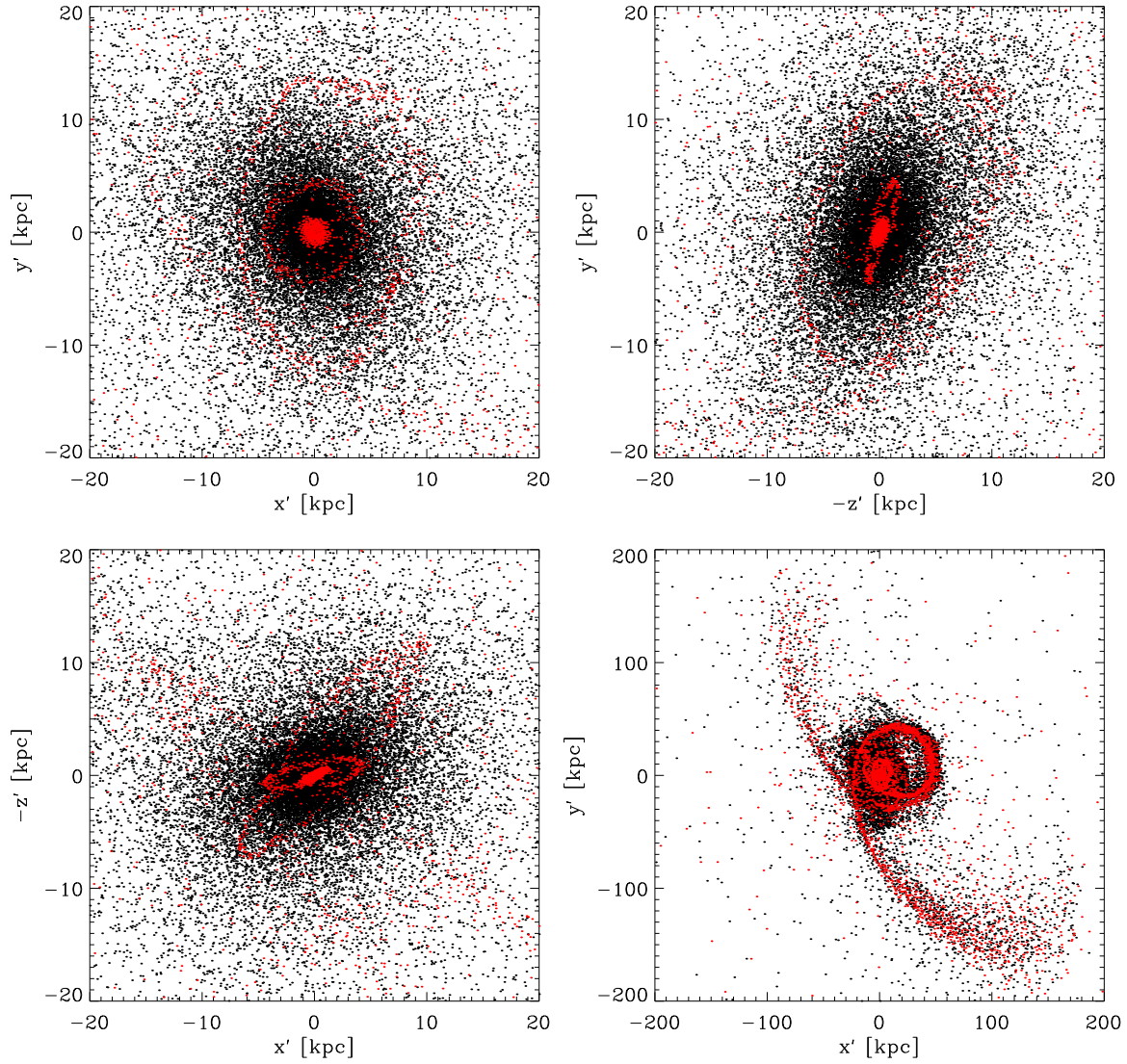

Figure 7.1: Spatial projections of the Antennae merger remnant for stellar (black) and gas (red) particles at a remnant age $\tau_{\rm remnant} = 1\,{\rm Gyr}$. We show three close-ups of the inner remnant structure (40 $\rm kpc$ across) in the plane-of-the-sky of the merger (X'Y', *upper left*), and two orthogonal projections (-Z'Y', *upper right* and X'(-Z'), *lower left*) edge-on to the plane-of-the-sky. A large-scale projection in the plane-of-the-sky (400 $\rm kpc$ across) is given in the lower right panel. For clarity, only every 40th stellar and every 15th gas particle is plotted. Note that the upper left and lower right panels correspond to how the simulated Antennae remnant would be observable on the sky in $\sim 1\,{\rm Gyr}$ from now.

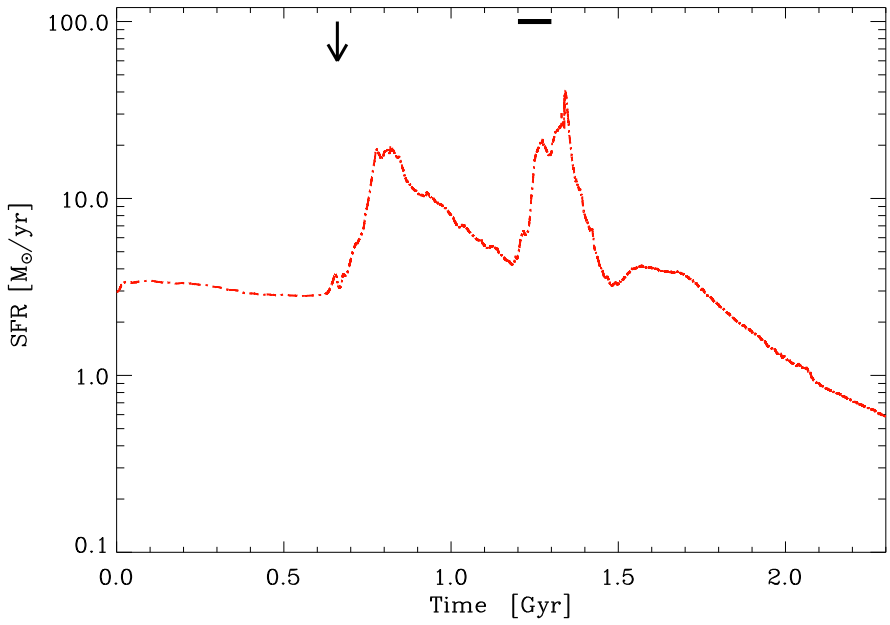

Figure 7.2: Star formation history of the fiducial Antennae simulation until a time $\sim 1\,\mathrm{Gyr}$ after the final merger of the progenitor galaxies. The arrow gives the time of first close encounter, while the bar indicates the time between second close encounter and final merger.

7.2 Intrinsic Structure and Kinematics of the Antennae Merger Remnant

We examine the properties of the Antennae remnant at a remnant age $\tau_{\mathrm{remnant}} = 1.0\,\mathrm{Gyr}$ after the final galaxy merger. At that time the virial coefficient ($\eta \equiv \frac{2E_{\mathrm{kin}}}{|E_{\mathrm{pot}}|}$) has converged to $\eta \sim 1.01$, as measured for all gravitationally bound particles of the system. This is close enough to dynamical equilibrium ($\eta_{\mathrm{equ}} \equiv 1$) such that we assume the system to be in virial equilibrium in the further analysis. The remnant galaxy appears as a rather flattened ellipsoid (see the upper panels and lower left panel in Figure 7.1). When looked at in the plane-of-the-sky projection of the merger (upper left panel), the remnant has a quite round projection. However, we determine intrinsic principal axis ratios of $b/a = 0.94$ and $c/a = 0.69$ for the major axis a, semi-major axis b, and minor axis c, respectively, measured at the stellar[2] spherical half-mass radius $r_{50,\mathrm{stellar}} = 7.34\,\mathrm{kpc}$. This corresponds to a triaxiality parameter $T \equiv \frac{a^2-b^2}{a^2-c^2} \approx 0.22$ at $r = r_{50,\mathrm{stellar}}$, indicating an intrinsically oblate system (see, e.g. Jesseit et al. 2005; van den Bosch et al. 2008). Going further inwards towards the center, this trend becomes even more pronounced with axis ratios $b/a = 0.98$ and $c/a = 0.77$, corresponding to $T = 0.10$ at $r = r_{50,\mathrm{stellar}}/4 \sim 1.8\,\mathrm{kpc}$. Albeit its recent major merger, the vast majority

[2]Note that here and in the following we denote with "stellar" all baryonic dissipation-less particles in the simulation, namely, the bulge, the pre-existing disk stars and the newly formed stars.

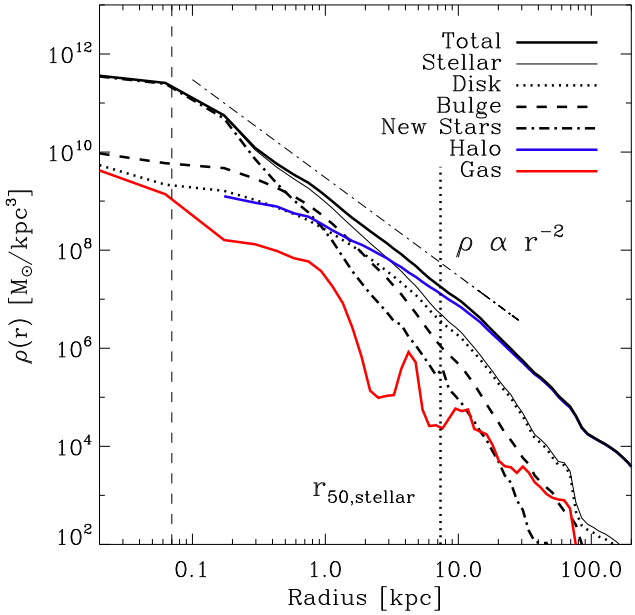

Figure 7.3: Spherical density profile of the stellar components — disk (dotted), bulge (dashed), and formed stars (dashed-dotted) — in the Antennae merger remnant at time $t = 2.3\,\mathrm{Gyr}$. This corresponds to a time $\sim 1\,\mathrm{Gyr}$ after final coalescence ($t \sim 1.3\,\mathrm{Gyr}$). The total stellar, dark matter and gas density profiles are given by the thick black line, the solid blue line, and the solid red line, respectively. The resolution limit (of two baryonic softening lengths) and the stellar half-mass radius are indicated by the dashed and dotted vertical lines.

($\sim 97.3\%$) of all particles is bound. The dense inner parts are surrounded by a ring of stars and gas with a projected diameter of $\sim 40\,\mathrm{kpc}$ that has been ejected during the second encounter, and, at larger radii, by the diffuse remnants of the tidal tails (lower right panel). In Figure 7.1, for clarity, only every 40th of all stellar particles and every 15th gas particle is plotted. Additionally, we have centered the remnant on the peak density in the system. While the inner regions of the stellar remnant are quite round and featureless (black particles in Figure 7.1), the gas (red particles) shows a number of peculiar features. In particular, there are two distinct loops of dense gas with projected diameters of $\sim 10\,\mathrm{kpc}$ and $\sim 20\,\mathrm{kpc}$ which encompass a small, compact gas disk in the center (upper row and lower left panel in Figure 7.1). The central gas disk and the inner ring happen to lie almost face-on in the plane-of-the-sky, and the two inner rings are made up almost entirely of gas which was flung out from the galaxy centers in the second close encounter (see Figure 7.3 below). Similar central gas disks and rings are found in earlier simulations of gas-rich mergers (see Barnes 2002; Naab et al. 2006) — with a highly irregular "disk" structure, in our case, which is more often seen in equal-mass mergers (Naab et al. 2006).

In these dense inner gaseous disk and rings there is still some on-going star formation

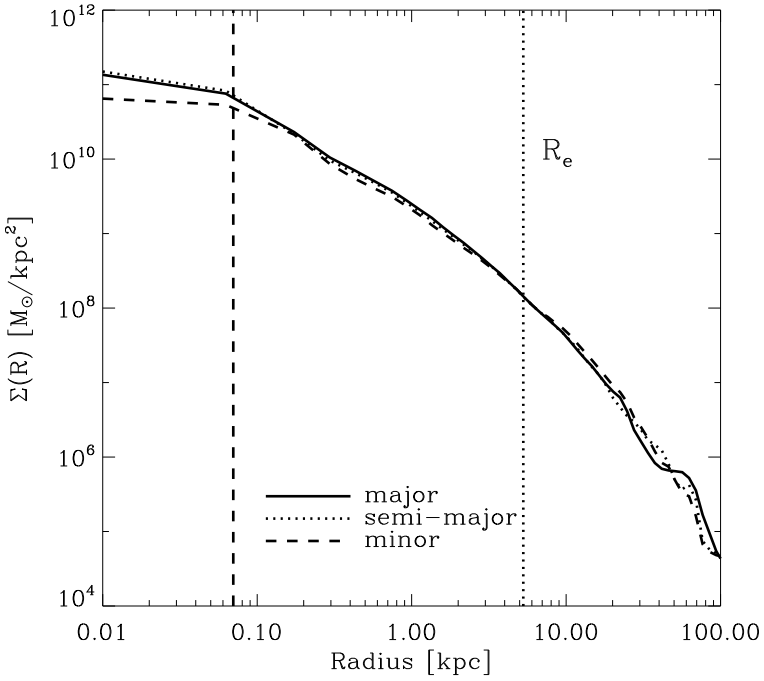

Figure 7.4: Projected surface density profiles for the stellar components in the Antennae merger remnant along the three principal axes: the major axis (solid line), the semi-major axis (dotted line), and the minor axis (dotted line). The resolution limit (of two baryonic softening lengths) and the mean effective radius of the three projections are indicated by the dashed and the dotted vertical lines.

in the remnant. We show the star formation history from the start of the simulation to the time when we analyze the merger remnant ($t = 2.3\,\mathrm{Gyr}$) in Figure 7.2. We see that the SFR drops quickly from a peak SFR of $\sim 41\,\mathrm{M_\odot\,yr^{-1}}$ shortly after the final merger ($t = 1.34\,\mathrm{Gyr}$) to $\sim 0.6\,\mathrm{M_\odot\,yr^{-1}}$ at $t = 2.3\,\mathrm{Gyr}$. This is due to the decreasing mass of dense gas in the remnant after the final merger that could fuel on-going star formation. The total gas mass at that time amounts to $M_\mathrm{g} = 1.6 \times 10^9\,\mathrm{M_\odot}$ within 30 kpc, which is about $\sim 40\%$ of the total mass in gas remaining in the simulation. Another $\sim 30\%$ reside in the larger shell-like feature surrounding the remnant at a distance $\sim 40\,\mathrm{kpc}$, and the rest (another 30%) is in the tidal tails. We find a stellar remnant mass of $M_\star \sim 8.9 \times 10^{10}\,\mathrm{M_\odot}$, defined within the inner 30 kpc, which is about $\sim 85\%$ of the total stellar mass in the system.

Figure 7.3 shows the spherical density profile of the remnant for the progenitor disk (dotted line), the bulge (dashed line), and the newly formed stars (dashed-dotted line). The profile of all three stellar components combined is indicated by the thin solid line. The remnant density has risen by a factor of ~ 10 inside $\sim 1\,\mathrm{kpc}$ with respect to the combined initial density profiles of the two progenitor spirals at the start of the

simulations (not shown here). This evolution is mainly driven by the accumulation of newly formed stars (dashed-dotted line) that formed mainly in the nuclear starbursts associated with the first encounter and the final merger. The stellar density starts to decline smoothly at radii greater than the resolution limit (vertical dashed line in Figure 7.3), which we define as two times the baryonic softening length, $\epsilon_{\rm bary} = 35$ pc. At a galactocentric radius $r \sim 70\,$kpc, a density enhancement from the outer ring is imprinted in the profile. The dark matter halo (blue solid line) dominates the density profile for radii $r \gtrsim 0.5 \cdot r_{50,\rm stellar}$. On the other hand, the gas component (red solid line) is concentrated towards the center of the remnant such that the density drops by a factor of ~ 8 from the resolution limit ($r \approx 70\,$pc) to $r \sim 0.2\,$kpc. The inner gas loops, again, reveal themselves as marked density jumps (of the order of ~ 1 dex) at $r \sim 4\,$kpc and $r \sim 10\,$kpc. Note that there are no corresponding features to these jumps in the stellar and dark matter density profiles, reflecting the fact that the inner loops are made up almost entirely of gas.

Strong lensing studies suggest that the total density profiles of early-type galaxies are close to isothermal, showing power-law profiles $\rho \propto r^{-\gamma'}$ with $\gamma' \sim 2$. A recent compilation of 58 SLACS early-type galaxies obtains density profiles with a mean slope of $\langle\gamma'\rangle \simeq 2.085 \pm 0.1$ and an intrinsic scatter $\sigma_{\gamma'} \lesssim 0.2$ (Koopmans et al. 2009). In fact, the Antennae remnant shows a total density profile (thick solid line in Figure 7.3) close to an isothermal profile with slope $\gamma' = 2$ (indicated by the dot-dashed straight line), in very good agreement with the observed estimates in the SLACS early-types.

The corresponding projected surface density profile of the merger remnant along the directions of the major axis (solid), semi-major axis (dotted), and minor axis (dashed) is presented in Figure 7.4. The surface density profiles are almost identical along the three principal axes for projected radii larger than $R \gtrsim 0.3\,$kpc, such that their mean effective radii are very similar, with a mean of $\bar{R}_{\rm e} = 5.28\,$kpc. Hence, the effective radii have decreased by factors of ~ 2 and ~ 1.3 with respect to the values $R_{\rm e}^{4038} = 10.5\,$kpc and $R_{\rm e}^{4039} = 6.9\,$kpc of the effective disk radii in the progenitor galaxies, respectively. Towards the center we see indications that the surface density profile projected along the minor axis levels off with respect to the other two projections, as we would expect for an oblate system. However, this is mostly seen significantly below the resolution limit (dashed vertical line) so that we cannot draw a robust conclusion here. Over the radial range $50\,{\rm kpc} < R < 100\,{\rm kpc}$ (depending on the projection) we, again, see some density enhancements in the surface density profiles, similar to what we found in Figure 7.3.

Next, we will have a look at the intrinsic kinematical structure of the different stellar components of the merger remnant. As we will see, the three components, while deeply mixed together during the final merging, show quite different kinematical signatures in the central regions of the merger remnant. This can be seen from the intrinsic velocity dispersion profiles for the different components in Figure 7.5, i.e. the

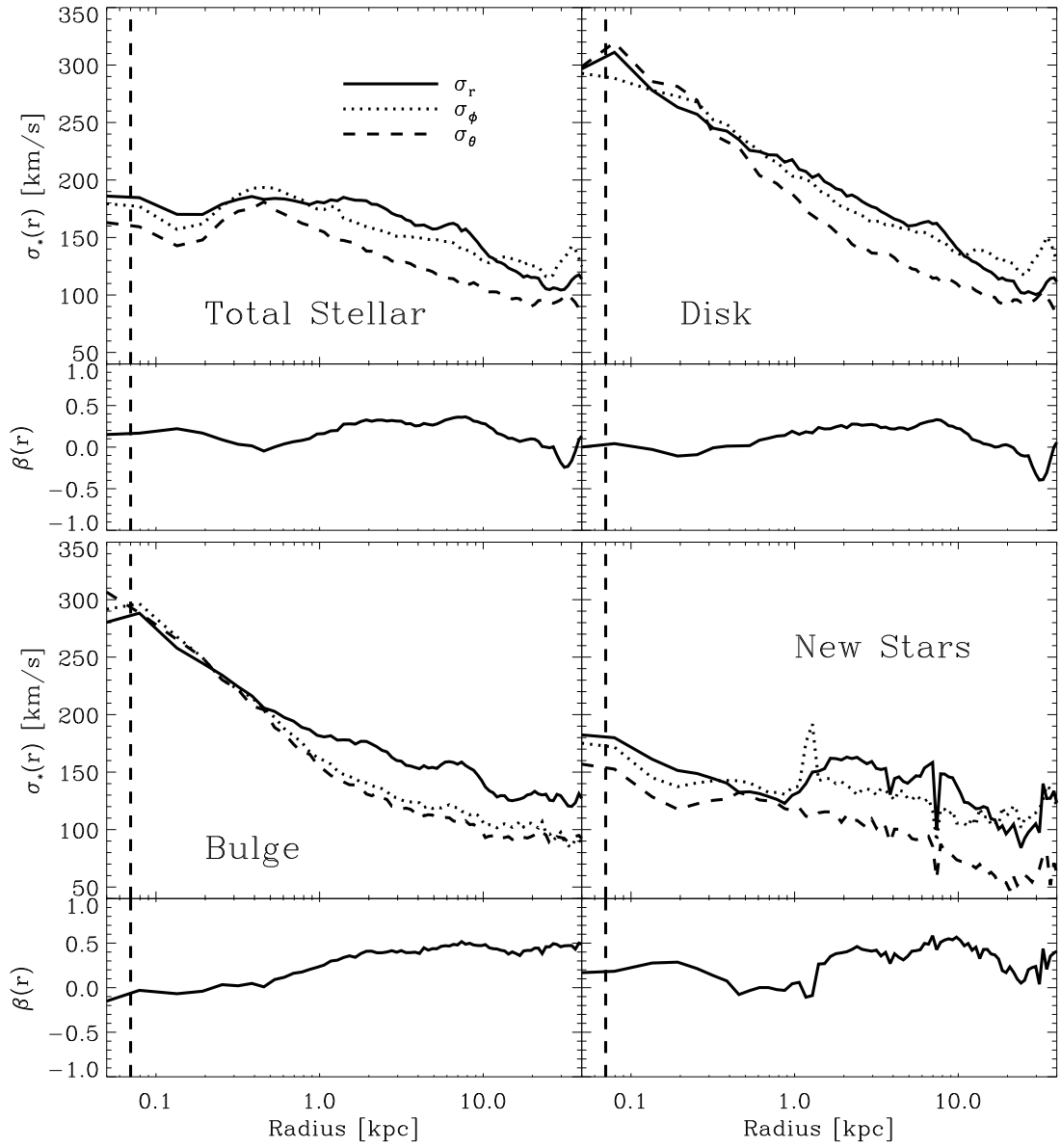

Figure 7.5: Velocity dispersion profiles of the stellar components in the Antennae merger remnant. The total velocity dispersion of all stellar particles *(upper left panel)* is shown together with the profiles for the disk particles *(upper right panel)*, bulge particles *(lower left panel)*, and newly formed star particles *(lower right panel)*, separately. The radial velocity dispersion σ_r and the two tangential velocity dispersions, σ_ϕ and σ_θ, are given by the solid, dotted, and dashed curves, respectively. The lower panels of each row present the corresponding radial profiles of the anisotropy parameter β from the velocity dispersion profiles in the upper panels. The resolution limit (of two baryonic softening lengths) is indicated by the dashed vertical line.

progenitor disk (upper right panel), the bulge (lower left panel), and the formed stars (lower right panel). In addition, in the lower panels of each row in Figure 7.5, we plot the anisotropy parameter $\beta(r)$, which describes the degree of radial anisotropy of the velocity distribution at radius r (see Binney & Tremaine 2008, Chapter 4) according to

$$\beta \equiv 1 - \frac{\sigma_\phi^2 + \sigma_\theta^2}{2\,\sigma_r^2}. \tag{7.1}$$

Hence, β tends to 1 for purely radial orbits, equals zero for a strictly isotropic system, and diverges to $-\infty$ for tangentially biased systems, e.g. in the case of non-zero rotation.

Both the progenitor disk and bulge components (upper right and lower left panels in Figure 7.5) appear as rather isotropic systems at the very center ($r < 1\,\mathrm{kpc}$), with peak velocity dispersion profiles of $\sim 300\,\mathrm{km\,s^{-1}}$. The profiles decline to $\sim 100 - 150\,\mathrm{km\,s^{-1}}$ at $r \sim 10\,\mathrm{kpc}$. Further out ($1\,\mathrm{kpc} < r < 10\,\mathrm{kpc}$), both components become more radially biased ($\beta(r) > 0$). The newly formed stars exhibit a strikingly different kinematic profile to the other two components (lower right panel in Figure 7.5). The dispersions are much flatter and do not exhibit a similarly dramatic rise in their central dispersions. They stay well below $200\,\mathrm{km\,s^{-1}}$ at all radii, and the dispersions become comparable to the ones of the progenitor bulge and disk components at radii larger than $\sim$ a few kpc. The formed stars also tend to be slightly radially biased, with $0 \lesssim \beta(r) \lesssim 0.5$ at all radii. The velocity dispersions of all stellar particles combined is shown in the upper left panel of Figure 7.5. Owing to the much higher stellar (number) density of the new star particles inside the central $\sim$ kpc (see Figure 7.3), the overall velocity dispersions for both the radial and the tangential directions stay at a comparably low level $\sigma_i \lesssim 190\,\mathrm{km\,s^{-1}}$, with $i = \{\mathrm{r}, \theta, \phi\}$, despite the high central dispersions of the bulge and the disk components. On the other hand, at radii $r \gtrsim 2\,\mathrm{kpc}$, the disk component dominates the stellar density and, hence, the stellar velocity dispersion profiles (see upper right panel in Figure 7.5). This is also reflected in the profile of the anisotropy parameter, which shows a very similar profile to the progenitor disk component at radii $r \gtrsim 2\,\mathrm{kpc}$, but becomes slightly radially biased ($0 \lesssim \beta \lesssim 0.2$) for $r \lesssim 1\,\mathrm{kpc}$ due to the dominant contribution of newly formed stars.

7.3 Observable Properties of the Antennae Merger Remnant

It was one of the fundamental early observations for elliptical galaxies that their projected surface brightness profiles are, in general, very well described by a de Vaucouleurs' law with characteristic $I \propto R^{1/4}$ profile over a large range of projected radii from the center R (de Vaucouleurs 1948). However, more recent work has shown that

the central slope of the light profiles seems to be a very important parameter because it correlates to other observed properties of elliptical galaxies, such as the effective radius R_e, the total luminosity L, and the stellar mass $M_\star$ (Caon et al. 1993; Nipoti et al. 2003; Naab & Trujillo 2006; Kormendy et al. 2009). Therefore, often a Sérsic $r^{1/n}$ (Sersic 1968) profile is used to describe the surface brightness profiles of elliptical galaxies. We will use this profile in order to fit the surface brightness of the simulated Antennae merger remnant. The Sérsic formula can be written as

$$I(R) = I_e \cdot 10^{-b_n\left[\left(\frac{R}{R_e}\right)^{1/n}-1\right]}, \tag{7.2}$$

where I_e is half of the total surface brightness. The effective radius R_e determines the projected distance from the galaxy center which encloses half of the total surface brightness, and n is the so-called Sérsic index that determines the logarithmic slope of the profile. The larger the value of n, the more centrally concentrated the profile is, and the steeper (shallower) the slope at small (large) radii. Cored galaxies generally show Sérsic indices with $n > 4$, while cuspy ("extra-light") galaxies have values of $n \simeq 3 \pm 1$ (Kormendy et al. 2009). These three free parameters together determine the exact shape of the profile, while the additional factor b_n depends only on n and is chosen such as to assure that the effective radius R_e encloses half of the total luminosity. For the observed range of Sérsic indices, this factor can be very well approximated by the relation $b_n = 0.868\,n - 0.142$ (Caon et al. 1993). Note that the Sérsic profile is a generalization of the de Vaucouleurs' law in the sense that Equation 7.2 reduces to a de Vaucouleurs' $r^{1/4}$ profile in the case of $n = 4$.

In order to compare the properties of the simulated Antennae remnant to observations of local elliptical galaxies (e.g. Trujillo et al. 2004; Kormendy et al. 2009) we proceed as follows. First, we obtain tabulated magnitudes (normalized to a mass of $1\,\mathrm{M}_\odot$) for a grid of ages and metallicities in a number of photometric bands using Bruzual & Charlot (2003) simple stellar population synthesis models. Hereby, we choose a Salpeter IMF (Salpeter 1955) with stellar masses between $0.1\,\mathrm{M}_\odot$ and $100\,\mathrm{M}_\odot$. For the actual comparison with the data, we will use the V-band and B-band luminosities below, and, for simplicity, we assume $Z = 0.02$ for all stellar particles and stellar ages of 10 Gyr and 5 Gyr for all bulge and disk particles, respectively, at the time of best match ($t = 1.247\,\mathrm{Gyr}$). The stellar ages of the newly formed stars are directly obtained from the simulations. Then we assign to every star particle of mass $m_\star$ a luminosity $L_\star^{\mathrm{B,V}}$ according to

$$L_\star^{\mathrm{B,V}} = m_\star \cdot 10^{-M_\star^{\mathrm{B,V}}/2.5}, \tag{7.3}$$

where $M_\star^{\mathrm{B,V}}$ is the absolute magnitude of a star in the given band at a distance of 10 pc. This yields total B- and V-band magnitudes of $M_\mathrm{B} = -20.4$ and $M_\mathrm{V} = -21.2$ for the Antennae remnant.

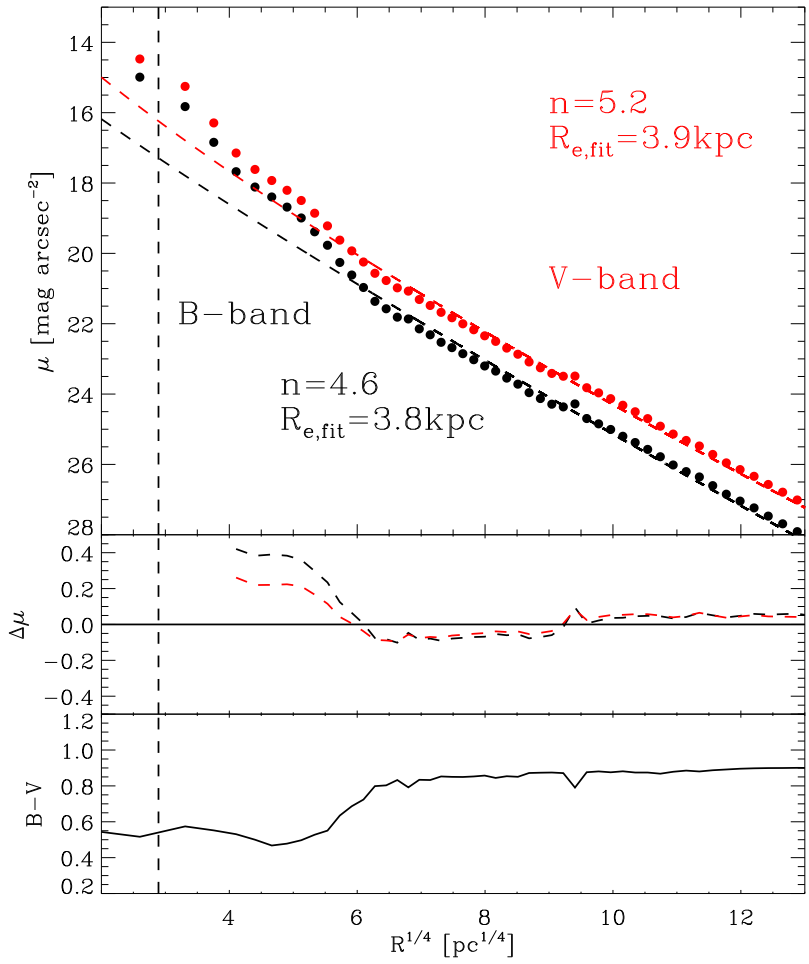

Figure 7.6: *Upper panel:* Surface brightness profiles projected along the major axis of the Antennae merger remnant. The red and black dots represent the binned simulated surface brightness in the V-band (red color) and the B-band (black color), respectively. Sérsic fits in both bands are shown as the dashed colored lines, together with the obtained fit parameters. *Middle panel:* Residuals between the fitted and the observed profiles for the V-band (red dashed line) and the B-band (black dashed line). *Lower panel:* $B-V$ color profile from the V- and B-band surface brightness profiles in the upper panel. The resolution limit (of two baryonic softening lengths) is indicated by the dashed vertical line.

As a next step, we calculate the projected surface brightness profile of all stellar particles along the line-of-sight for the relaxed merger remnant in bins of the projected radius R for both the B- and V-band (note that we drop the superscripts in the following),

$$\mu(R) = -2.5 \cdot \log L(R) + c_0, \tag{7.4}$$

with zeropoint $c_0 = 21.5721$. Here, $L(R)$ is the total stellar luminosity in each bin in the given band. Finally, we fit a Sérsic function to the simulated surface brightness profile of the remnant in both B- and V-band, where we use the logarithmic form of Equation 7.2,

$$\mu(R) = -2.5 \log I(R) = \mu_e + c_n \left[\left(\frac{R}{R_e} \right)^{1/n} - 1 \right], \tag{7.5}$$

with $c_n = 2.5 \cdot b_n$ and $\mu_e = -2.5 \log I_e$.

In Figure 7.6 we present the resulting Sérsic fits for the simulated surface brightness profiles in the V-band (red) and the B-band (black). The profiles have a strict power-law shape over most of the plotted radial range ($1\,\mathrm{kpc} \lesssim R \lesssim 28\,\mathrm{kpc}$), with an almost constant offset of ~ 1 mag. But within $R \lesssim 1\,\mathrm{kpc}$, they show a significant amount of extra-light which stems from the central starburst after the final merger. Therefore, we have chosen a fitting range such that we obtain a good fit for the main body of the merger remnant. This means that we fit for radii from $R_e/4 \gtrsim 1.2\,\mathrm{kpc}$ out to $\lesssim 8 \cdot R_e$, for both the B- and the V-band. This choice results in Sérsic fits very close to the simulated profile with residuals $\Delta\mu$ that are typically well below 0.1 mag arcsec^{-2} (bottom panel of Figure 7.6), except for the central regions, where a luminous stellar cusp has formed. We obtain fit parameters for the Sérsic index of $n_\mathrm{V} = 5.2$ and $n_\mathrm{B} = 4.6$, together with $R^\mathrm{V}_\mathrm{e,fit} = 3.9\,\mathrm{kpc}$ and $R^\mathrm{B}_\mathrm{e,fit} = 3.8\,\mathrm{kpc}$ for the V-band and the B-band, respectively (see Figure 7.6). This is close to a de Vaucouleurs $R^{1/4}$-profile and consistent with the upper end of the observed Sérsic indices of extra-light galaxies (Kormendy et al. 2009; Trujillo et al. 2004). The effective radii we obtain from our fits lie very well inside the range of observed values in the V-band and B-band, $R_e \sim 3.3 - 5.4\,\mathrm{kpc}$, for massive extra-light ellipticals (Trujillo et al. 2004; Kormendy et al. 2009).

The $B - V$ colors show an overall shallow profile with slope $\Delta(\mathrm{B\text{-}V})/\Delta \log(R) = 0.07$ mag per dex in radius within $1.5\,\mathrm{kpc} < R < 28.5\,\mathrm{kpc}$. In the central regions ($R \lesssim 1.5\,\mathrm{kpc}$), where the compact gas disk is located and the newly formed stars dominate the total density (Figure 7.3), the remnant is substantially bluer with a drop in the $B - V$ color of ~ 0.25 dex. Generally it has been found that massive early-type galaxies in general tend to have redder colors at their centers, becoming bluer toward their outer parts, i.e. they show color gradients that have small negative logarithmic slopes with the exact value depending on the bands used to derive the colors (e.g. Franx

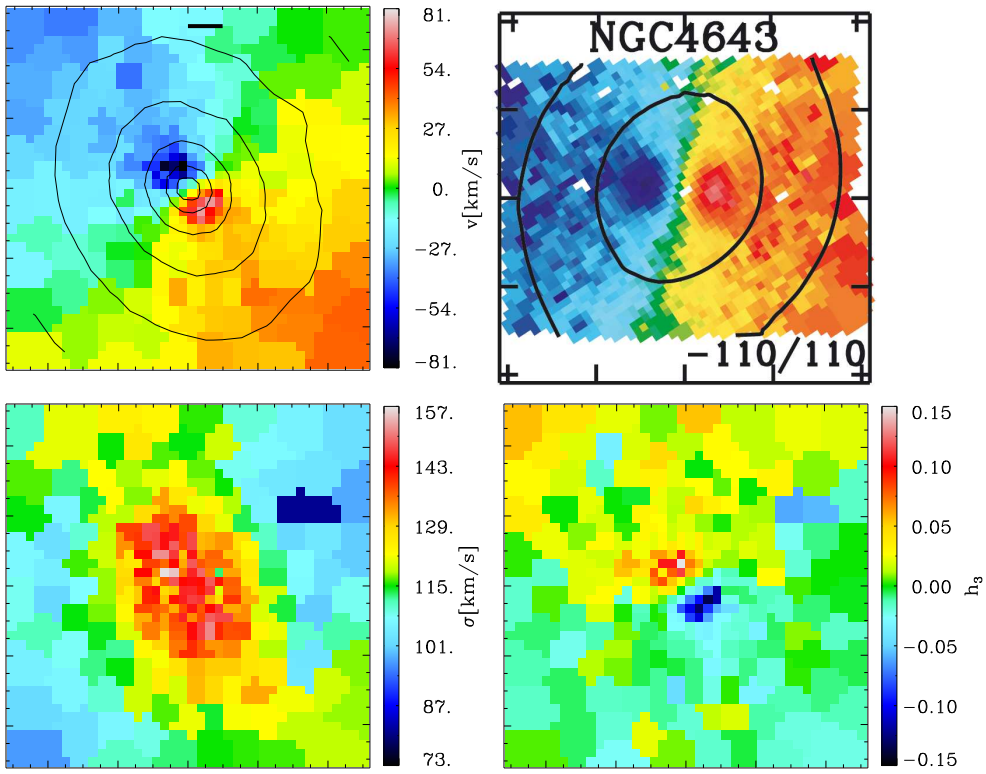

Figure 7.7: 2D stellar kinematics of the merger remnant. The vantage point is chosen as for the best match of the Antennae. We present the line-of-sight velocity distribution (LOSVD; *upper left panel*), the velocity dispersion *(lower left panel)*, together with the higher moment h_3 *(lower right panel)*. The field-of-view corresponds to the projection in the plane-of-the-sky inside the spherical effective radius. The small bar indicates a projected distance of 1 kpc. For comparison, we show the best look-alike to the Antennae remnant, NGC 4643, from the ATLAS^{3D} survey (*upper right panel*).

et al. 1989; Peletier et al. 1990; Tortora et al. 2010; Gonzalez-Perez et al. 2011; den Brok et al. 2011). However, the scatter tends to be large such there, indeed, exist many examples of early-types with flat or positive gradients (see e.g. Bender & Moellenhoff 1987; Gonzalez-Perez et al. 2011). In the case of the Antennae remnant, the mean stellar age is lowest in the galactic center, where it experienced the starburst during the final merger, only about 1 Gyr ago. We will further discuss the evolution of the remnant color and absolute magnitude with age in Section 7.4.

Figure 7.7 shows kinematic maps constructed using the kinemetric methods presented in Krajnović et al. (2008). These include two-dimensional maps of several low-order Gauss-Hermite coefficients, e.g. the projected stellar densities (contours in the upper left panel), the stellar line-of-sight velocity distribution (LOSVD; upper left panel), the velocity dispersion (h_2; lower left panel), and the h_3 coefficient (lower right panel), which is a measure for asymmetric deviations from a Gaussian LOSVD. All

maps are Voronoi binned (Cappellari & Copin 2003) and the field-of-view is chosen such that the system is imaged out to a spherical effective radius, $r_{\rm e} = 5.2\,{\rm kpc}$ (which we take as the spherical half mass radius with a cut-off at 30 kpc). Furthermore, we adopt the same line-of-sight as in our best match to the Antennae, i.e. we "observe" the system as it would be seen in the plane-of-the-sky. The projected stellar density profile (zeroth moment) shows regular iso-density contours that appear quite round in accord with a small ellipticity parameter $\epsilon \equiv 1 - b/a = 0.04$ in this projection. We also determine the $\lambda_{\rm R}$-parameter, which is a luminosity-weighted measure for the projected angular momentum per unit mass (Emsellem et al. 2007), defined as

$$\lambda_{\rm R} \;=\; \frac{\langle R\,|V|\rangle}{\langle R\,\sqrt{V^2+\sigma^2}\rangle}, \tag{7.6}$$

with the brackets being luminosity averages. It is commonly used as an observational discriminant to divide fast ($\lambda_{\rm R} > 0.1$) and slowly ($\lambda_{\rm R} < 0.1$) rotating elliptical galaxies (Emsellem et al. 2007; Cappellari et al. 2007). In addition, binary merger simulation have confirmed that this parameter is a robust proxy for the intrinsic angular momentum content of elliptical merger remnants (Jesseit et al. 2009). This implies that, with $\lambda_{\rm R} \sim 0.184$ measured at the *projected* effective radius, $R_{\rm e} = 5.91\,{\rm kpc}$, the Antennae remnant, as seen in the plane-of-the-sky, would be classified as a fast-rotating elliptical. This is also consistent with the fact that the stellar remnant shows significant rotation, with the principal kinematical axis ($\rm PA_{kin}$) inclined by $\sim 21^\circ$ to the photometric major axis ($\rm PA_{phot}$, see upper left panel of Figure 7.7). The line-of-sight velocity has a spread of about $\pm 75\,{\rm km\,s^{-1}}$ in the very center ($R \lesssim 1.5\,{\rm kpc}$), revealing the rotating core of the galaxy. This is also reflected in the next higher uneven moment, h_3, that exhibits a strong anti-correlation to the LOSVD within the inner $\sim 1.5\,{\rm kpc}$ (lower right panel). This is usually taken as a sign for significant rotation (Bender et al. 1994; Krajnović et al. 2008, 2011). The velocity dispersion shows a characteristic peak at the center with $\sigma \gtrsim 150\,{\rm km\,s^{-1}}$, leveling off to $\sigma \lesssim 120\,{\rm km\,s^{-1}}$ for $r \gtrsim 2\,{\rm kpc}$. The values of h_3 are close to zero everywhere, except at the center, indicating that the LOSVD is generally close to Gaussian.

For comparison, we show the observed LOSVD map of NGC 4643 from the ATLAS$^{\rm 3D}$ survey, which is volume-limited sample of 260 nearby early-type galaxies (upper right panel of Figure 7.7; Cappellari et al. 2011; Krajnović et al. 2011). This galaxy is the best, among a number of further good kinematic look-alikes to the Antennae remnant in the survey. Both, NGC 4643 and the Antennae remnant, are clearly classified as regular rotators (RR), showing distinct maxima in their central velocity profiles, together with another radially aligned maximum following an intermediate decrease in the velocities. These features place them in group "e" of the ATLAS$^{\rm 3D}$ classification scheme (Krajnović et al. 2011). Both have low ellipticities, where $\epsilon_{\rm NGC4643} = 0.12 \pm 0.15$, which is also reflected by their round isophotes. The kinematic misalignment is slightly larger for the Antennae ($\Psi \sim 21^\circ$) than for NGC 4643 ($\Psi_{\rm NGC4643} = 9.1^\circ$), and NGC 4643 shows a larger velocity range ($\pm 110\,{\rm km\,s^{-1}}$; see Figure 7.7). Discrepancies lie in their

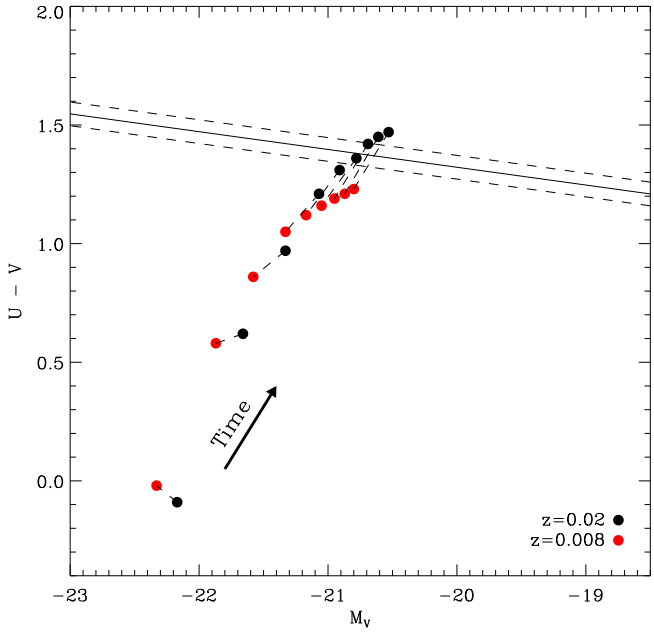

Figure 7.8: $U-V$ color vs. absolute magnitude M_V of the stellar population for different ages of the Antennae merger remnant with metallicities $Z = 0.02$ (black) and $Z = 0.008$ (red). The lower left dots correspond to the time of final merger of the progenitor galaxies. Each subsequent pair of dots to the right corresponds to a remnant that have aged further by $0.5\,\mathrm{Gyr}$. Remnants with $Z = 0.02$ are consistent with the observed color-magnitude (CM) relation (McIntosh et al. 2005) for ages between $\sim 2.5 - 3\,\mathrm{Gyr}$, while remnants with lower metallicity ($Z = 0.008$) would not evolve onto the observed CM relation for $\tau_{\mathrm{remnant}} \lesssim 4\,\mathrm{Gyr}$. The direction of increasing time is indicated by the black arrow.

absolute K-magnitudes and effective radii, where NGC 4643 is brighter by ~ 1 mag and much more compact with $R_{\mathrm{e,NGC4643}} = 1.92\,\mathrm{kpc}$ than the Antennae remnant with $R_{\mathrm{e}} = 5.91\,\mathrm{kpc}$.

7.4 Time Evolution of the Remnant Properties

In Figure 7.8 we present the time evolution of the Antennae remnant properties in the $U-V$ vs. M_V color-magnitude (CM) plane, where we assume stellar populations with slightly super-solar (Z = 0.02, black dots) and sub-solar (Z = 0.008, red dots) metallicites. Both values are in reasonable agreement with metallicity estimates from young star clusters in the Antennae (Bastian et al. 2009; Brandl et al. 2009). The leftmost pair of dots in each model corresponds to the CM properties of the remnant at the time of final merging of the progenitor spirals. With each subsequent pair the remnant has aged by $\sim 0.5\,\mathrm{Gyr}$. For simplicity, for ages $\tau_{\mathrm{remnant}} > 1\,\mathrm{Gyr}$ we extrap-

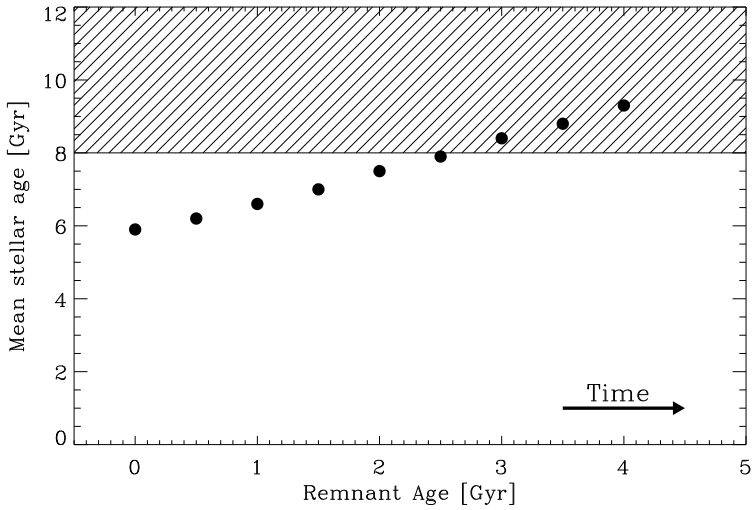

Figure 7.9: Mean age of the remnant stellar population vs. remnant age, where the time of the final merger corresponds to $\tau_{\rm remnant} = 0$. The shaded area represents mean stellar ages consistent with the stellar populations of present-day elliptical galaxies, and the arrow in the lower right indicates the direction of increasing time.

olate the remnant properties in time, assuming no significant further star formation after that time consistent with the rapidly dropping SFR after the peak following the final collision and merger (see Figure 7.2). Additionally, we indicate the observed CM relation (McIntosh et al. 2005) by the solid line, together with an intrinsic scatter of $\sigma \pm 0.5$ mag (dashed lines). As expected, owing to the peak star formation activity induced by the final merger, the remnant is much too blue to resemble a typical elliptical present-day galaxy in both models. With increasing age the stellar populations start to fade and redden, evolving towards the observed relation. For the higher-metallicity model, the stellar properties of the remnant fall right within the observed relation for ages $2.5\,{\rm Gyr} < \tau_{\rm remnant} < 3\,{\rm Gyr}$, resembling an elliptical galaxy with absolute V-band magnitude $M_V \sim -20.7$ mag. At later ages the remnant becomes even redder than observed present-day ellipticals due to the increasing mean age of the stellar population. In the lower metallicity model, we find that the remnant also becomes redder and evolves to fainter M_V magnitudes with increasing age, but stays well below the observed CM relation even for ages $\tau_{\rm remnant} \lesssim 4\,{\rm Gyr}$.

In Figure 7.9, we show the evolution of the mean stellar age of the merger remnant population with time. In fact, the remnant is already quite old when it forms, with $\langle \tau_\star \rangle = 5.9\,{\rm Gyr}$. This is due to a significant contribution of the old, massive bulges in our models. For remnant ages $\tau_{\rm remnant} \gtrsim 2.5\,{\rm Gyr}$, we find the merger remnant to be consistent with the typical mean stellar ages in elliptical galaxies ($\langle \tau_\star^{\rm elliptical} \rangle \gtrsim 8\,{\rm Gyr}$; shown by the dashed region in Figure 7.9). This agrees well with the analysis of Figure 7.8, provided the metallicity of the progenitor galaxies is high ($Z \gtrsim Z_\odot$). Assum-

ing that the photometric and kinematic properties of the dynamically relaxed merger remnant remain approximately constant in time, we conclude that, within our model, the Antennae galaxies may resemble an elliptical galaxy with properties of typical intermediate-mass present-day early-types at remnant ages $2.5\,\mathrm{Gyr} < \tau_{\mathrm{remnant}} < 3\,\mathrm{Gyr}$ after the time of the final merger, reddening even further at older ages.

7.5 Conclusions

In this Chapter, we have addressed the question of whether a present-day merger of two gas-rich spiral galaxies, represented by our bona-fide model of the Antennae galaxies, will evolve into a normal elliptical galaxy. This is not clear a priori since there still remain conflicting issues when comparing the stellar populations of spiral and elliptical galaxies, indicating that mergers of present-day spiral galaxies are not fully consistent with a number of properties of elliptical galaxies, such as their metal content, mean stellar ages, total absolute magnitudes and colors (see, e.g. Naab & Ostriker 2009). While we cannot assess the first issue (metal content) in our present numerical model, we can predict how other properties of the remnant will evolve with time under (simple) assumptions for the metallicities and the ages of the progenitor galaxies.

We have analyzed the virialized remnant properties from our fiducial Antennae model (see Chapter 4 and Chapter 5) at a remnant age $\tau_{\mathrm{remnant}} \sim 1\,\mathrm{Gyr}$ after the final merger. We find that the remnant photometric and kinematic properties are in good agreement with the ones in observed intermediate-mass elliptical galaxies. This confirms results of previous merger simulations (see Section 7.1). In particular, the remnant is an intrinsically oblate system with a nearly isothermal spherical density profile and a rotating stellar core. Using stellar population models, we find that the projected surface brightness profile is well fitted by a Sérsic function with Sérsic index $n \sim 5$. Owing to gas dissipation and star formation at the center in the final stages of the merger, the remnant has a significant amount of "extra-light" in its core ($R \lesssim 1.2\,\mathrm{kpc}$).

Evidently, the colors of the remnant at an age $\tau_{\mathrm{remnant}} = 1.0\,\mathrm{Gyr}$ are far too blue to represent a typical present-day elliptical. Therefore, we investigate the evolution of the stellar population of the remnant with time up to remnant ages $\tau_{\mathrm{remnant}} = 4\,\mathrm{Gyr}$. Assuming no further star formation for remnant ages $\tau_{\mathrm{remnant}} > 1.0\,\mathrm{Gyr}$, we find that an Antennae-like disk merger may add to a population of (future) elliptical galaxies with location in the CM diagram and mean stellar ages in good agreement with the population of present-day intermediate-mass ellipticals within the next $2.5 - 3\,\mathrm{Gyr}$, reddening even further at older ages. This, however, is only true provided that the merger remnant is sufficiently metal-rich, with $Z \gtrsim 0.02$.

Chapter 8

Conclusions and Outlook

8.1 Conclusions

Within this Thesis, we have performed the most detailed numerical study of the Antennae galaxies to date, using high-resolution simulations including radiative cooling, star formation and stellar feedback. Our goal is to improve the theoretical understanding of the Antennae galaxies. To achieve this, in a first step, we constrained suitable initial conditions (orbit geometry, disk orientations, initial disk galaxy models, etc.) in an extended parameter survey (Chapter 4). It is found that the Antennae are best described by an equal-mass merger on a mildly elliptical orbit and highly inclined disks with respect to the orbital plane. The progenitor galaxies are modeled as local early-type spirals of total mass $M \sim 5 \times 10^{11}\,\mathrm{M}_{\odot}$ with a typical disk gas mass fraction $f_g = 20\%$, a bulge-to-disk ratio $B/D = 0.4$, and a baryonic fraction $f_{\mathrm{bary}} = 0.1$. The two model galaxies only differ in their relative specific angular momenta, with $\lambda_{4038} = 0.10$ and $\lambda_{4039} = 0.07$. The line-of-sight towards the system actually lies very close, almost "edge-on", to the orbital plane of the merger. For further reference, all relevant parameters of the new fiducial Antennae model are listed in Table 4.2. In summary, the model galaxies are fairly consistent both with direct observation constraints from the Antennae and with predictions from current ΛCDM structure formation theory. This is a significant improvement with respect to previous modeling efforts. In order to reproduce the long tidal tails of the Antennae, however, our progenitor disks are necessarily biased towards models that fulfill this criterion.

Using the new best-matching galaxy models and orbit geometry, we were able to simulate the Antennae in unprecedentedly high resolution (Chapter 5). These simulations constitute the first numerical models that successfully match both the morphology and kinematics of the Antennae galaxies, as traced by high-resolution HI maps (Hibbard et al. 2001), on large (i.e. the tidal tails) and small scales (e.g. the kinematics and morphology of the main bodies). Moreover, in contrast to previous work, our proposed model reproduces the spatial distribution of young star clusters and the current

SFR in good agreement with recent observations (Klaas et al. 2010; Brandl et al. 2005; Whitmore et al. 2010). To disentangle the effects of stellar feedback on the observed star formation properties we tested different parameters of the adopted star formation and feedback model (Springel & Hernquist 2003) and found that the relative strength and the exact locations of intensively star-forming sites in the overlap region is reproduced in best quantitative agreement if we adopt a very weak stellar feedback in the star formation model, close to an isothermal effective equation of state (Springel et al. 2005). This is confirmed in detailed mock FIR and CO maps of the Antennae. The underlying reason that allows us, for the first time, to explain these features in such great detail is the exact timing of the merger. We find that the time of best match is confined to a very short period ($\Delta t \approx 20$ Myr) after the second encounter. This is the only phase in the simulations when a gas-rich overlap region between the nuclei is forming accompanied by enhanced star formation. These results indicate that we observe the Antennae in a very special moment of their evolution. In our model, they have passed the second pericenter about 40 Myr ago and will have their final collision and merger in only another ~ 50 Myr. Moreover, the proposed time of best match implies that the Antennae are in a more advanced phase of the merger than found in previous numerical models. This could possibly require a revision of the Toomre merger sequence (Toomre 1977).

Interacting and merging galaxies like the Antennae galaxies are well-known triggers for the formation of young star clusters (e.g. Holtzman et al. 1992; Meurer et al. 1995; Whitmore & Schweizer 1995). Subsequently, most of the clusters are destroyed by several internal and external processes (Fall et al. 2009; Portegies Zwart et al. 2010) and will eventually disperse into the stellar field. We have focused on the age distribution of star clusters in the Antennae galaxies in Chapter 6. Using the excellent statistics of the rich star cluster population in the Antennae their age distribution is found to be well approximated by a power-law $dN/d\tau \propto \tau^{-\gamma}$ with $\gamma \approx 1$. In a sample of ~ 20 local galaxies, including quiescent galaxies with a nearly constant SFR over the last $\sim 10^9$ yr, such as the Milky Way or the Magellanic Clouds, the cluster age distributions are observed to decline equally steep, with a power law of the form $dN/d\tau \propto \tau^{-\gamma}$ with $\gamma \approx 0.7-1.0$. Since the observed age distribution reflects the combined cluster formation and disruption histories of a galaxy, this decline may be understood as a hint for very efficient disruption of star clusters, at least in the more quiescent galaxies. To test if this interpretation also holds in interacting, non-quiescent galaxies, we have gathered the star formation histories from all available hydrodynamical simulations of the Antennae, including different interaction orbits, different numerical methods, and different prescriptions for the star formation and stellar feedback. Assuming that the SFR is a direct tracer for the cluster formation rate, we have shown that the star formation histories of *all* Antennae simulations cannot account alone for most of the decline in the observed cluster age distribution. The reason for this is that the SFRs in all simulations vary relatively slowly with time — despite them experiencing an on-going merger. In particular, they have varied by factors of only $1.3-2.5$ in the past $\sim 10^8$ yr.

This means that the simulated cluster formation histories can only be reconciled with the observed age distribution when we combine it with a power-law model for the fraction of clusters, $f_{\rm surv} \propto \tau^{\delta}$, that survive to each age τ. We find good agreement to the observed age distribution with exponents in the range $-0.9 \lesssim \delta \lesssim -0.6$ if cluster disruption lasts for at least $\sim 10^8$ yr and possibly $\sim 10^9$ yr. The necessity to adopt a model for the star cluster survival fraction that is equally steep as the observed cluster age distribution suggests that the latter is mainly shaped by the disruption of clusters rather than variations in their formation rate. Hence, we conclude that star clusters in the Antennae galaxies are disrupted in much the same way as those in other galaxies.

Finally, we have assessed the future evolution of the Antennae and addressed the question of whether our bona-fide model of the present-day Antennae will evolve into a typical elliptical galaxy. At an age $\tau_{\rm remnant} = 1\,{\rm Gyr}$, the remnant has already returned to virial equilibrium and resembles an intrinsically oblate system with a rotating stellar core. Its projected surface brightness profile is very well represented by a Sérsic function with Sérsic index $n \sim 5$ with a significant amount of "extra-light" at the center. Thus, the photometric and kinematic properties of the virialized merger remnant are in good agreement with observed intermediate-mass elliptical galaxies, which confirms results from previous numerical simulations. Regarding the photometric properties of the young merger remnant, the colors, however, are far too blue to represent a typical present-day elliptical. Therefore, we have examined the evolution of the stellar remnant with time up to remnant ages $\tau_{\rm remnant} \leq 4\,{\rm Gyr}$, assuming no further star formation for $\tau_{\rm remnant} > 1.0\,{\rm Gyr}$. For sufficiently high metallicities ($Z \gtrsim Z_{\odot}$), the stellar populations show properties, such as mean stellar ages and the locations in the color-magnitude diagram, which are in good agreement with local early-type galaxies for remnant ages $2.5\,{\rm Gyr} < \tau_{\rm remnant} < 3\,{\rm Gyr}$. This indicates that a plausible future remnant of an Antennae-like merger may add to a population of typical present-day intermediate-mass ellipticals after additional secular evolution of $\sim 2.5 - 3\,{\rm Gyr}$, reddening even further at older ages.

8.2 Perspectives

We have proposed an improved numerical model for the interacting Antennae galaxies that may serve as a solid basis and test-bed for further theoretical investigations of this spectacular merging system. As next steps within this context, it would be extremely interesting to generate further mock observations in additional wavelengths to obtain a more complete spectral coverage of the simulation data. Having the full multi-wavelength picture at hand, one can put more stringent constraints on the proposed theoretical models, and improve them accordingly. It would be particularly interesting to test new numerical feedback models, that are desperately needed in current cosmological and galactic-scale simulations, against the spatially-resolved properties of the

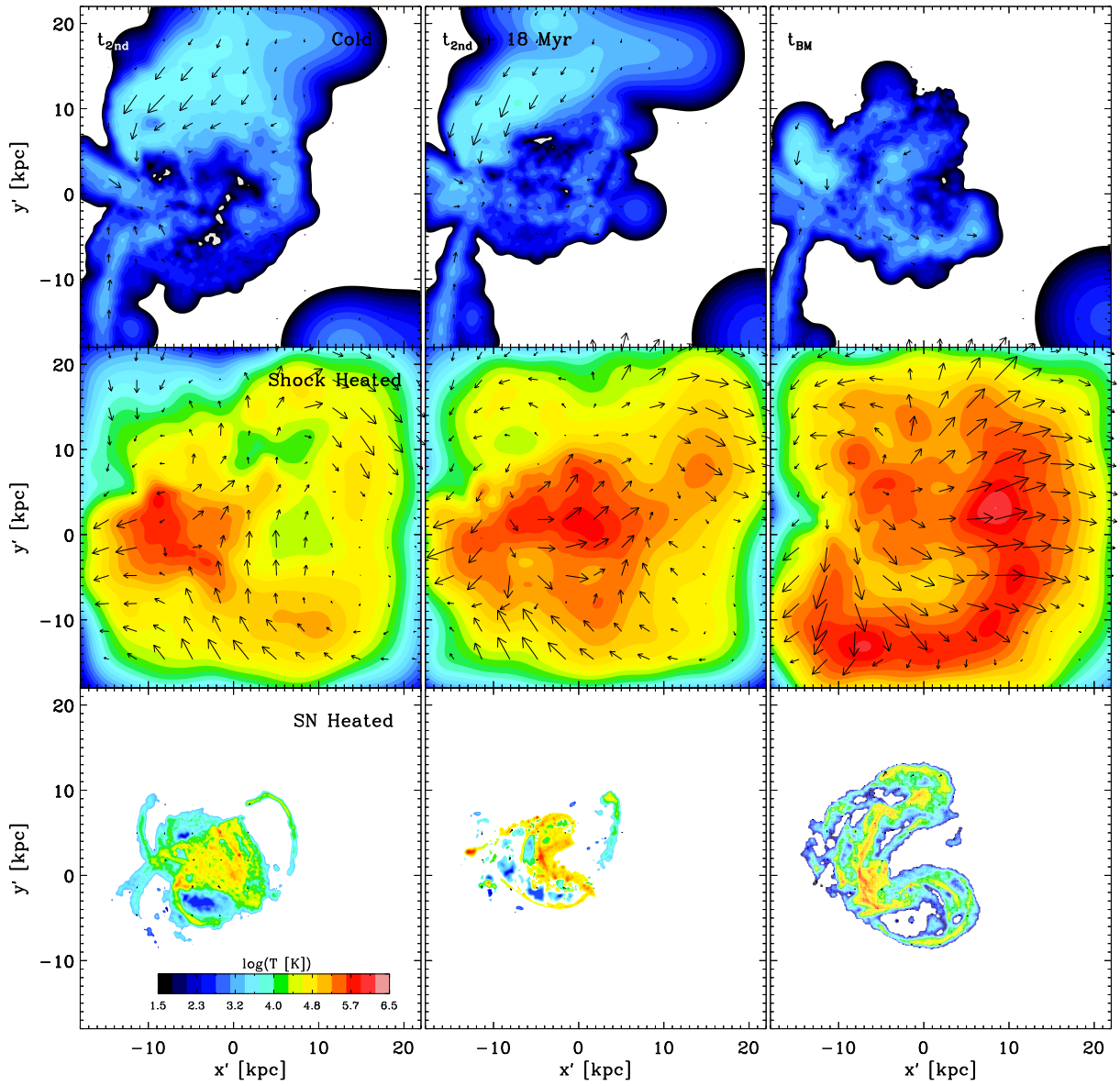

Figure 8.1: Evolution of temperature (colors) and tangential gas velocities (arrows) at the time of second pericenter $t_{2\mathrm{nd}}$ *(left column)*, the time of best match t_{BM} *(right column)*, and an intermediate time $t \approx t_{2\mathrm{nd}} + 18\,\mathrm{Myr}$ *(middle column)* for the fiducial Antennae model. We show the time evolution separately for the cold, non-star-forming gas particles with $T < 3 \times 10^4$ K *(upper panels)*, hot shock-heated, non-star-forming gas particles with $T > 3 \times 10^4$ K *(middle panels)*, and the dense star-forming gas particles ($n > n_{\mathrm{crit}}$) treated by the effective multi-phase model *lower panels)*. An arrow of length 1 corresponds to a velocity of $25\,\mathrm{km\,s^{-1}}$.

ISM in the Antennae. This includes, most importantly, the generation of large-scale AGN- and supernovae-driven galactic winds.

As a first step in this direction, we plan to investigate the detailed properties of the extended hot gas component found in Chandra X-ray observations of the Antennae. Our goal is to explain which mechanism is mainly responsible for driving the large-scale loops of hot X-ray gas to the south of the Antennae galaxies. Possible mechanisms are, e.g. the expansion of shock-heated gas, and starburst- or AGN-driven outflows. Furthermore, a code comparison project with the adaptive-mesh-refinement grid code RAMSES was started which will enable us to assess the robustness of the proposed dynamical model to possible numerical artifacts in the simulations and test different physical prescriptions of the codes against each other.

In the following, we want to address the first question in a little more detail, presenting the very first results of an analysis of out-flowing gas in our Antennae models. Figure 8.1 presents temperature maps at three different times between second pericenter and the time of best match. Additionally, we have divided the gas into three different phases according to their temperatures and densities. Non-star-forming particles ($n < n_{\rm crit} = 0.128\,{\rm cm}^{-3}$) are tagged as either "cold" gas (upper panel) or hot, "shock-heated" (middle panel) gas for temperatures $T < 4 \times 10^8$ K and $T > 4 \times 10^8$ K, respectively. The remaining particles constitute the star-forming, "supernovae-heated" gas phase ($n > n_{\rm crit}$, lower panel) which is treated by the effective multi-phase star formation model (Springel & Hernquist 2003). The cold and star-forming gas phases show very small or even in-flowing tangential velocities and are found to be located near the main galaxies. Only the shock-heated, non-star-forming gas is more extended, out to radii $\lesssim 18\,{\rm kpc}$ at the three different times and has developed a very powerful, galactic-scale outflow at the time of best match. The hot outflow is oriented mostly towards the southern (lower) and western (right) part of the system, similar to the hot X-ray halo in the Antennae galaxies. Since the fiducial model uses only very weak stellar-, and no AGN-feedback, we conclude that the hot X-ray halo of the Antennae could have formed mainly from hot, shock-heated gas that is expanding after the collision of the two galaxies at the second pericenter.

To constrain this question further, in Figure 8.2, we show simple synthetic X-ray maps for the fiducial model, together with new simulations with additional black hole feedback (middle panel; Springel et al. 2005) and a hot gas halo surrounding the main galaxies (right panel; constructed according to Moster et al. 2010b) at the time of best match. We calculate the total X-ray luminosity between $0.1 - 10$ eV following Evrard (1990), assuming a hot, optically thin plasma which emits mainly via thermal Bremsstrahlung. For all three simulations, we find that the X-ray emission is extended more towards the south, and is nicely identified with the morphology of the extended X-ray gas in the Antennae (see Figure 2.6). The simulations with and without black hole feedback (middle and left panel) are quite similar due to a relatively low black

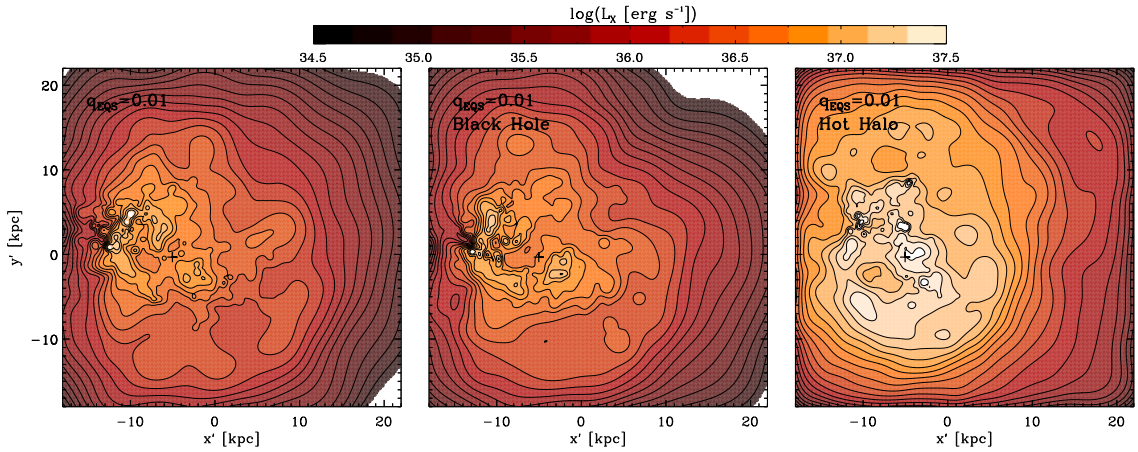

Figure 8.2: Synthetic thermal X-ray emission from three different Antennae simulations including the fiducial simulation and two simulations with additional black hole feedback and a hot halo component, respectively. The X-ray luminosity is computed using the formula from Evrard (1990), assuming thermal emission from a hot, optically thin plasma. Black crosses denote the galaxy center of each simulation.

hole accretion at that time, which will rise, however, significantly, after the final galaxy merger. The additional hot gas halo (right panel) shows an increased X-ray emission due the high temperatures and the additional gas mass that is accreting onto the galaxies. Indications for interesting details, such as X-ray loops, are already present in Figure 8.2, especially for the fiducial Antennae model (left panel). The next step will be to apply a more sophisticated X-ray photon simulator (e.g. "PHOX" by V. Biffi at MPE), which, e.g. includes non-thermal emission from metal line cooling, and a treatment of the instrument response (i.e. Chandra ACIS in our case). Likewise, it would be highly beneficial to add a treatment for the evolution of metals to our simulations in order to enable a fair comparison with the data.

As a final remark, it seems that detailed and accurate dynamical modeling using modern simulation codes is an important key to explain many of the puzzling features observed in nearby interacting galaxies. Therefore, it would be highly desirable to extend the number of reliable dynamical models to a larger number of systems, e.g. from the Toomre sequence (Toomre 1977; Laine et al. 2003) or the nearby GOALS sample (Armus et al. 2009), by using fast, new modeling techniques (e.g. "Identikit", see Chapter 4). In particular, with these samples one could probe a larger baseline of different merger stages, different orbit geometries, and different types of progenitor galaxies. This would nicely help to generalize the results obtained in the present study for one of the prototypical merger systems — the Antennae.

References

Aarseth, S. J.: 1963. Dynamical evolution of clusters of galaxies, I. *MNRAS*, **126**, 223.

Appel, A.: 1985. An efficient program for many-body simulation. *SIAM Journal on Scientific and Statistical Computing*, **6**, 85.

Armus, L., Mazzarella, J. M., Evans, A. S., Surace, J. A., Sanders, D. B., Iwasawa, K., Frayer, D. T., Howell, J. H., Chan, B., Petric, A., Vavilkin, T., Kim, D. C., Haan, S., Inami, H., Murphy, E. J., Appleton, P. N., Barnes, J. E., Bothun, G., Bridge, C. R., Charmandaris, V., Jensen, J. B., Kewley, L. J., Lord, S., Madore, B. F., Marshall, J. A., Melbourne, J. E., Rich, J., Satyapal, S., Schulz, B., Spoon, H. W. W., Sturm, E., U, V., Veilleux, S., Xu, K.: 2009. GOALS: The Great Observatories All-Sky LIRG Survey. *PASP*, **121**, 559–576.

Arp, H.: 1966. Atlas of Peculiar Galaxies. *ApJS*, **14**, 1.

Athanassoula, E., Fady, E., Lambert, J. C., Bosma, A.: 2000. Optimal softening for force calculations in collisionless N-body simulations. *MNRAS*, **314**, 475–488.

Baade, W. Minkowski, R.: 1954a. Abnormal galaxies as radio sources. *The Observatory*, **74**, 130–131.

Baade, W. Minkowski, R.: 1954b. Identification of the Radio Sources in Cassiopeia, Cygnus a, and Puppis a. *ApJ*, **119**, 206.

Baldi, A., Raymond, J. C., Fabbiano, G., Zezas, A., Rots, A. H., Schweizer, F., King, A. R., Ponman, T. J.: 2006a. Chemical Enrichment of the Complex Hot ISM of the Antennae Galaxies. I. Spatial and Spectral Analysis of the Diffuse X-Ray Emission. *ApJS*, **162**, 113–133.

Baldi, A., Raymond, J. C., Fabbiano, G., Zezas, A., Rots, A. H., Schweizer, F., King, A. R., Ponman, T. J.: 2006b. Chemical Enrichment of the Complex Hot

ISM of the Antennae Galaxies. II. Physical Properties of the Hot Gas and Supernova Feedback. *ApJ*, **636**, 158–171.

Balsara, D. S.: 1995. von Neumann stability analysis of smooth particle hydrodynamics–suggestions for optimal algorithms. *Journal of Computational Physics*, **121**, 357–372.

Barnes, J. Hut, P.: 1986. A Hierarchical O(NlogN) Force-Calculation Algorithm. *Nature*, **324**, 446–449.

Barnes, J. E.: 1988. Encounters of disk/halo galaxies. *ApJ*, **331**, 699–717.

Barnes, J. E.: 1990. A Modified Tree Code Don't Laugh: It Runs. *Journal of Computational Physics*, **87**, 161.

Barnes, J. E.: 1992. Transformations of galaxies. I - Mergers of equal-mass stellar disks. *ApJ*, **393**, 484–507.

Barnes, J. E.: 2002. Formation of gas discs in merging galaxies. *MNRAS*, **333**, 481–494.

Barnes, J. E.: 2004. Shock-induced star formation in a model of the Mice. *MNRAS*, **350**, 798–808.

Barnes, J. E.: 2011. Identikit 2: an algorithm for reconstructing galactic collisions. *MNRAS*, **413**, 2860–2872.

Barnes, J. E. Hernquist, L.: 1996. Transformations of Galaxies. II. Gasdynamics in Merging Disk Galaxies. *ApJ*, **471**, 115.

Barnes, J. E. Hibbard, J. E.: 2009. Identikit 1: A Modeling Tool for Interacting Disk Galaxies. *AJ*, **137**, 3071–3090.

Bastian, N., Emsellem, E., Kissler-Patig, M., Maraston, C.: 2006. Young star cluster complexes in NGC 4038/39. Integral field spectroscopy using VIMOS-VLT. *A&A*, **445**, 471–483.

Bastian, N., Trancho, G., Konstantopoulos, I. S., Miller, B. W.: 2009. Gemini Spectroscopic Survey of Young Star Clusters in Merging/Interacting Galaxies. III. The Antennae. *ApJ*, **701**, 607–619.

Baumgardt, H. Kroupa, P.: 2007. A comprehensive set of simulations studying the influence of gas expulsion on star cluster evolution. *MNRAS*, **380**, 1589–1598.

Bekki, K., Forbes, D. A., Beasley, M. A., Couch, W. J.: 2002. Globular cluster formation from gravitational tidal effects of merging and interacting galaxies. *MNRAS*, **335**, 1176–1192.

Bell, E. F. de Jong, R. S.: 2001. Stellar Mass-to-Light Ratios and the Tully-Fisher Relation. *ApJ*, **550**, 212–229.

Bender, R. Moellenhoff, C.: 1987. Morphological analysis of massive early-type galaxies in the Virgo cluster. *A&A*, **177**, 71–83.

Bender, R., Saglia, R. P., Gerhard, O. E.: 1994. Line-of-Sight Velocity Distributions of Elliptical Galaxies. *MNRAS*, **269**, 785.

Bender, R., Surma, P., Doebereiner, S., Moellenhoff, C., Madejsky, R.: 1989. Isophote shapes of elliptical galaxies. II - Correlations with global optical, radio and X-ray properties. *A&A*, **217**, 35–43.

Bigiel, F., Leroy, A., Walter, F., Brinks, E., de Blok, W. J. G., Madore, B., Thornley, M. D.: 2008. The Star Formation Law in Nearby Galaxies on Sub-Kpc Scales. *AJ*, **136**, 2846–2871.

Binney, J. Merrifield, M.: 1998. *Galactic astronomy.*

Binney, J. Tremaine, S.: 2008. *Galactic Dynamics: Second Edition.* Princeton University Press.

Bois, M., Emsellem, E., Bournaud, F., Alatalo, K., Blitz, L., Bureau, M., Cappellari, M., Davies, R. L., Davis, T. A., de Zeeuw, P. T., Duc, P.-A., Khochfar, S., Krajnović, D., Kuntschner, H., Lablanche, P.-Y., McDermid, R. M., Morganti, R., Naab, T., Oosterloo, T., Sarzi, M., Scott, N., Serra, P., Weijmans, A.-M., Young, L. M.: 2011. The ATLAS^{3D} project - VI. Simulations of binary galaxy mergers and the link with fast rotators, slow rotators and kinematically distinct cores. *MNRAS*, Seite 1257.

Bournaud, F., Duc, P.-A., Emsellem, E.: 2008. High-resolution simulations of galaxy mergers: resolving globular cluster formation. *MNRAS*, **389**, L8–L12.

Bournaud, F., Jog, C. J., Combes, F.: 2007. Multiple minor mergers: formation of elliptical galaxies and constraints for the growth of spiral disks. *A&A*, **476**, 1179–1190.

Brandl, B. R., Clark, D. M., Eikenberry, S. S., Wilson, J. C., Henderson, C. P., Barry, D. J., Houck, J. R., Carson, J. C., Hayward, T. L.: 2005. Deep Near-Infrared Imaging and Photometry of the Antennae Galaxies with WIRC. *ApJ*, **635**, 280–289.

Brandl, B. R., Snijders, L., den Brok, M., Whelan, D. G., Groves, B., van der Werf, P., Charmandaris, V., Smith, J. D., Armus, L., Kennicutt, R. C., Houck, J. R.: 2009. Spitzer-IRS Study of the Antennae Galaxies NGC 4038/39. *ApJ*, **699**, 1982–2001.

Bridge, C. R., Appleton, P. N., Conselice, C. J., Choi, P. I., Armus, L., Fadda, D., Laine, S., Marleau, F. R., Carlberg, R. G., Helou, G., Yan, L.: 2007. The Role of Galaxy Interactions and Mergers in Star Formation at z<=1.3: Mid-Infrared Properties in the Spitzer First Look Survey. *ApJ*, **659**, 931–940.

Bridge, C. R., Carlberg, R. G., Sullivan, M.: 2010. The CFHTLS-Deep Catalog of Interacting Galaxies. I. Merger Rate Evolution to z = 1.2. *ApJ*, **709**, 1067–1082.

Bruzual, G. Charlot, S.: 2003. Stellar population synthesis at the resolution of 2003. *MNRAS*, **344**, 1000–1028.

Bullock, J. S., Dekel, A., Kolatt, T. S., Kravtsov, A. V., Klypin, A. A., Porciani, C., Primack, J. R.: 2001a. A Universal Angular Momentum Profile for Galactic Halos. *ApJ*, **555**, 240–257.

Bullock, J. S., Kolatt, T. S., Sigad, Y., Somerville, R. S., Kravtsov, A. V., Klypin, A. A., Primack, J. R., Dekel, A.: 2001b. Profiles of dark haloes: evolution, scatter and environment. *MNRAS*, **321**, 559–575.

Burbidge, E. M. Burbidge, G. R.: 1966. The Velocity Field in the Peculiar Extragalactic System NGC 4038-39. *ApJ*, **145**, 661.

Caon, N., Capaccioli, M., D'Onofrio, M.: 1993. On the Shape of the Light Profiles of Early Type Galaxies. *MNRAS*, **265**, 1013.

Cappellari, M. Copin, Y.: 2003. Adaptive spatial binning of integral-field spectroscopic data using Voronoi tessellations. *MNRAS*, **342**, 345–354.

Cappellari, M., Emsellem, E., Bacon, R., Bureau, M., Davies, R. L., de Zeeuw, P. T., Falcón-Barroso, J., Krajnović, D., Kuntschner, H., McDermid, R. M., Peletier, R. F., Sarzi, M., van den Bosch, R. C. E., van de Ven, G.: 2007. The SAURON project - X. The orbital anisotropy of elliptical and lenticular galaxies: revisiting the (V/σ, ϵ) diagram with integral-field stellar kinematics. *MNRAS*, **379**, 418–444.

Cappellari, M., Emsellem, E., Krajnović, D., McDermid, R. M., Scott, N., Verdoes Kleijn, G. A., Young, L. M., Alatalo, K., Bacon, R., Blitz, L., Bois, M., Bournaud, F., Bureau, M., Davies, R. L., Davis, T. A., de Zeeuw, P. T., Duc, P.-A., Khochfar, S., Kuntschner, H., Lablanche, P.-Y., Morganti, R., Naab, T., Oosterloo, T., Sarzi, M., Serra, P., Weijmans, A.-M.: 2011. The ATLAS^{3D} project - I. A volume-limited sample of 260 nearby early-type galaxies: science goals and selection criteria. *MNRAS*, **413**, 813–836.

Chandar, R., Fall, S. M., Whitmore, B. C.: 2010a. New Tests for Disruption Mechanisms of Star Clusters: The Large and Small Magellanic Clouds. *ApJ*, **711**, 1263–1279.

Chandar, R., Whitmore, B. C., Calzetti, D., Di Nino, D., Kennicutt, R. C., Regan, M., Schinnerer, E.: 2011. New Constraints on Mass-dependent Disruption of Star Clusters in M51. *ApJ*, **727**, 88.

Chandar, R., Whitmore, B. C., Fall, S. M.: 2010b. A Comparison of Methods for Determining the Age Distribution of Star Clusters: Application to the Large Magellanic Cloud. *ApJ*, **713**, 1343–1349.

Chandar, R., Whitmore, B. C., Kim, H., Kaleida, C., Mutchler, M., Calzetti, D., Saha, A., O'Connell, R., Balick, B., Bond, H., Carollo, M., Disney, M., Dopita, M. A., Frogel, J. A., Hall, D., Holtzman, J. A., Kimble, R. A., McCarthy, P., Paresce, F., Silk, J., Trauger, J., Walker, A. R., Windhorst, R. A., Young, E.: 2010c. The Luminosity, Mass, and Age Distributions of Compact Star Clusters in M83 Based on Hubble Space Telescope/Wide Field Camera 3 Observations. *ApJ*, **719**, 966–978.

Chernoff, D. F. Weinberg, M. D.: 1990. Evolution of globular clusters in the Galaxy. *ApJ*, **351**, 121–156.

Chyży, K. T. Beck, R.: 2004. Magnetic fields in merging spirals - the Antennae. *A&A*, **417**, 541–555.

Clutton-Brock, M.: 1972. How Are Intergalactic Filaments Made? *Ap&SS*, **17**, 292–324.

Conselice, C. J., Bershady, M. A., Dickinson, M., Papovich, C.: 2003. A Direct Measurement of Major Galaxy Mergers at z<˜3. *AJ*, **126**, 1183–1207.

Conselice, C. J., Bundy, K., Trujillo, I., Coil, A., Eisenhardt, P., Ellis, R. S., Georgakakis, A., Huang, J., Lotz, J., Nandra, K., Newman, J., Papovich, C., Weiner, B., Willmer, C.: 2007. The properties and evolution of a K-band selected sample of massive galaxies at z ˜ 0.4-2 in the Palomar/DEEP2 survey. *MNRAS*, **381**, 962–986.

Conselice, C. J., Yang, C., Bluck, A. F. L.: 2009. The structures of distant galaxies - III. The merger history of over 20000 massive galaxies at z < 1.2. *MNRAS*, **394**, 1956–1972.

Courant, R., Friedrichs, K., Lewy, H.: 1928. Über die partiellen Differenzengleichungen der mathematischen Physik. *Mathematische Annalen*, **100**, 32–74.

Cox, T. J., Dutta, S. N., Di Matteo, T., Hernquist, L., Hopkins, P. F., Robertson, B., Springel, V.: 2006. The Kinematic Structure of Merger Remnants. *ApJ*, **650**, 791–811.

Cox, T. J., Jonsson, P., Somerville, R. S., Primack, J. R., Dekel, A.: 2008. The effect of galaxy mass ratio on merger-driven starbursts. *MNRAS*, **384**, 386–409.

Cullen, H., Alexander, P., Green, D. A., Clemens, M., Sheth, K.: 2007. The unusual distribution of molecular gas and star formation in Arp 140. *MNRAS*, **374**, 1185–1197.

Dame, T. M.: 1993. The Distribution of Neutral Gas in the Milky Way. In Holt, S. S. Verter, F., editors, *Back to the Galaxy*, volume 278 of *American Institute of Physics Conference Series*, Seiten 267–278.

Dasyra, K. M., Tacconi, L. J., Davies, R. I., Genzel, R., Lutz, D., Naab, T., Burkert, A., Veilleux, S., Sanders, D. B.: 2006a. Dynamical Properties of Ultraluminous Infrared Galaxies. I. Mass Ratio Conditions for ULIRG Activity in Interacting Pairs. *ApJ*, **638**, 745–758.

Dasyra, K. M., Tacconi, L. J., Davies, R. I., Naab, T., Genzel, R., Lutz, D., Sturm, E., Baker, A. J., Veilleux, S., Sanders, D. B., Burkert, A.: 2006b. Dynamical Properties of Ultraluminous Infrared Galaxies. II. Traces of Dynamical Evolution and End Products of Local Ultraluminous Mergers. *ApJ*, **651**, 835–852.

Davies, R. L., Efstathiou, G., Fall, S. M., Illingworth, G., Schechter, P. L.: 1983. The kinematic properties of faint elliptical galaxies. *ApJ*, **266**, 41–57.

de Vaucouleurs, G.: 1948. Recherches sur les Nebuleuses Extragalactiques. *Annales d'Astrophysique*, **11**, 247.

de Vaucouleurs, G., de Vaucouleurs, A., Corwin, Jr., H. G., Buta, R. J., Paturel, G., Fouque, P.: 1991. *Third Reference Catalogue of Bright Galaxies*.

Dehnen, W.: 2000. A Very Fast and Momentum-conserving Tree Code. *ApJ*, **536**, L39–L42.

Dehnen, W.: 2001. Towards optimal softening in three-dimensional N-body codes - I. Minimizing the force error. *MNRAS*, **324**, 273–291.

den Brok, M., Peletier, R. F., Valentijn, E. A., Balcells, M., Carter, D., Erwin, P., Ferguson, H. C., Goudfrooij, P., Graham, A. W., Hammer, D., Lucey, J. R., Trentham, N., Guzmán, R., Hoyos, C., Verdoes Kleijn, G., Jogee, S., Karick, A. M., Marinova, I., Mouhcine, M., Weinzirl, T.: 2011. The HST/ACS Coma Cluster Survey - VI. Colour gradients in giant and dwarf early-type galaxies. *MNRAS*, **414**, 3052–3070.

Dinshaw, N., Evans, A. S., Epps, H., Scoville, N. Z., Rieke, M.: 1999. NICMOS Observations of Interaction-triggered Star Formation in the Luminous Infrared Galaxy NGC 6090. *ApJ*, **525**, 702–708.

Draine, B. T.: 2003. Interstellar Dust Grains. *ARA&A*, **41**, 241–289.

Drake, A. J., Djorgovski, S. G., Williams, R., Mahabal, A., Graham, M. J., Christensen, E., Beshore, E. C., Larson, S. M.: 2007. Supernova 2007sr in NGC 4038. *Central Bureau Electronic Telegrams*, **1172**, 1.

Drzazga, R. T., Chyży, K. T., Jurusik, W., Wiórkiewicz, K.: 2011. Magnetic field evolution in interacting galaxies. *A&A*, **533**, A22+.

Dubinski, J., Mihos, J. C., Hernquist, L.: 1996. Using Tidal Tails to Probe Dark Matter Halos. *ApJ*, **462**, 576.

Dubinski, J., Mihos, J. C., Hernquist, L.: 1999. Constraining Dark Halo Potentials with Tidal Tails. *ApJ*, **526**, 607–622.

Duc, P.-A. Mirabel, I. F.: 1998. Young tidal dwarf galaxies around the gas-rich disturbed lenticular NGC 5291. *A&A*, **333**, 813–826.

Duffy, A. R., Schaye, J., Kay, S. T., Dalla Vecchia, C.: 2008. Dark matter halo concentrations in the Wilkinson Microwave Anisotropy Probe year 5 cosmology. *MNRAS*, **390**, L64–L68.

Duncan, J. C.: 1923. Photographic studies of nebulae. III. *ApJ*, **57**, 137–148.

Eddington, A. S.: 1916. The distribution of stars in globular clusters. *MNRAS*, **76**, 572–585.

Emsellem, E., Cappellari, M., Krajnović, D., Alatalo, K., Blitz, L., Bois, M., Bournaud, F., Bureau, M., Davies, R. L., Davis, T. A., de Zeeuw, P. T., Khochfar, S., Kuntschner, H., Lablanche, P.-Y., McDermid, R. M., Morganti, R., Naab, T., Oosterloo, T., Sarzi, M., Scott, N., Serra, P., van de Ven, G., Weijmans, A.-M., Young, L. M.: 2011. The ATLAS^{3D} project - III. A census of the stellar angular momentum within the effective radius of early-type galaxies: unveiling the distribution of fast and slow rotators. *MNRAS*, **414**, 888–912.

Emsellem, E., Cappellari, M., Krajnović, D., van de Ven, G., Bacon, R., Bureau, M., Davies, R. L., de Zeeuw, P. T., Falcón-Barroso, J., Kuntschner, H., McDermid, R., Peletier, R. F., Sarzi, M.: 2007. The SAURON project - IX. A kinematic classification for early-type galaxies. *MNRAS*, **379**, 401–417.

Engel, H., Davies, R. I., Genzel, R., Tacconi, L. J., Hicks, E. K. S., Sturm, E., Naab, T., Johansson, P. H., Karl, S. J., Max, C. E., Medling, A., van der Werf, P. P.: 2010. NGC 6240: merger-induced star formation and gas dynamics. *A&A*, **524**, A56+.

Evrard, A. E.: 1990. Formation and evolution of X-ray clusters - A hydrodynamic simulation of the intracluster medium. *ApJ*, **363**, 349–366.

Fabbiano, G., Baldi, A., King, A. R., Ponman, T. J., Raymond, J., Read, A., Rots, A., Schweizer, F., Zezas, A.: 2004. X-Raying Chemical Evolution and Galaxy Formation in the Antennae. *ApJ*, **605**, L21–L24.

Fabbiano, G., Zezas, A., Murray, S. S.: 2001. Chandra Observations of "The Antennae" Galaxies (NGC 4038/9). *ApJ*, **554**, 1035–1043.

Fall, S. M., Chandar, R., Whitmore, B. C.: 2005. The Age Distribution of Massive Star Clusters in the Antennae Galaxies. *ApJ*, **631**, L133–L136.

Fall, S. M., Chandar, R., Whitmore, B. C.: 2009. New Tests for Disruption Mechanisms of Star Clusters: Methods and Application to the Antennae Galaxies. *ApJ*, **704**, 453–468.

Fall, S. M., Krumholz, M. R., Matzner, C. D.: 2010. Stellar Feedback in Molecular Clouds and its Influence on the Mass Function of Young Star Clusters. *ApJ*, **710**, L142–L146.

Firth, P., Evstigneeva, E. A., Jones, J. B., Drinkwater, M. J., Phillipps, S., Gregg, M. D.: 2006. Kinematics, substructure and luminosity-weighted dynamics of six nearby galaxy groups. *MNRAS*, **372**, 1856–1868.

Fischler, M. A. Firschein, O.: 1987. *Intelligence: The eye, the brain, and the computer*. Addison-Wesley Pub. Co. Inc.,Reading, MA.

Franx, M., Illingworth, G., Heckman, T.: 1989. Multicolor surface photometry of 17 ellipticals. *AJ*, **98**, 538–576.

Gao, Y., Lo, K. Y., Lee, S.-W., Lee, T.-H.: 2001. Molecular Gas and the Modest Star Formation Efficiency in the "Antennae" Galaxies: Arp 244=NGC 4038/9. *ApJ*, **548**, 172–189.

Geng, A., Kotarba, H., Bürzle, F., Dolag, K., Stasyszyn, F., Beck, A., Nielaba, P.: 2011. Magnetic field amplification and X-ray emission in galaxy minor mergers. *ArXiv e-prints*.

Genzel, R., Tacconi, L. J., Rigopoulou, D., Lutz, D., Tecza, M.: 2001. Ultraluminous Infrared Mergers: Elliptical Galaxies in Formation? *ApJ*, **563**, 527–545.

Gieles, M., Bastian, N., Lamers, H. J. G. L. M., Mout, J. N.: 2005. The star cluster population of M 51. III. Cluster disruption and formation history. *A&A*, **441**, 949–960.

Gilbert, A. M. Graham, J. R.: 2007. Feedback in the Antennae Galaxies (NGC 4038/9). I. High-Resolution Infrared Spectroscopy of Winds from Super Star Clusters. *ApJ*, **668**, 168–181.

Gingold, R. A. Monaghan, J. J.: 1977. Smoothed particle hydrodynamics - Theory and application to non-spherical stars. *MNRAS*, **181**, 375–389.

Goddard, Q. E., Bastian, N., Kennicutt, R. C.: 2010. On the fraction of star clusters surviving the embedded phase. *MNRAS*, **405**, 857–869.

Gonzalez-Perez, V., Castander, F. J., Kauffmann, G.: 2011. Colour gradients within SDSS DR7 galaxies: hints of recent evolution. *MNRAS*, **411**, 1151–1166.

Gordon, S., Koribalski, B., Jones, K.: 2001. H i observations of interacting galaxy pair NGC 4038/9. *MNRAS*, **326**, 578–596.

Guedes, J., Callegari, S., Madau, P., Mayer, L.: 2011. Forming Realistic Late-Type Spirals in a LCDM Universe: The Eris Simulation. *ArXiv e-prints*.

Guo, Q., White, S., Li, C., Boylan-Kolchin, M.: 2010. How do galaxies populate dark matter haloes? *MNRAS*, **404**, 1111–1120.

Haardt, F. Madau, P.: 1996. Radiative Transfer in a Clumpy Universe. II. The Ultraviolet Extragalactic Background. *ApJ*, **461**, 20.

Haas, M., Klaas, U., Coulson, I., Thommes, E., Xu, C.: 2000. The cold dust concentrations in the colliding galaxies NGC 4038/39. *A&A*, **356**, L83–L87.

Harris, J. Zaritsky, D.: 2004. The Star Formation History of the Small Magellanic Cloud. *AJ*, **127**, 1531–1544.

Harris, J. Zaritsky, D.: 2009. The Star Formation History of the Large Magellanic Cloud. *AJ*, **138**, 1243–1260.

Hernquist, L.: 1990. An analytical model for spherical galaxies and bulges. *ApJ*, **356**, 359–364.

Herschel, J. F. W.: 1833. Observations of Nebulae and Clusters of Stars, Made at Slough, with a Twenty-Feet Reflector, between the Years 1825 and 1833. *Royal Society of London Philosophical Transactions Series I*, **123**, 359–505.

Hibbard, J. E.: 2003. The Antennae in the Merging Sequence. In *Bulletin of the American Astronomical Society*, volume 35 of *Bulletin of the American Astronomical Society*, Seite 1413.

Hibbard, J. E., Bianchi, L., Thilker, D. A., Rich, R. M., Schiminovich, D., Xu, C. K., Neff, S. G., Seibert, M., Lauger, S., Burgarella, D., Barlow, T. A., Byun, Y., Donas, J., Forster, K., Friedman, P. G., Heckman, T. M., Jelinsky, P. N., Lee, Y., Madore, B. F., Malina, R. F., Martin, D. C., Milliard, B., Morrissey, P., Siegmund, O. H. W., Small, T., Szalay, A. S., Welsh, B. Y., Wyder, T. K.: 2005. Ultraviolet Morphology and Star Formation in the Tidal Tails of NGC 4038/39. *ApJ*, **619**, L87–L90.

Hibbard, J. E., van der Hulst, J. M., Barnes, J. E., Rich, R. M.: 2001. High-Resolution H I Mapping of NGC 4038/39 ("The Antennae") and Its Tidal Dwarf Galaxy Candidates. *AJ*, **122**, 2969–2992.

Hills, J. G.: 1980. The effect of mass loss on the dynamical evolution of a stellar system - Analytic approximations. *ApJ*, **235**, 986–991.

Hockney, R. W. Eastwood, J. W.: 1981. *Computer Simulation Using Particles.*

Holland, J. H.: 1975. *Adaptation in natural and artificial systems. an introductory analysis with applications to biology, control and artificial intelligence.*

Holmberg, E.: 1941. On the Clustering Tendencies among the Nebulae. II. a Study of Encounters Between Laboratory Models of Stellar Systems by a New Integration Procedure. *ApJ*, **94**, 385.

Holtzman, J. A., Faber, S. M., Shaya, E. J., Lauer, T. R., Groth, J., Hunter, D. A., Baum, W. A., Ewald, S. P., Hester, J. J., Light, R. M., Lynds, C. R., O'Neil, Jr., E. J., Westphal, J. A.: 1992. Planetary Camera observations of NGC 1275 - Discovery of a central population of compact massive blue star clusters. *AJ*, **103**, 691–702.

Hopkins, P. F., Cox, T. J., Dutta, S. N., Hernquist, L., Kormendy, J., Lauer, T. R.: 2009. Dissipation and Extra Light in Galactic Nuclei. II. "Cusp" Ellipticals. *ApJS*, **181**, 135–182.

Hopkins, P. F., Hernquist, L., Cox, T. J., Di Matteo, T., Martini, P., Robertson, B., Springel, V.: 2005. Black Holes in Galaxy Mergers: Evolution of Quasars. *ApJ*, **630**, 705–715.

Hummel, E. van der Hulst, J. M.: 1986. NGC 4038/39: Interacting spiral galaxies with enhanced extended radio emission. *A&A*, **155**, 151–160.

Inami, H., Armus, L., Surace, J. A., Mazzarella, J. M., Evans, A. S., Sanders, D. B., Howell, J. H., Petric, A., Vavilkin, T., Iwasawa, K., Haan, S., Murphy, E. J., Stierwalt, S., Appleton, P. N., Barnes, J. E., Bothun, G., Bridge, C. R., Chan, B., Charmandaris, V., Frayer, D. T., Kewley, L. J., Kim, D. C., Lord, S., Madore, B. F., Marshall, J. A., Matsuhara, H., Melbourne, J. E., Rich, J., Schulz, B., Spoon, H. W. W., Sturm, E., U, V., Veilleux, S., Xu, K.: 2010. The Buried Starburst in the Interacting Galaxy II Zw 096 as Revealed by the Spitzer Space Telescope. *AJ*, **140**, 63–74.

Jarosik, N., Bennett, C. L., Dunkley, J., Gold, B., Greason, M. R., Halpern, M., Hill, R. S., Hinshaw, G., Kogut, A., Komatsu, E., Larson, D., Limon, M., Meyer, S. S., Nolta, M. R., Odegard, N., Page, L.,

Smith, K. M., Spergel, D. N., Tucker, G. S., Weiland, J. L., Wollack, E., Wright, E. L.: 2011. Seven-year Wilkinson Microwave Anisotropy Probe (WMAP) Observations: Sky Maps, Systematic Errors, and Basic Results. *ApJS*, **192**, 14.

Jesseit, R., Cappellari, M., Naab, T., Emsellem, E., Burkert, A.: 2009. Specific angular momentum of disc merger remnants and the λ_R-parameter. *MNRAS*, **397**, 1202–1214.

Jesseit, R., Naab, T., Burkert, A.: 2005. Orbital structure of collisionless merger remnants: on the origin of photometric and kinematic properties of elliptical and S0 galaxies. *MNRAS*, **360**, 1185–1200.

Johansson, P. H., Naab, T., Burkert, A.: 2009. Equal- and Unequal-Mass Mergers of Disk and Elliptical Galaxies with Black Holes. *ApJ*, **690**, 802–821.

Joseph, R. D. Wright, G. S.: 1985. Recent star formation in interacting galaxies. II - Super starburst in merging galaxies. *MNRAS*, **214**, 87–95.

Juvela, M.: 2005. Efficient Monte Carlo methods for continuum radiative transfer. *A&A*, **440**, 531–546.

Kalberla, P. M. W. Dedes, L.: 2008. Global properties of the H I distribution in the outer Milky Way. Planar and extra-planar gas. *A&A*, **487**, 951–963.

Karl, S. J., Fall, S. M., Naab, T.: 2011. Disruption of Star Clusters in the Interacting Antennae Galaxies. *ApJ*, **734**, 11.

Karl, S. J., Naab, T., Johansson, P. H., Kotarba, H., Boily, C. M., Renaud, F., Theis, C.: 2010. One Moment in Time–Modeling Star Formation in the Antennae. *ApJ*, **715**, L88–L93.

Karl, S. J., Naab, T., Johansson, P. H., Theis, C., Boily, C. M.: 2008. Towards an accurate model for the Antennae galaxies. *Astronomische Nachrichten*, **329**, 1042.

Kassin, S. A., Frogel, J. A., Pogge, R. W., Tiede, G. P., Sellgren, K.: 2003. Stellar Populations in NGC 4038/39 (the Antennae): Exploring a Galaxy Merger Pixel by Pixel. *AJ*, **126**, 1276–1285.

Katz, N., Weinberg, D. H., Hernquist, L.: 1996. Cosmological Simulations with TreeSPH. *ApJS*, **105**, 19.

Kennicutt, Jr., R. C.: 1998. The Global Schmidt Law in Star-forming Galaxies. *ApJ*, **498**, 541.

Kent, S. M.: 1985. CCD surface photometry of field Galaxies. II - Bulge/disk decompositions. *ApJS*, **59**, 115–159.

Khochfar, S. Burkert, A.: 2006. Orbital parameters of merging dark matter halos. *A&A*, **445**, 403–412.

Klaas, U., Nielbock, M., Haas, M., Krause, O., Schreiber, J.: 2010. Tracing the sites of obscured star formation in the Antennae galaxies with Herschel-PACS. *A&A*, **518**, L44+.

Knierman, K. A., Gallagher, S. C., Charlton, J. C., Hunsberger, S. D., Whitmore, B., Kundu, A., Hibbard, J. E., Zaritsky, D.: 2003. From Globular Clusters to Tidal Dwarfs: Structure Formation in the Tidal Tails of Merging Galaxies. *AJ*, **126**, 1227–1244.

Komatsu, E., Smith, K. M., Dunkley, J., Bennett, C. L., Gold, B., Hinshaw, G., Jarosik, N., Larson, D., Nolta, M. R., Page, L., Spergel, D. N., Halpern, M., Hill, R. S., Kogut, A., Limon, M., Meyer, S. S., Odegard, N., Tucker, G. S., Weiland, J. L., Wollack, E., Wright, E. L.: 2011. Seven-year Wilkinson Microwave Anisotropy Probe (WMAP) Observations: Cosmological Interpretation. *ApJS*, **192**, 18.

Koopmans, L. V. E., Bolton, A., Treu, T., Czoske, O., Auger, M. W., Barnabè, M., Vegetti, S., Gavazzi, R., Moustakas, L. A., Burles, S.: 2009. The Structure and Dynamics of Massive Early-Type Galaxies: On Homology, Isothermality, and Isotropy Inside One Effective Radius. *ApJ*, **703**, L51–L54.

Kormendy, J. Bender, R.: 1996. A Proposed Revision of the Hubble Sequence for Elliptical Galaxies. *ApJ*, **464**, L119+.

Kormendy, J., Fisher, D. B., Cornell, M. E., Bender, R.: 2009. Structure and Formation of Elliptical and Spheroidal Galaxies. *ApJS*, **182**, 216–309.

Kotarba, H., Karl, S. J., Naab, T., Johansson, P. H., Dolag, K., Lesch, H., Stasyszyn, F. A.: 2010. Simulating Magnetic Fields in the Antennae Galaxies. *ApJ*, **716**, 1438–1452.

Krajnović, D., Bacon, R., Cappellari, M., Davies, R. L., de Zeeuw, P. T., Emsellem, E., Falcón-Barroso, J., Kuntschner, H., McDermid, R. M., Peletier, R. F., Sarzi, M., van den Bosch, R. C. E., van de Ven, G.: 2008. The SAURON project - XII. Kinematic substructures in early-type galaxies: evidence for discs in fast rotators. *MNRAS*, **390**, 93–117.

Krajnović, D., Emsellem, E., Cappellari, M., Alatalo, K., Blitz, L., Bois, M., Bournaud, F., Bureau, M., Davies, R. L., Davis, T. A., de Zeeuw, P. T., Khochfar, S., Kuntschner, H., Lablanche, P.-Y., McDermid, R. M., Morganti, R., Naab, T., Oosterloo, T., Sarzi, M., Scott, N., Serra, P., Weijmans, A.-M., Young, L. M.: 2011. The ATLAS^{3D} project - II. Morphologies, kinemetric features and alignment between photometric and kinematic axes of early-type galaxies. *MNRAS*, **414**, 2923–2949.

Kravtsov, A. V. Gnedin, O. Y.: 2005. Formation of Globular Clusters in Hierarchical Cosmology. *ApJ*, **623**, 650–665.

Lada, C. J. Lada, E. A.: 2003. Embedded Clusters in Molecular Clouds. *ARA&A*, **41**, 57–115.

Laine, S., van der Marel, R. P., Rossa, J., Hibbard, J. E., Mihos, J. C., Böker, T., Zabludoff, A. I.: 2003. A Hubble Space Telescope WFPC2 Investigation of the Nuclear Morphology in the Toomre Sequence of Merging Galaxies. *AJ*, **126**, 2717–2739.

Lauer, T. R., Faber, S. M., Gebhardt, K., Richstone, D., Tremaine, S., Ajhar, E. A., Aller, M. C., Bender, R., Dressler, A., Filippenko, A. V., Green, R., Grillmair, C. J., Ho, L. C., Kormendy, J., Magorrian, J., Pinkney, J., Siopis, C.: 2005. The Centers of Early-Type Galaxies with Hubble Space Telescope. V. New WFPC2 Photometry. *AJ*, **129**, 2138–2185.

Li, Y., Mac Low, M., Klessen, R. S.: 2004. Formation of Globular Clusters in Galaxy Mergers. *ApJ*, **614**, L29–L32.

Lilly, S. J., Le Fevre, O., Hammer, F., Crampton, D.: 1996. The Canada-France Redshift Survey: The Luminosity Density and Star Formation History of the Universe to Z approximately 1. *ApJ*, **460**, L1+.

Lotz, J. M., Davis, M., Faber, S. M., Guhathakurta, P., Gwyn, S., Huang, J., Koo, D. C., Le Floc'h, E., Lin, L., Newman, J., Noeske, K., Papovich, C., Willmer, C. N. A., Coil, A., Conselice, C. J., Cooper, M., Hopkins, A. M., Metevier, A., Primack, J., Rieke, G., Weiner, B. J.: 2008. The Evolution of Galaxy Mergers and Morphology at z $<$ 1.2 in the Extended Groth Strip. *ApJ*, **672**, 177–197.

Lotz, J. M., Jonsson, P., Cox, T. J., Croton, D., Primack, J. R., Somerville, R. S., Stewart, K.: 2011. The Major and Minor Galaxy Merger Rates at z $<$ 1.5. *ArXiv e-prints*.

Lucy, L. B.: 1977. A numerical approach to the testing of the fission hypothesis. *AJ*, **82**, 1013–1024.

Lutz, D., Spoon, H. W. W., Rigopoulou, D., Moorwood, A. F. M., Genzel, R.: 1998. The Nature and Evolution of Ultraluminous Infrared Galaxies:A Mid-Infrared Spectroscopic Survey. *ApJ*, **505**, L103–L107.

Madau, P., Ferguson, H. C., Dickinson, M. E., Giavalisco, M., Steidel, C. C., Fruchter, A.: 1996. High-redshift galaxies in the Hubble Deep Field: colour selection and star formation history to z˜4. *MNRAS*, **283**, 1388–1404.

Mahoney, J. H., van der Hulst, J. M., Burke, B. F.: 1984. Simulations and 21 cm Observations of the Colliding Galaxies NGC4038/39. In *Bulletin of the American Astronomical Society*, volume 16 of *Bulletin of the American Astronomical Society*, Seite 539.

Makino, J.: 1990. Comparison of Two Different Tree Algorithms. *Journal of Computational Physics*, **88**, 393.

McGaugh, S. S.: 2005. The Baryonic Tully-Fisher Relation of Galaxies with Extended Rotation Curves and the Stellar Mass of Rotating Galaxies. *ApJ*, **632**, 859–871.

McGaugh, S. S. de Blok, W. J. G.: 1997. Gas Mass Fractions and the Evolution of Spiral Galaxies. *ApJ*, **481**, 689.

McGaugh, S. S., Schombert, J. M., de Blok, W. J. G., Zagursky, M. J.: 2010. The Baryon Content of Cosmic Structures. *ApJ*, **708**, L14–L17.

McIntosh, D. H., Zabludoff, A. I., Rix, H.-W., Caldwell, N.: 2005. Testing the Universality of the (U-V) Color-Magnitude Relations for Nearby Clusters of Galaxies. *ApJ*, **619**, 193–217.

McKee, C. F. Ostriker, E. C.: 2007. Theory of Star Formation. *ARA&A*, **45**, 565–687.

McKee, C. F. Ostriker, J. P.: 1977. A theory of the interstellar medium - Three components regulated by supernova explosions in an inhomogeneous substrate. *ApJ*, **218**, 148–169.

Melena, N. W., Elmegreen, B. G., Hunter, D. A., Zernow, L.: 2009. Bright Ultraviolet Regions and Star Formation Characteristics in Nearby Dwarf Galaxies. *AJ*, **138**, 1203–1229.

Mengel, S., Lehnert, M. D., Thatte, N., Genzel, R.: 2005. Star-formation in NGC 4038/4039 from broad and narrow band photometry: cluster destruction? *A&A*, **443**, 41–60.

Merritt, D.: 1996. Optimal Smoothing for N-Body Codes. *AJ*, **111**, 2462.

Metz, J. M., Cooper, R. L., Guerrero, M. A., Chu, Y.-H., Chen, C.-H. R., Gruendl, R. A.: 2004. Hot Interstellar Gas and Stellar Energy Feedback in the Antennae Galaxies. *ApJ*, **605**, 725–741.

Meurer, G. R., Heckman, T. M., Leitherer, C., Kinney, A., Robert, C., Garnett, D. R.: 1995. Starbursts and Star Clusters in the Ultraviolet. *AJ*, **110**, 2665.

Mihos, J. C.: 2001. The Development of Gas/Star Offsets in Tidal Tails. *ApJ*, **550**, 94–103.

Mihos, J. C., Bothun, G. D., Richstone, D. O.: 1993. Modeling the Spatial Distribution of Star Formation in Interacting Disk Galaxies. *ApJ*, **418**, 82.

Mihos, J. C. Hernquist, L.: 1994. Dense stellar cores in merger remnants. *ApJ*, **437**, L47–L50.

Mihos, J. C. Hernquist, L.: 1996. Gasdynamics and Starbursts in Major Mergers. *ApJ*, **464**, 641.

Mihos, J. C., Richstone, D. O., Bothun, G. D.: 1991. A numerical study of star formation in interacting disk galaxies. *ApJ*, **377**, 72–88.

Mihos, J. C., Richstone, D. O., Bothun, G. D.: 1992. Models of star formation in interacting and merging disk galaxies. *ApJ*, **400**, 153–162.

Mills, B. Y., Slee, O. B., Hill, E. R.: 1958. A Catalogue of Radio Sources between Declinations +10° and -20°. *Australian Journal of Physics*, **11**, 360.

Minkowski, R.: 1957. Optical investigations of radio sources (Introductory Lecture). In H. C. van de Hulst, editor, *Radio astronomy*, volume 4 of *IAU Symposium*, Seite 107.

Mirabel, I. F., Dottori, H., Lutz, D.: 1992. Genesis of a dwarf galaxy from the debris of the Antennae. *A&A*, **256**, L19–L22.

Mirabel, I. F., Vigroux, L., Charmandaris, V., Sauvage, M., Gallais, P., Tran, D., Cesarsky, C., Madden, S. C., Duc, P.-A.: 1998. The dark side of star formation in the Antennae galaxies. *A&A*, **333**, L1–L4.

Mo, H. J., Mao, S., White, S. D. M.: 1998. The formation of galactic discs. *MNRAS*, **295**, 319–336.

Monaghan, J. J.: 1992. Smoothed particle hydrodynamics. *ARA&A*, **30**, 543–574.

Monaghan, J. J.: 1997. SPH and Riemann Solvers. *Journal of Computational Physics*, **136**, 298–307.

Mora, M. D., Larsen, S. S., Kissler-Patig, M., Brodie, J. P., Richtler, T.: 2009. Imaging of star clusters in unperturbed spiral galaxies with the Advanced Camera for Surveys. II. A comparison of star cluster systems in five late type spirals. *A&A*, **501**, 949–964.

Moster, B. P., Macciò, A. V., Somerville, R. S., Johansson, P. H., Naab, T.: 2010a. Can gas prevent the destruction of thin stellar discs by minor mergers? *MNRAS*, **403**, 1009–1019.

Moster, B. P., Somerville, R. S., Maulbetsch, C., van den Bosch, F. C., Macciò, A. V., Naab, T., Oser, L.: 2010b. Constraints on the Relationship between Stellar Mass and Halo Mass at Low and High Redshift. *ApJ*, **710**, 903–923.

Muñoz-Cuartas, J. C., Macciò, A. V., Gottlöber, S., Dutton, A. A.: 2011. The redshift evolution of Λ cold dark matter halo parameters: concentration, spin and shape. *MNRAS*, **411**, 584–594.

Naab, T. Burkert, A.: 2003. Statistical Properties of Collisionless Equal- and Unequal-Mass Merger Remnants of Disk Galaxies. *ApJ*, **597**, 893–906.

Naab, T., Jesseit, R., Burkert, A.: 2006. The influence of gas on the structure of merger remnants. *MNRAS*, **372**, 839–852.

Naab, T. Ostriker, J. P.: 2009. Are Disk Galaxies the Progenitors of Giant Ellipticals? *ApJ*, **690**, 1452–1462.

Naab, T. Trujillo, I.: 2006. Surface density profiles of collisionless disc merger remnants. *MNRAS*, **369**, 625–644.

Naiman, J. P., Ramirez-Ruiz, E., Lin, D. N. C.: 2009. Gas Accretion by Star Clusters and the Formation of Ultraluminous X-Ray Sources from Cusps of Compact Remnants. *ApJ*, **705**, L153–L157.

Navarro, J. F., Frenk, C. S., White, S. D. M.: 1997. A Universal Density Profile from Hierarchical Clustering. *ApJ*, **490**, 493.

Neff, S. G. Ulvestad, J. S.: 2000. VLA Observations of the Nearby Merger NGC 4038/4039: H II Regions and Supernova Remnants in the "Antennae". *AJ*, **120**, 670–696.

Negroponte, J. White, S. D. M.: 1983. Simulations of mergers between disc-halo galaxies. *MNRAS*, **205**, 1009–1029.

Neisser, U. Weene, P.: 1960. A note on human recognition of hand-printed characters. *Information and Control*, **3**(2), 191 – 196.

Nipoti, C., Londrillo, P., Ciotti, L.: 2003. Galaxy merging, the fundamental plane of elliptical galaxies and the M_{BH}-σ_0 relation. *MNRAS*, **342**, 501–512.

Noguchi, M.: 1988. Gas dynamics in interacting disc galaxies - Fuelling of nuclei by induced bars. *A&A*, **203**, 259–272.

O'Connell, R. W., Gallagher, III, J. S., Hunter, D. A., Colley, W. N.: 1995. Hubble Space Telescope Imaging of Super Star Clusters in M82. *ApJ*, **446**, L1+.

Pancoast, A., Sajina, A., Lacy, M., Noriega-Crespo, A., Rho, J.: 2010. Star Formation and Dust Obscuration in the Tidally Distorted Galaxy NGC 2442. *ApJ*, **723**, 530–543.

Patton, D. R., Pritchet, C. J., Carlberg, R. G., Marzke, R. O., Yee, H. K. C., Hall, P. B., Lin, H., Morris, S. L., Sawicki, M., Shepherd, C. W., Wirth, G. D.: 2002. Dynamically Close Galaxy Pairs and Merger Rate Evolution in the CNOC2 Redshift Survey. *ApJ*, **565**, 208–222.

Peletier, R. F., Davies, R. L., Illingworth, G. D., Davis, L. E., Cawson, M.: 1990. CCD surface photometry of galaxies with dynamical data. II - UBR photometry of 39 elliptical galaxies. *AJ*, **100**, 1091–1142.

Pellerin, A., Meurer, G. R., Bekki, K., Elmegreen, D. M., Wong, O. I., Knezek, P. M.: 2010. The Star Cluster Population of the Collisional Ring Galaxy NGC 922. *AJ*, **139**, 1369–1382.

Pelupessy, F. I. Papadopoulos, P. P.: 2009. Molecular Gas, CO, and Star Formation in Galaxies: Emergent Empirical Relations, Feedback, and the Evolution of Very Gas-Rich Systems. *ApJ*, **707**, 954–970.

Perrine, C. D.: 1922. Nebulæ, Note on four interesting. *MNRAS*, **82**, 486.

Peterson, B. W., Struck, C., Smith, B. J., Hancock, M.: 2009. Star clusters in the interacting galaxy system Arp 284. *MNRAS*, **400**, 1208–1224.

Petsch, H. P. Theis, C.: 2011. Determining properties of the Antennae system - Merging ability for restricted N-body. In H. Wozniak & G. Hensler, editor, *EAS Publications Series*, volume 44 of *EAS Publications Series*, Seiten 33–36.

Pfleiderer, J.: 1963. Gravitationseffekte bei der Begegnung zweier Galaxien. Mit 5 Textabbildungen. *Zeitschrift fur Astrophysik*, **58**, 12.

Pfleiderer, J. Siedentopf, H.: 1961. Spiralstrukturen durch Gezeiteneffekte bei der Begegnung zweier Galaxien. Mit 7 Textabbildungen. *Zeitschrift fur Astrophysik*, **51**, 201.

Plummer, H. C.: 1911. On the problem of distribution in globular star clusters. *MNRAS*, **71**, 460–470.

Portegies Zwart, S. F., McMillan, S. L. W., Gieles, M.: 2010. Young Massive Star Clusters. *ARA&A*, **48**, 431–493.

Price, D.: 2005. Smoothed Particle Hydrodynamics. *ArXiv Astrophysics e-prints*.

Quinn, P. J., Hernquist, L., Fullagar, D. P.: 1993. Heating of galactic disks by mergers. *ApJ*, **403**, 74–93.

Quinn, T., Katz, N., Stadel, J., Lake, G.: 1997. Time stepping N-body simulations. *ArXiv Astrophysics e-prints*.

Renaud, F., Boily, C. M., Fleck, J., Naab, T., Theis, C.: 2008. Star cluster survival and compressive tides in Antennae-like mergers. *MNRAS*, **391**, L98–L102.

Renaud, F., Boily, C. M., Naab, T., Theis, C.: 2009. Fully Compressive Tides in Galaxy Mergers. *ApJ*, **706**, 67–82.

Robertson, B. E. Kravtsov, A. V.: 2008. Molecular Hydrogen and Global Star Formation Relations in Galaxies. *ApJ*, **680**, 1083–1111.

Rosse, E. O.: 1861. On the Construction of Specula of Six-Feet Aperture; and a Selection from the Observations of Nebulae Made with Them. *Royal Society of London Philosophical Transactions Series I*, **151**, 681–745.

Rothberg, B. Joseph, R. D.: 2004. A Deep K-Band Photometric Survey of Merger Remnants. *AJ*, **128**, 2098–2143.

Rubin, V. C., Ford, W. K. J., D'Odorico, S.: 1970. Emission-Line Intensities and Radial Velocities in the Interacting Galaxies NGC 4038-4039. *ApJ*, **160**, 801.

Salpeter, E. E.: 1955. The Luminosity Function and Stellar Evolution. *ApJ*, **121**, 161.

Sanders, D. B., Mazzarella, J. M., Kim, D.-C., Surace, J. A., Soifer, B. T.: 2003. The IRAS Revised Bright Galaxy Sample. *AJ*, **126**, 1607–1664.

Sanders, D. B. Mirabel, I. F.: 1996. Luminous Infrared Galaxies. *ARA&A*, **34**, 749.

Saviane, I., Momany, Y., da Costa, G. S., Rich, R. M., Hibbard, J. E.: 2008. A New Red Giant-based Distance Modulus of 13.3 Mpc to the Antennae Galaxies and Its Consequences. *ApJ*, **678**, 179–186.

Schmidt, M.: 1959. The Rate of Star Formation. *ApJ*, **129**, 243.

Schweizer, F.: 1978. Galaxies with long tails. In Berkhuijsen, E. M. Wielebinski, R., editors, *Structure and Properties of Nearby Galaxies*, volume 77 of *IAU Symposium*, Seiten 279–284.

Schweizer, F., Burns, C. R., Madore, B. F., Mager, V. A., Phillips, M. M., Freedman, W. L., Boldt, L., Contreras, C., Folatelli, G., González, S., Hamuy, M., Krzeminski, W., Morrell, N. I., Persson, S. E., Roth, M. R., Stritzinger, M. D.: 2008. a New Distance to the Antennae Galaxies (ngc 4038/39) Based on the Type ia Supernova 2007sr. *AJ*, **136**, 1482–1489.

Sersic, J. L.: 1968. *Atlas de galaxias australes*.

Shapley, H. Paraskevopoulos, J. S.: 1940. Galactic and Extragalactic Studies, III. Photographs of Thirty Southern Nebulae and Clusters. *Proceedings of the National Academy of Science*, **26**, 31–36.

Smith, B. J., Struck, C., Hancock, M., Appleton, P. N., Charmandaris, V., Reach, W. T.: 2007. The Spitzer Spirals, Bridges, and Tails Interacting Galaxy Survey: Interaction-Induced Star Formation in the Mid-Infrared. *AJ*, **133**, 791–817.

Spitzer, L.: 1987. *Dynamical evolution of globular clusters*.

Spitzer, Jr., L.: 1958. Distribution of Galactic Clusters. *ApJ*, **127**, 17.

Springel, V.: 2000. Modelling star formation and feedback in simulations of interacting galaxies. *MNRAS*, **312**, 859–879.

Springel, V.: 2005. The cosmological simulation code GADGET-2. *MNRAS*, **364**, 1105–1134.

Springel, V., Di Matteo, T., Hernquist, L.: 2005. Modelling feedback from stars and black holes in galaxy mergers. *MNRAS*, **361**, 776–794.

Springel, V. Hernquist, L.: 2002. Cosmological smoothed particle hydrodynamics simulations: the entropy equation. *MNRAS*, **333**, 649–664.

Springel, V. Hernquist, L.: 2003. Cosmological smoothed particle hydrodynamics simulations: a hybrid multiphase model for star formation. *MNRAS*, **339**, 289–311.

Springel, V. White, S. D. M.: 1999. Tidal tails in cold dark matter cosmologies. *MNRAS*, **307**, 162–178.

Stanford, S. A., Sargent, A. I., Sanders, D. B., Scoville, N. Z.: 1990. CO aperture synthesis of NGC 4038/39 (ARP 244). *ApJ*, **349**, 492–496.

Steinicke, W.: 2010. *Observing and Cataloguing Nebulae and Star Clusters: From Herschel to Dreyer's New General Catalogue*. Cambridge University Press.

Steinmetz, M.: 1996. GRAPESPH: cosmological smoothed particle hydrodynamics simulations with the special-purpose hardware GRAPE. *MNRAS*, **278**, 1005–1017.

Struck, C.: 1997. Simulations of Collisions between Two Gas-rich Galaxy Disks with Heating and Cooling. *ApJS*, **113**, 269.

Struve, O. Linke, W.: 1940. The Spectra of Three Southern Extragalactic Nebulae. *PASP*, **52**, 139.

Tacconi, L. J., Genzel, R., Neri, R., Cox, P., Cooper, M. C., Shapiro, K., Bolatto, A., Bouché, N., Bournaud, F., Burkert, A., Combes, F., Comerford, J., Davis, M., Schreiber, N. M. F., Garcia-Burillo, S., Gracia-Carpio, J., Lutz, D., Naab, T., Omont, A., Shapley, A., Sternberg, A., Weiner, B.: 2010. High molecular gas fractions in normal massive star-forming galaxies in the young Universe. *Nature*, **463**, 781–784.

Tacconi, L. J., Genzel, R., Tecza, M., Gallimore, J. F., Downes, D., Scoville, N. Z.: 1999. Gasdynamics in the Luminous Merger NGC 6240. *ApJ*, **524**, 732–745.

Teyssier, R.: 2002. Cosmological hydrodynamics with adaptive mesh refinement. A new high resolution code called RAMSES. *A&A*, **385**, 337–364.

Teyssier, R., Chapon, D., Bournaud, F.: 2010. The Driving Mechanism of Starbursts in Galaxy Mergers. *ApJ*, **720**, L149–L154.

Theis, C.: 1999. Modeling Encounters of Galaxies: The Case of NGC 4449. In R. E. Schielicke, editor, *Reviews in Modern Astronomy*, volume 12 of *Reviews in Modern Astronomy*, Seite 309.

Theis, C. Kohle, S.: 2001. Multi-method-modeling of interacting galaxies. I. A unique scenario for NGC 4449? *A&A*, **370**, 365–383.

Toomre, A.: 1974. Gravitational interactions between galaxies. In Shakeshaft, J. R., editor, *The Formation and Dynamics of Galaxies*, volume 58 of *IAU Symposium*, Seiten 347–363.

Toomre, A.: 1977. Mergers and Some Consequences. In Tinsley, B. M. Larson, R. B., editors, *Evolution of Galaxies and Stellar Populations*, Seite 401.

Toomre, A. Toomre, J.: 1970. On Intergalactic Bridges. In *Bulletin of the American Astronomical Society*, volume 2 of *Bulletin of the American Astronomical Society*, Seite 350.

Toomre, A. Toomre, J.: 1971. Theorectical Model of NGC 4038/39. In *Bulletin of the American Astronomical Society*, volume 3 of *Bulletin of the American Astronomical Society*, Seite 390.

Toomre, A. Toomre, J.: 1972. Galactic Bridges and Tails. *ApJ*, **178**, 623–666.

Tortora, C., Napolitano, N. R., Cardone, V. F., Capaccioli, M., Jetzer, P., Molinaro, R.: 2010. Colour and stellar population gradients in galaxies: correlation with mass. *MNRAS*, **407**, 144–162.

Trujillo, I., Erwin, P., Asensio Ramos, A., Graham, A. W.: 2004. Evidence for a New Elliptical-Galaxy Paradigm: Sérsic and Core Galaxies. *AJ*, **127**, 1917–1942.

van den Bosch, R. C. E., van de Ven, G., Verolme, E. K., Cappellari, M., de Zeeuw, P. T.: 2008. Triaxial orbit based galaxy models with an application to the (apparent) decoupled core galaxy NGC 4365. *MNRAS*, **385**, 647–666.

van der Hulst, J. M.: 1979. The kinematics and distribution of neutral hydrogen in the interacting galaxy pair NGC 4038/39. *A&A*, **71**, 131–140.

Velazquez, H. White, S. D. M.: 1999. Sinking satellites and the heating of galaxy discs. *MNRAS*, **304**, 254–270.

Vigroux, L., Mirabel, F., Altieri, B., Boulanger, F., Cesarsky, C., Cesarsky, D., Claret, A., Fransson, C., Gallais, P., Levine, D., Madden, S., Okumura, K., Tran, D.: 1996. ISOCAM observations of the Antennae Galaxies. *A&A*, **315**, L93–L96.

Vorontsov-Velyaminov, B. A.: 1959. Atlas and catalog of interacting galaxies. 1959, Sternberg Institute, Moscow State University. In *Atlas and catalog of interacting galaxies (1959)*, Seite 0.

Wahde, M.: 1998. Determination of orbital parameters of interacting galaxies using a genetic algorithm. Description of the method and application to artificial data. *A&AS*, **132**, 417–429.

Wang, J., Zhang, Q., Wang, Z., Ho, P. T. P., Fazio, G. G., Wu, Y.: 2004a. Warm Molecular Gas in Galaxy-Galaxy Merger NGC 6090. *ApJ*, **616**, L67–L70.

Wang, Z., Fazio, G. G., Ashby, M. L. N., Huang, J.-S., Pahre, M. A., Smith, H. A., Willner, S. P., Forrest, W. J., Pipher, J. L., Surace, J. A.: 2004b. The Off-Nuclear Starbursts in NGC 4038/4039 (The Antennae Galaxies). *ApJS*, **154**, 193–198.

Westmoquette, M. S., Smith, L. J., Gallagher, III, J. S., Trancho, G., Bastian, N., Konstantopoulos, I. S.: 2009. The Optical Structure of the Starburst Galaxy M82. I. Dynamics of the Disk and Inner-Wind. *ApJ*, **696**, 192–213.

Wetzstein, M., Naab, T., Burkert, A.: 2007. Do dwarf galaxies form in tidal tails? *MNRAS*, **375**, 805–820.

White, S. D. M.: 1979. Further simulations of merging galaxies. *MNRAS*, **189**, 831–852.

Whitmore, B. C., Chandar, R., Fall, S. M.: 2007. Star Cluster Demographics. I. A General Framework and Application to the Antennae Galaxies. *AJ*, **133**, 1067–1084.

Whitmore, B. C., Chandar, R., Schweizer, F., Rothberg, B., Leitherer, C., Rieke, M., Rieke, G., Blair, W. P., Mengel, S., Alonso-Herrero, A.: 2010. The Antennae Galaxies (NGC 4038/4039) Revisited: Advanced Camera for Surveys and NICMOS Observations of a Prototypical Merger. *AJ*, **140**, 75–109.

Whitmore, B. C. Schweizer, F.: 1995. Hubble space telescope observations of young star clusters in NGC-4038/4039, 'the antennae' galaxies. *AJ*, **109**, 960–980.

Whitmore, B. C., Zhang, Q., Leitherer, C., Fall, S. M., Schweizer, F., Miller, B. W.: 1999. The Luminosity Function of Young Star Clusters in "the Antennae" Galaxies (NGC 4038-4039). *AJ*, **118**, 1551–1576.

Wilson, C. D. Scoville, N.: 1990. The properties of individual giant molecular clouds in M33. *ApJ*, **363**, 435–450.

Wilson, C. D., Scoville, N., Madden, S. C., Charmandaris, V.: 2000. High-Resolution Imaging of Molecular Gas and Dust in the Antennae (NGC 4038/39): Super Giant Molecular Complexes. *ApJ*, **542**, 120–127.

Wright, A. E.: 1972. Computational models of gravitationally interacting galaxies. *MNRAS*, **157**, 309.

Xu, C., Gao, Y., Mazzarella, J., Lu, N., Sulentic, J. W., Domingue, D. L.: 2000. Mapping Infrared Enhancements in Closely Interacting Spiral-Spiral Pairs. I. ISO CAM and ISO SWS Observations. *ApJ*, **541**, 644–659.

Yabushita, S.: 1971. The possibility of capture in the restricted problem of three bodies and formation of bridges between galaxies. *MNRAS*, **153**, 97.

Zezas, A. Fabbiano, G.: 2002. Chandra Observations of "The Antennae" Galaxies (NGC 4038/4039). IV. The X-Ray Source Luminosity Function and the Nature of Ultraluminous X-Ray Sources. *ApJ*, **577**, 726–737.

Zezas, A., Fabbiano, G., Baldi, A., Schweizer, F., King, A. R., Ponman, T. J., Rots, A. H.: 2006. Chandra Monitoring Observations of The Antennae Galaxies. I. Catalog of Source Properties. *ApJS*, **166**, 211–248.

Zezas, A., Fabbiano, G., Baldi, A., Schweizer, F., King, A. R., Rots, A. H., Ponman, T. J.: 2007. Chandra Monitoring Observations of the Antennae Galaxies. II. X-Ray Luminosity Functions. *ApJ*, **661**, 135–148.

Zezas, A., Fabbiano, G., Rots, A. H., Murray, S. S.: 2002. Chandra Observations of "The Antennae" Galaxies (NGC 4038/4039). III. X-Ray Properties and Multiwavelength Associations of the X-Ray Source Population. *ApJ*, **577**, 710–725.

Zhang, H., Gao, Y., Kong, X.: 2010. Star formation histories within the Antennae galaxies (Arp244). *MNRAS*, **401**, 1839–1849.

Zhang, Q. Fall, S. M.: 1999. The Mass Function of Young Star Clusters in the "Antennae" Galaxies. *ApJ*, **527**, L81–L84.

Zhang, Q., Fall, S. M., Whitmore, B. C.: 2001. A Multiwavelength Study of the Young Star Clusters and Interstellar Medium in the Antennae Galaxies. *ApJ*, **561**, 727–750.

Zhu, M., Seaquist, E. R., Kuno, N.: 2003. A Multitransition CO Study of the Antennae Galaxies NGC 4038/9. *ApJ*, **588**, 243–263.

Zwicky, F.: 1953. Luminous and dark formations of intergalactic matter. *Physics Today*, **6**, 7–11.

Zwicky, F.: 1956. Multiple Galaxies. *Ergebnisse der exakten Naturwissenschaften*, **29**, 344–385.

Zwicky, F.: 1959. Multiple Galaxies. *Handbuch der Physik*, **53**, 373.

List of Publications

REFEREED JOURNAL ARTICLES

- *One Moment in Time - Modeling Star Formation in the Antennae*
  Karl, S. J., Naab, T., Johansson, P. H., Kotarba, H., Boily, C. M., Renaud, F., & Theis, C. 2010, ApJ, 715, L88

- *Simulating Magnetic Fields in the Antennae Galaxies*
  Kotarba, H., **Karl, S. J.**, Naab, T., Johansson, P. H., Dolag, K., Lesch, H., & Stasyszyn, F. A. 2010, ApJ, 716, 1438

- *NGC6240: Merger-Induced Star Formation & Gas Dynamics*
  Engel, H., Davies, R. I., Genzel, R., Tacconi, L. J., Hicks, E. K. S., Sturm, E., Naab, T., Johansson, P. H., **Karl, S. J.**, Max, C. E., Medling, A., & van der Werf, P. P. 2010, A&A, 524, 56

- *Disruption of Star Clusters in the Interacting Antennae Galaxies*
  Karl, S. J., Fall, S. M., & Naab, T. 2011, ApJ, 734, 11

REFEREED CONFERENCE PROCEEDINGS

- *Towards an accurate model for the Antennae galaxies*
  Karl, S. J., Naab, T., Johansson, P. H., Theis, C., & Boily, C. M. 2008, AN, 329, 1042

PUBLICATIONS IN PREPARATION

- *The fate of the Antennae galaxies - will their merger remnant resemble a normal elliptical?*
  Karl, S. J., Hilz, M., Naab, T., & Oser, L., in preparation

- *Combining regularization with a tree: Implementation of an algorithmic regularized chain method into the VINE tree-code*
  Karl, S. J., Aarseth, S. J., & Naab, T., in preparation

Danksagung

An erster Stelle gilt mein besonderer Dank meinem Betreuer Dr. Thorsten Naab für seinen unermüdlichen Einsatz für meine Arbeit, die immer neuen Forschungsideen und die vielen spannenden und lehrreichen Reisen, die ich während dieser Zeit unternehmen durfte. Ohne seine fortwährende Unterstützung wäre meine Doktorabeit so nicht möglich gewesen.

Desweiteren bedanke ich mich bei Prof. Dr. Andreas Burkert für die Möglichkeit, nach meiner Diplomarbeit auch Teile meiner Doktorarbeit am Lehrstuhl für "Computational Astrophysics" (CAST) an der Universitäts-Sternwarte (USM) schreiben zu dürfen. Der CAST Gruppe danke ich für eine immer positive und kreative Arbeitsatmosphäre.

Meine Arbeit wurde finanziell unterstützt durch das Schwerpunktprogramm "Witnesses of cosmic history: formation and evolution of black holes, galaxies and their environment" der Deutschen Forschungsgemeinschaft (DFG) sowie das Max-Planck-Institut für Astrophysik (MPA) in Garching, was mir unbeschwerte erste Schritte in der Astrophysik erlaubte. Einen herzlichen Dank dafür!

Ein spezieller Dank gilt all den netten und interessanten Menschen, die ich während meiner Doktorarbeit treffen durfte, z.B. Sverre Aarseth, Chris Boily, Christian Theis, Michael Fall, Romain Teissier, Hanns Petsch, Florent Renaud und Veronica Biffi. Danke für die vielen hilfreichen Diskussionen und Kommentare und die produktiven Kollarborationen! Besonders bedanke ich mich bei Prof. Michael Fall dafür, dass er mich in neue Dimensionen der wissenschaflichen Methodik eingeführt hat, und Dr. Sverre Aarseth für seine engagierte Zusammenarbeit bei unserem Projekt zu den massiven schwarzen Löchern.

Ganz herzlich bedanke ich mich auch bei allen Sekretärinnen und System-Administratoren an der USM und dem MPA für die schnelle, nette und unkomplizierte Hilfe, wann immer ich in Not war.

Danke an alle meine Kollegen und Betreuer, v.a. Peter, Roland, Michi, Ludwig, Hanna, Micha, Matthias, Stefan und die zwei Steffis für die tolle Zeit, die wir miteinander hatten, und dass immer Zeit für einen schnellen Kaffee oder ein gemütliches Bier war.

Ein dreifaches Hipp-Hipp-Hurra auf die Laufgruppe an der USM, die mich immer bei guter Gesundheit und Fitness gehalten hat!

Vielen lieben Dank auch an alle meine münchener, regensburger und niederbayrischen Freunde für die schönen Biergarten- und Kletterabende, und v.a. die unvergesslichen WG- und Rossstall-Parties. “River Hearts of Ell”, keep on rocking!

Nicht zuletzt gilt mein tiefer Dank meiner Schwester und meinen Eltern, sowie meiner Freundin Ursula und ihrer Familie, für ihre immerwährende Unterstützung und die schöne Zeit, die wir in den letzten Jahren in München und Umgebung zusammen verbracht haben.

Ehrenwörtliche Erklärung

des Doktoranden

Simon Johannes Karl

Mit der Abgabe dieser Doktorarbeit erkläre ich, dass ich diese Arbeit selbständig verfasst und angefertigt habe. Ich habe, ausser den angegebenen, keine anderen Quellen und Hilfsmitteln verwendet.

München, den 22. September 2011,
Ort, Datum

Unterschrift